High Speed All-Optical Switching Based on a Single-Arm Interferometer

by

Naimish S. Patel

Submitted to the Department of Electrical Engineering and Computer Science
in Partial Fulfillment of the Requirements for the Degrees of
Bachelor of Science in Electrical Science and Engineering
and Master of Engineering in Electrical Engineering and Computer Science
at the Massachusetts Institute of Technology
May 1996

Author____
Department of Electrical Engineering and Computer Science
May 17, 1992

Certified by ____
Dr. Erich Ippen
Thesis Supervisor

Accepted by ____
F.R. Morgenthaler
Chairman, Department Committee on Graduate Theses

High Speed All-Optical Switching Based on a Single-Arm Interferometer
by
Naimish S. Patel

Submitted to the
Department of Electrical Engineering and Computer Science

May 17, 1996

In Partial Fulfillment of the Requirements for the Degree of
Bachelor of Science in Electrical Engineering
and Master of Engineering in Electrical Engineering and Computer Science

ABSTRACT

This thesis outlines the design, implementation, and experimental results of a family of all-optical switching devices based on a single-arm interferometer (SAI) geometry. This work was undertaken as part of a research effort in devices for ultra-high speed (~ 100 Gb/s) time division multiplexed networks. It is shown that the functional versatility of the SAI geometry allows one to implement generalized optical logic elements that are cascadable, interferometrically stable, compact, and can potentially be integrated in semiconductor. Except for the SAI based devices presented in this thesis, most optical switches to date have not simultaneously exhibited all these characteristics. Experimental results of all-optical demultiplexing, AND, NOT, OR, NOR, and XOR gating at data rates up to 40 Gb/s are presented. These results represent the highest rate demonstration of bit-wise optical logic to date. A theoretical treatment of the SAI switching characteristics is presented for the cases of a fiber and semiconductor nonlinearity. Particular attention is paid to performance metrics including switching efficiency, amplitude and timing jitter tolerance, and data rate scaleability. In addition, a comparative analysis between SAI-based devices and other devices of current interest is outlined from the perspective of device functionality and practicality. The final section of this thesis provides some speculative ideas for future work and development.

Thesis Supervisor: Dr. Erich Ippen
Title: Elihu Thomson Professor of Electrical Engineering

Acknowledgments

I am first and foremost indebted to my supervisors and Lincoln Laboratory and MIT. Kristin Rauschenbach has been a model supervisor. Always the source of constructive comments and new ideas, I have learned a great deal from her, both theoretical and experimental (free space alignment!). Indeed, this thesis is an off shoot of her work on switching using the single-arm interferometer. I am very fortunate that she introduced me to this fascinating subject. Katie Hall has been a great source of encouragement and supervision. It is a great pleasure working with her in the lab, as she is one the most amiable people I know. I have gained much from our discussions and her expertise in the lab is something I have striven towards. It has been an honor having a pioneer in nonlinear optics, Professor Ippen, as my thesis advisor. He has been a valuable source of information. When I had gaps in my understanding, I knew who to ask!

It has been a delight working in group 67. I am thankful to Roy Bondurant and Vincent Chan for giving me the opportunity to work with experts in optics and communications. John Moores has been a source of theoretical insight (Eq. 3.15 is the result of his innovative mathematical trickery!). The bit error rate measurements that form the crux of the experimental data in this thesis would not have been possible without Jeff Livas's generosity. Discussions with him have helped me greatly in understanding what they mean. Thanks also go to Salil Parikh, Doug Marquis, Laura Adams, Igor Gonta, Todd Knibbe, Sue LePage, Eric Swanson, Dan Castagnozzi, Fred Walther, Rick Barry, Emily Kintzer, John Kaufmann, and Claudia Fennelly.

Table Of Contents

Appendix

List of Figures

Chapter 1: Motivation

One of the fastest growing industries nowadays is telecommunications. The global network, alias "The Information Superhighway", projected for the future will carry telephone conversations, high definition video, electronic mail, gigabyte files, and potentially even real time tele-medicine. Such applications require extremely high channel bandwidths. The use of high density time and frequency division multiplexing makes the provisioning of such high bandwidths possible. Since the fabrication of low loss silica fiber in the 1970's, it has been recognized that single mode optical fiber has the large inherent bandwidths (10 THz and beyond), dispersion characteristics, and most importantly low loss (.2 dB/km) suitable for the future generations of optical network infrastructures. Moreover, nonlinearities in silica fiber are now being exploited in all optical switching devices and long distance repeaterless transmission. In fact, the feasibility of ultra-high capacity optical fiber transmission systems has very recently been demonstrated, simultaneously by 3 research groups, at aggregate rates exceeding 1 Tb/s![1,2,3]

Terrestrial data networks are likely to undergo an evolution in which more of the transparent services of the network such as switching and possibly even routing will be accomplished via optical means, thus relieving the so called electronics bottleneck due to opto-electronic data conversion. The latter enables high bit rate streams to gradually pervade the periphery of the network instead of residing primarily at the center. As such, the electronic - optical interface will be pushed closer to the user, allowing individuals to burst data onto the network at very high rates. Such high rate networks may ultimately be used in distributed processing systems in which low latency, high rate connectivity is required for computationally complex numerical tasks. It is also conceivable that local area networks with single channel capacities of up to 100 Gb/s will be made possible by the utilization of transparent all-optical techniques. These systems, however, are based on intrinsically large latency topologies and architecturally are not well understood. As such, they are currently the target of a considerable architectural research effort[4]. Lastly, long haul transmission systems could very well benefit from optical processing. Currently, 64 Kb/s telephone conversations are electronically time division multiplexed (MUX'd) to rates of 2.5 Gb/s and higher for transoceanic optical transmission. At the receiver end, these high rate streams are electronically demultiplexed (DEMUX'd). As the channel capacities of the long haul links approach tens of Gb/s, the electronics required to MUX and DEMUX the data become increasingly expensive. Moreover, it is not clear whether the use of electronics operating at rates over 40 Gb/s is practical or even feasible, particularly when packaging is concerned.[5] Consequently, all optical demultiplexing at rates exceeding 100 Gb/s may be a solution.

The implementation of the types of networks described above requires the development of a number of digital optical components. High speed optical multiplexers and demultiplexers are required primarily for long links, but also in local area networks. Wavelength and pulsewidth converters are required for inter-networking high speed time division multiplexed (TDM) systems with wavelength division multiplexed (WDM) systems. Rate conversion will also be required to allow a variety of user access rates in addition to providing connectivity between sub-networks. Access nodes in local area networks require many different optical elements to implement high speed clock recovery, optical buffering, header processing, etc. A conception of a high speed access node is depicted in Figure 1.1[6] in which optical signals / components are represented by thickened lines and electronics by thin lines. One may envision such an access node that receives packets at 100 Gb/s, optically recovers the bit and slot clocks, stores the optical packet, checks the address in the packet header, and subsequently either discards or keeps the packet. Outward going data would be stored in an optical buffer and then burst onto the network at 100 Gb/s into an allocated time slot. It is currently not yet clear where it makes sense to put the interface between electronics and optics in the access node partly because the capabilities of the optical technologies are not yet known. Moreover, the capabilities of the underlying technology largely determine the degree of complexity of the network protocol scheme. The simpler the low level protocol, the better, because the interconnectivity of optical processing devices, at present, is limited.

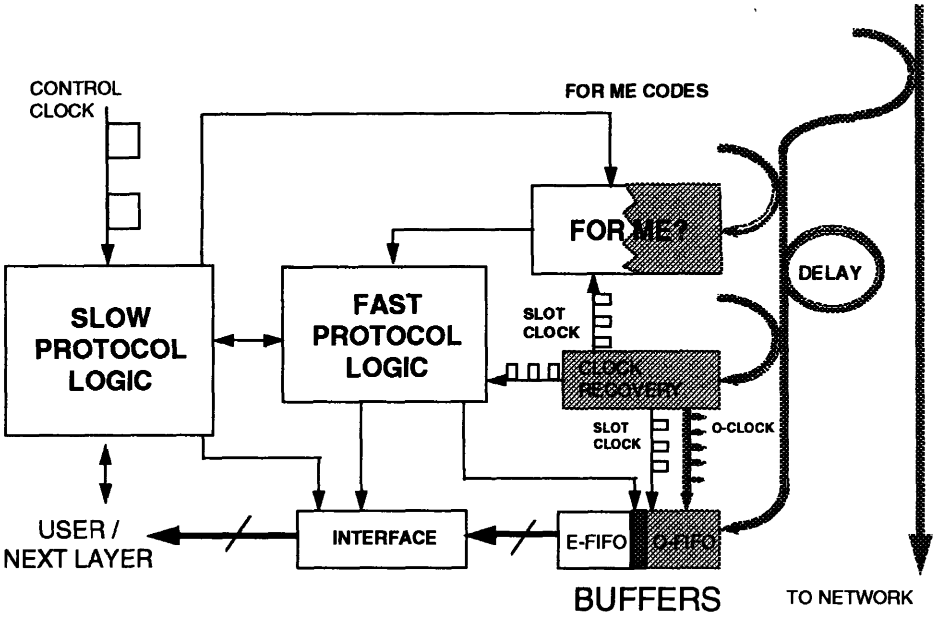

Figure 1.1: ***High Speed Access Node Architecture***

In this thesis, I will discuss a family of devices that address some of the issues relating to the implementation of components for high speed all-optical networks. The main application of these devices is in high speed all optical switching. In particular, we will demonstrate all optical demultiplexing, inverting, AND, XOR, OR and NOR gating. In Chapter 2, I will describe the device geometries investigated in this thesis. I will then provide a brief discussion of nonlinearities in optical fiber and semiconductor laser amplifiers necessary to understand the theoretical aspects of the devices. In Chapter 3, I will present analytic theory for the nonlinear interactions in silica fiber and semiconductor laser amplifiers. Measures of switching performance will be derived. Chapter 4 contains the experimental setup and switching results. In Chapter 5, I will summarize the results and compare them to those obtained from other devices of recent interest.

Chapter 2: Background

In this chapter, I will describe the various interferometric switching geometries presented in this thesis. In order to be able to freely discuss the theoretical analysis of these devices in Chapter 3, I will then briefly present the fundamental theoretical framework for the linear and nonlinear responses in single mode silica fiber. I will finally discuss the basics of semiconductor nonlinearities.

2.1 Device Descriptions

The optical switching devices presented in this thesis are based on a single arm interferometer geometry[7,8,9,10]. The three devices are called the Ultrafast Nonlinear Interferometer (UNI)[11,12], the UNI with counter-propagating control[13,14], and the Single Arm Dual Input Nonlinear Interferometer (SADINI)[15,16]. We have used the UNI geometry to perform 40 Gb/s demultiplexing and bit-wise inversion. The UNI with counter-propagating control allows device cascadibility and an implementation complexity reduction. We have additionally used this geometry to perform all optical OR and NOR gating. Lastly, we have used the SADINI to perform a binary XOR function at 10 Gb/s.

2.1.1 The Mach-Zehnder Nonlinear Interferometer

A large class of optical switches is based on some form of nonlinear interferometer. An example of such a device is the so called Mach-Zehnder (MZ) nonlinear interferometer, shown in Figure 2.1. Light of intensity I_s enters the device and is split, via a 50/50 splitter, into two components. One component travels along the lower arm through a linear material while the other component travels through a nonlinear medium. The two components are subsequently interfered at the output of the device. An additional beam of intensity I_c called the control beam is coupled into the nonlinear medium. Via a nonlinear process call cross phase modulation (as will be described in section 2.3), the control beam changes the index of the nonlinear medium by the factor n_2I_c where n_2 is the so called nonlinear index of refraction. The signal component traveling along the lower path experiences a phase shift in proportion to the linear index, n_0. The component travelling along the upper arm experiences the same linear phase shift in addition to a nonlinear contribution in proportion to the factor n_2I_c. Consequently, the presence of the control light causes a differential phase shift between the two signal components. When these components are interfered at the output, this differential phase shift results in an output intensity change.

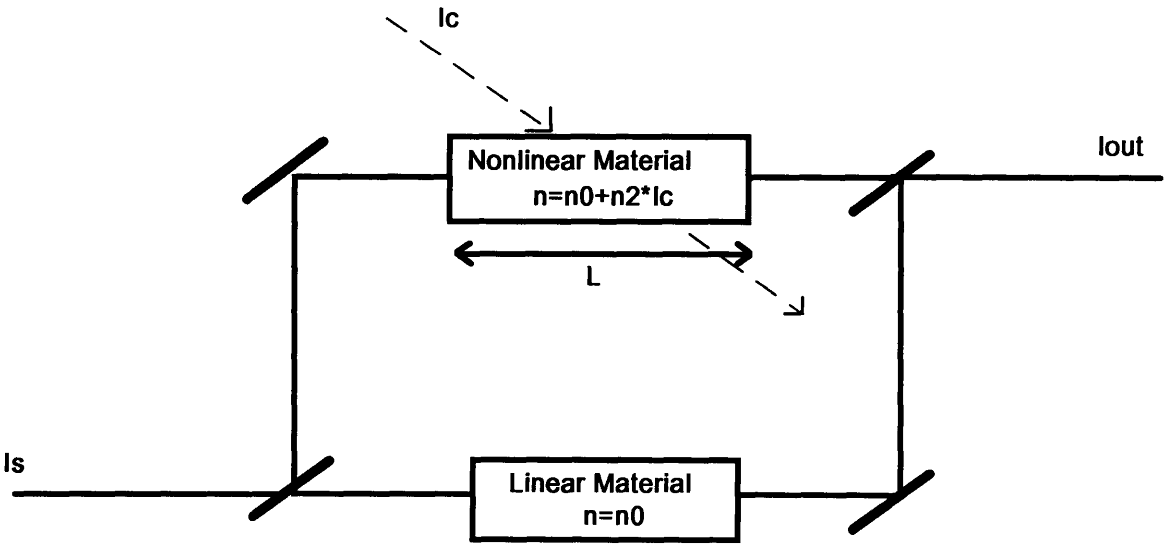

Figure 2.1: ***Mach Zehnder Nonlinear Interferometer***

One may easily verify that the transfer characteristic of the device is:

$$\frac{I_{out}}{I_s} = \cos^2\left(\frac{\phi_b + \Delta\phi_{nl}}{2}\right) \tag{2.1}$$

where ϕ_b is the linear phase bias of the interferometer due to intrinsic path length changes between the upper and lower arm in the absence of the control light, and $\Delta\phi_{nl}$ is the induced nonlinear phase shift via cross phase modulation in the nonlinear medium. The nonlinear phase shift can be related to the nonlinear refractive index and the interaction length in the nonlinear material, L, via the expression: $\Delta\phi_{nl} = \frac{2\pi}{\lambda} n_2 I_c L$ where λ is the wavelength of the signal light. If ϕ_b is 0, the interferometer is said to be biased ON since the signal light is transmitted to the output in the absence of control light. Alternatively, if ϕ_b is π then the interferometer is biased OFF. If one chooses I_c and L such that the $\Delta\phi_{nl}$ is π, then the interferometer can be switched between the ON and OFF state by the presence of the control light. What was just described corresponds to a situation in which the signal and control are CW beams. However, one can now imagine pulse amplitude modulating both streams at rates slower than the response time of the nonlinearity and thereby dynamically switch the interferometer output at high speeds.

Since the induced differential phase shift is linearly proportional to the control pulse intensity, the transfer curve of control intensity vs. output intensity has the same functional form as the above expression. A diagram of the transfer curve for the case of $\phi_b=0$ is shown in Figure 2.2. Only when $I_c=I_{pi}$ will the signal intensity be switched to I_{so}. Thus, the device acts like an AND gate, or equivalently, a demultiplexer. It is important to realize that it has been assumed that $\Delta\phi_{nl}$ is constant over the full width of the signal pulse. In reality, $\Delta\phi_{nl}$ will have a form that depends on the control pulse shape. The effect of temporal non-uniformity in $\Delta\phi_{nl}$ will be analyzed in Section 3.1.

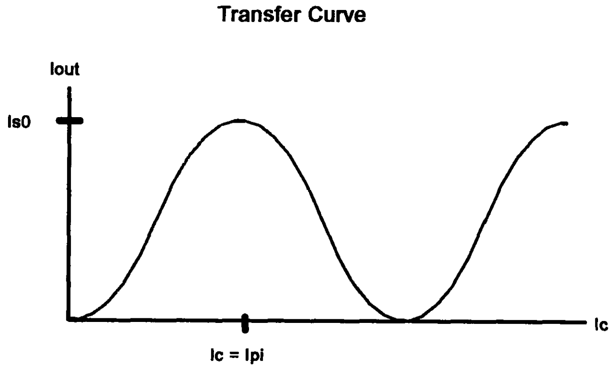
Transfer Curve

AND Truth Table

Is	Ic	Iout
0	0	0
0	Ipi	0
Is0	0	0
Is0	Ipi	Is0

Figure 2.2: ***Nonlinear Interferometer Transfer Curve and AND Truth Table***

One disadvantage of the two arm interferometer concerns long lived phase and gain modulation in the nonlinear material[17]. If the response of the nonlinearity has components with time scales longer than the bit period, then the phase and gain modulation that a particular signal pulse experiences depends on the past history of control pulses. This pattern dependent modulation adversely affects the switching operation of the device since random phase and gain modulation in the nonlinearity maps to random intensity modulation at the output of the interferometer. The physical mechanisms underlying the nonlinear response in semiconductor will be outlined in section 2.4.

2.1.2 The UNI

An alternative to the above geometry is the single-arm interferometer (SAI) or time division interferometer (TDI)[18,19]. Instead of splitting the signal pulse into two components travelling along distinct paths, it is split into two components travelling along the same path, as shown in Figure 2.3. More specifically, the polarization sensitive delay (PSD) splits the signal pulse into two delayed orthogonal polarizations (the two white pulses). The control pulse (black pulse) is then timed to overlap with one signal component, imparting a phase shift via cross phase modulation in the nonlinear material (NLM). The second PSD serves to recombine the two signal components in the same time slot. As before, the two overlapped signal components are interfered at the output via a polarizer (POL.) set at 45° to each polarization. This approach has the advantage that parasitic path length changes due to fabrication non-idealities or environmental changes do not adversely effect the device operation since both signal components travel along the same path. More importantly, however, this single arm implementation circumvents the problems of slow nonlinear recovery times. The reason is that both signal components now experience the long lived phase and gain modulation in the nonlinear material, and thus the relative phase of each pulse is determined exclusively by the fast components of the control induced refractive index change. If one is using fiber as the nonlinear material, the latter is of no consequence because the nonlinear response in fiber has femtosecond time scales, but it now becomes possible to utilize semiconductor for nonlinearity without limiting the bit period to be greater than the slowest response time of the nonlinearity. Thus, the performance of the single arm interferometer with a semiconductor nonlinearity can be greatly improved over the two arm approach. It should be noted, however, that pattern dependent gain modulation still exists, the details of which will be presented in Section 3.2. We call this switching device the Ultrafast Nonlinear Interferometer (UNI). The control pulse is at a different wavelength from the signal so that it may be filtered out at the output of the UNI using a band pass filter (BPF). If the signal and control are sufficiently separated in wavelength, a dichroic coupler (instead of a 50/50 coupler) may be used before the nonlinear material to reduce input coupling loss. If the UNI is biased OFF, the signal pulse is transmitted to the output only in the presence of the control pulse, thus implementing an AND or demultiplexing function. Alternatively, if the UNI is biased OFF, it can be used as an inverter.

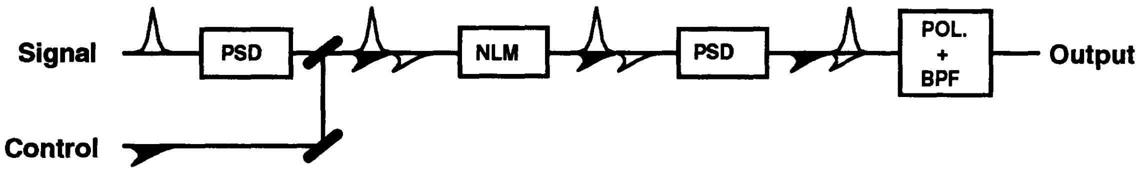

Figure 2.3: *Ultrafast Nonlinear Interferometer (UNI)*

2.1.3 The UNI With Counter-Propagating Control

In the scenario where one is using a semiconductor nonlinearity with a short interaction length (~ 1 mm) in the UNI, a minor modification can relieve the requirement on control filtering. Namely, one can use a counter-propagating control stream timed to overlap with one of the orthogonally polarized signal components in the nonlinear medium, as shown in Figure 2.4. The latter enables both inputs to be at the same wavelength, without filtering. More importantly, however, the device is now cascadable since the output can be used as a control stream for a second gate if all optical streams are at the same wavelength. It is important to realize that the assumption of a short interaction length and large nonlinearity is very important since counter-propagating pulses in a length of fiber will not interact significantly.

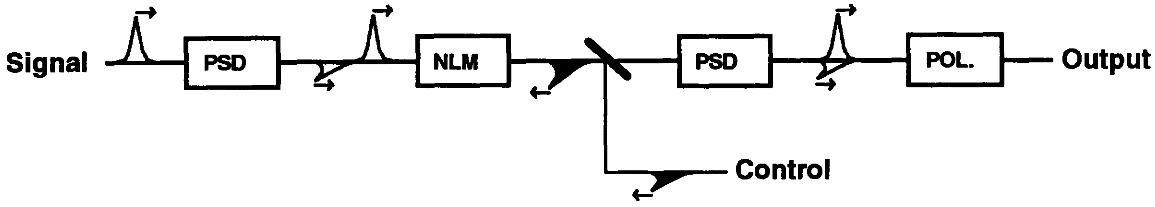

Figure 2.4: *UNI with Counter-Propagating Control*

With the utilization of a semiconductor nonlinearity, an optical NOR gate can be implemented using the UNI geometry, a block diagram of which is shown in Figure 2.5. The operation of the NOR gate relies on cross gain saturation in the semiconductor nonlinearity whereby a control pulse (A or B) depletes the available gain such that an incident signal pulse (Clock) experiences less gain and is thus turned OFF at the output. If the individual intensities of the A and B pulses are sufficient to saturate the gain, then the clock pulse will be turned OFF if either or both of the logical inputs are "1". Alternatively, the Clock pulse will only be transmitted to the output if both A and B are "0", thus implementing a binary NOR function. It is important to note that the index nonlinearity is still used to destructively interfere the signal components at the output. However, for NOR operation, the main mechanism invoked is cross gain saturation to non-interferometrically aid in turning the signal pulse OFF. Similarly, if the UNI is biased OFF, an OR function can be realized primarily by using cross phase modulation.

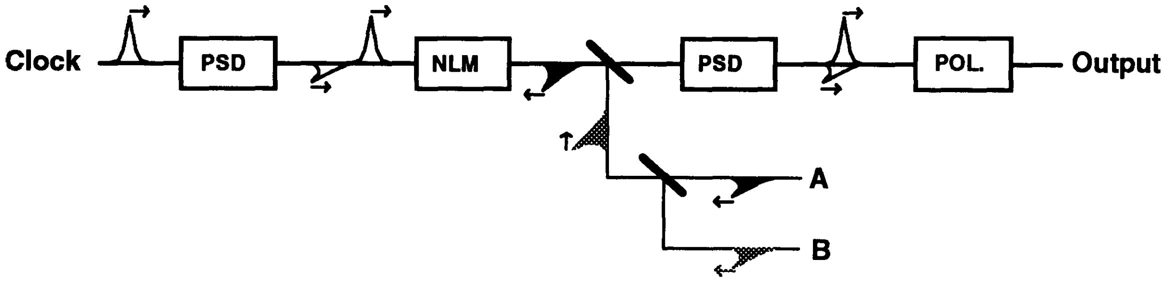

Figure 2.5: *Optical OR/NOR Gate Based on a UNI Geometry*

2.1.4 The SADINI

Although the UNI can be used as a high speed AND gate / demultiplexer, an inverter, and as a OR/NOR gate, it cannot function as a true 3 port (2 input) logic gate. One can go a step further by splitting and interfering the control pulse. The latter has two advantages. Firstly, a filter at the output is not required since the control pulse can be destructively interfered out. As such, both the signal and control can be at the same wavelength. Secondly, an XOR function may now be implemented via the mutual cross phase modulation between intense signal and control pulses. A block diagram of the device is shown in Figure 2.6. An important aspect of the device to keep in mind concerns cascadability. Due to the fashion in which the signal and control pulses are time division multiplexed in the nonlinear medium, the output time slots for each are different. Namely, according to the diagram in Figure 2.6, at the output, the control appears in a time slot delayed at least by a pulse width from the signal. Thus, depending on the input streams, the output logic result may appear in 1 of 2 time slots. Clearly, cascadability is compromised since the output timing is effectively random. By exploiting pulse walk through, however, this problem can be eliminated at the cost of input wavelength symmetry. Although it is important to point out these problems, for some applications, i.e. address recognition, only one XOR gate is required and thus is relatively unaffected by the lack of cascadability.

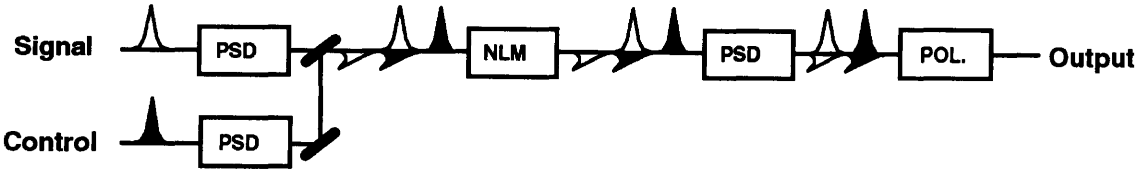

Figure 2.6: ***Single Arm Dual Input Nonlinear Interferometer (SADINI)***

A few words about the biasing conditions of the above device are in order. For demultiplexing operation, both the signal and control must be biased OFF. This may be achieved by setting the polarization sensitive delays at integer multiples of $\lambda/2$ where λ is the appropriate wavelength for signal and control. Thus, the signal is turned ON only in the presence of the control. The interesting new function achievable with the SADINI is the binary XOR function. In this case, both the signal and control must be biased ON by setting the PSD's to integer multiples of λ. As a result, the output is only 0 if both the inputs represent the same binary value. The transfer function SADINI in the case when both inputs are biased ON is easily derived to be:

$$I_{out}(I_s,I_c)=I_s\cos^2\left(\frac{\pi}{2}\frac{I_c}{I_{switch}}\right)+I_c\cos^2\left(\frac{\pi}{2}\frac{I_s}{I_{switch}}\right) \tag{2.2}$$

where I_{switch} is the input intensity required to induce a π phase shift via cross phase modulation. The normalized SADINI transfer curve and XOR truth table are presented in Figure 2.7 in which I_{switch} is normalized to 1 (I_{pi} = 1). As can be seen, the transfer function is a saddle shaped curve that is 0 at vertices with like logical values, and 1 at vertices with opposite logical values, thus implementing an binary XOR function. It is important to keep in mind that the transfer function in Figure 2.6 was derived by assuming uniform phase shifts over the entire signal and control pulses giving rise to perfect switching. This assumption is appropriate for a scenario in which the input pulses are essentially rectangular. A close approximation to a rectangular pulse, however, is a super Gaussian pulse of the form $x(t) \propto e^{-(\frac{t}{\tau})^{2n}}$ for large integer n.

Transfer Function

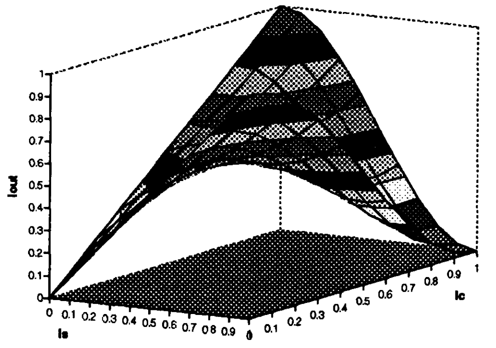

XOR Truth Table

Is	Ic	Iout
0	0	0
0	Ipi	Ipi
Ipi	0	Ipi
Ipi	Ipi	0

Figure 2.7: ***SADINI Transfer Curve and XOR Truth Table***

2.2 Overview of Relevant Nonlinear Materials

Silica fiber and semiconductor have been the primary materials utilized to demonstrate optical switching, but for different reasons. Semiconductors, notably GaAs, have large nonlinearities, at least in comparison to fiber. Moreover, semiconductor based switching enables device integration and its consequent reliability and packaging. However, the dynamics of semiconductor nonlinearities have bound electron contributions with sub-picosecond recovery times, in addition to free carrier contributions with recovery times approaching a few nanoseconds. Thermal effects with ms time scales are also present. In general, these slower nonlinearities limit the achievable device throughputs. However, the family of devices based on the single arm interferometer are immune to these long lived effects as discussed previously. Nonlinearities in fiber, on the other hand, have femtosecond recovery times and thus, picosecond switching is attainable. The price, however, is the fact that the nonlinearities are much weaker than in semiconductor requiring interaction lengths on the order of kilometers. The low loss in current fiber has been the enabling factor in fiber based switching experiments. In the switching demonstrations we present in this thesis, we have used kilometer lengths of silica fiber and millimeter lengths of InGaAs semiconductor for nonlinearities. To facilitate the theoretical device analysis in Chapter 3, I will present a basic treatment of the linear response of silica fiber in section 2.3, nonlinearities in fiber in section 2.4, and finally, semiconductor nonlinearities in section 2.5.

2.3 The Linear Response of Silica Fiber

2.3.1 Dispersion

The fabrication of low loss silica fiber with mode loss coefficients of 0.2 dB/km at 1.55 µm was first demonstrated as recently as 1979 yielding. Moreover, bandwidths supportable by single mode fiber are in excess of 10 THz allowing high density time division and wavelength division multiplexing. These figures have been the driving forces behind the commercialization and utilization of optical fiber in communications systems.

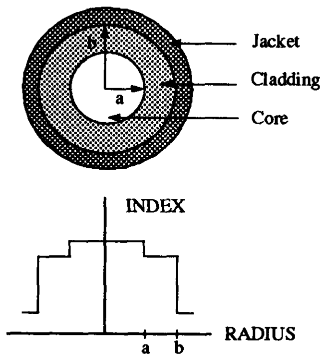

Figure 2.8:

Step Index Fiber Geometry

The simplest realization of optical fiber consists of a silica core surrounded by a lower index cladding layer. Figure 2.8 shows this basic fiber geometry. The transverse mode profiles are obtained by solving the wave equation in cylindrical coordinates for the given step structure. The result is that the transverse modes are linear combination of Bessel functions. One may define a normalized frequency for the waveguide that facilitates the determination of the number of transverse modes supportable[20]:

$$V = \frac{2\pi}{\lambda} a \sqrt{n_1^2 - n_2^2} \tag{2.3}$$

where λ is the wavelength of the incident light, a is the core radius, n_1 and n_2 are the core and cladding refractive indices respectively. By solving the eigenvalue equation for the step index fiber, one finds that single mode operation (higher modes are cut-off) corresponds to a normalized frequency of $V = 2.405$. Thus, if the geometrical parameters of the fiber are designed to meet this condition for the wavelengths of interest, single mode propagation is guaranteed. To satisfy the above criterion, single mode fibers have typical core radii of 2-4 μm and cladding radii on the order of 50-60 μm. The precise cladding radius is not particularly critical as long as it is large enough to sufficiently confine the field modes.

Apart from loss, the linear response of optical fiber is primarily characterized by its dispersion parameters. In fact, chromatic dispersion is the fundamental limiting mechanism in long distance linear propagation schemes. The reason for the latter is that dispersion induced pulse broadening leads to intersymbol interference and, consequently, the achievable bit error rate degrades. Dispersion arises from the wavelength dependence of the refractive index which causes different frequency (wavelength) components of a pulse to travel at different speeds along the fiber. The dispersion parameters are defined by expanding the mode propagation constant around the center frequency of the incident light[21], ω_0.

$$\beta = \beta_0 + \beta_1(\omega - \omega_0) + \frac{1}{2}\beta_2(\omega - \omega_0)^2 + \frac{1}{6}\beta_3(\omega - \omega_0)^3 + \cdots$$

$$\beta_m = \left[\frac{\partial^m \beta}{\partial \omega^m}\right]_{\omega=\omega_0} \tag{2.4}$$

β_0 is the center wavelength propagation constant, β_1 is the inverse group velocity, and β_2 is related to pulse broadening. Higher order dispersion (β_3, β_4, etc) can be neglected for the pulse widths of interest in this thesis. The dispersion zero wavelength, λ_0, of optical fiber is defined to be that wavelength at which β_2 vanishes. For normal single mode fiber, λ_0 is around 1.27 μm. However, the dispersion has contributions not only from material dispersion, but also from waveguide dispersion. By varying the geometrical fiber parameters, namely the core radius and the core to cladding index ratio, thus affecting waveguide dispersion, the dispersion zero can be shifted to the 1.55 μm range. Such fiber is termed dispersion shifted fiber. Most of the fiber utilized in the device implementations in this thesis is dispersion shifted. A plot of β_2 vs λ for the dispersion shifted fiber used in this thesis is shown in Figure 2.9. Note the dispersion zero around 1.547 μm.

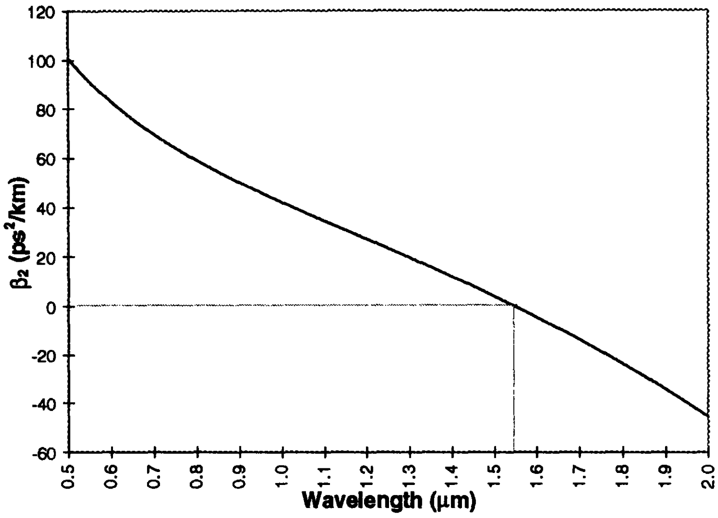

Figure 2.9: β_2 *vs* λ

Given the dispersion parameters as defined above, one can write the differential equation that governs linear pulse propagation in fiber[22].

$$\frac{\partial A}{\partial z}+\beta_1\frac{\partial A}{\partial t}+\frac{1}{2}j\beta_2\frac{\partial^2 A}{\partial t^2}+\frac{1}{2}\alpha A=0 \qquad (2.5)$$

where A is the complex electric field amplitude, α and is the mode loss coefficient. In obtaining this equation, it was assumed that the field could be written as a product of a slowly varying amplitude and a rapidly varying phase term. Thus, this equation is valid for pulse widths satisfying $\frac{\Delta\omega}{\omega} << 1$, i.e. the spectral width is much smaller than the absolute frequency. The latter constraint implies that pulsewidths of interest must be greater than ~ .1 ps. For convenience, one may now move to a reference frame that travels at the group velocity of the pulse by making the substitution: T = t-(z/v_g). Normalizing the mode amplitude via the substitution: $A(z,T)=\sqrt{P_0}e^{-\frac{1}{2}\alpha z}u(z,T)$ where P_0 is the pulse peak power, one obtains a simplified propagation equation[23]:

$$j\frac{\partial u}{\partial z}=\frac{1}{2}\beta_2\frac{\partial^2 u}{\partial T^2} \qquad (2.6)$$

Fourier transforming this equation yields an ordinary differential equation in z which can be solved to obtain the spectrum of the pulse as a function of distance. Inverse Fourier transforming the spectrum yields the time domain pulse shape[24]:

$$u(z,T) = \frac{1}{2\pi}\int_{-\infty}^{\infty} U(0,\omega)\, e^{(-\frac{1}{2}j\beta_2\omega^2 z + j\omega T)}\, d\omega \tag{2.7}$$

where U(z,ω) is the Fourier transform of u(z,T) defined by $U(z,\omega) = \int_{-\infty}^{\infty} u(z,T)\, e^{-j\omega T}\, dT$.

Eq. 2.5 shows that the effect of GVD is to multiply the pulse spectrum by a phase term that is quadratic in frequency and linear in distance. Thus, the power spectrum remains invariant over propagation, but the actual time domain pulse shape changes. Moreover, the pulse becomes linearly chirped, i.e. the instantaneous carrier frequency changes across the pulse. This chirping mechanism can be used to one's advantage in pulse compression. In chapter 4, I will discuss the scheme I used to linearly compress the pulses from a gain switched DFB laser. Moreover, to be able to derive semi-analytic results for device performance measures in Chapter 3, I will need the following results on Gaussian pulse propagation in fiber.

2.3.2 Gaussian Pulse Propagation

One starts with a complex Gaussian pulse shape to account for an initial linear chirp. Thus,

$$u(0,T) = e^{-\frac{(1+jC)}{2}\frac{T^2}{T_0^2}} \tag{2.8}$$

where C is the so called chirp parameter and T_0 is the initial pulse width. Note that T_0 is related to the more familiar full width at half maximum (FWHM) via the relation $T_{FWHM} = 2\sqrt{\ln 2}\, T_0$. The above complex pulse shape is composed of the product of a real Gaussian and a complex quadratic phase term. The time derivative of the phase gives rise to the linear frequency chirp, as desired. The spectrum of the input pulse is obtained via the Fourier transform:

$$U(0,\omega) = \sqrt{\frac{2\pi T_0^2}{1+jC}}\, e^{-\frac{1}{2}\frac{\omega^2 T_0^2}{(1+jC)}} \tag{2.9}$$

Note that the spectral FWHM increases as $\sqrt{1+C^2}$. The latter enables one to estimate the magnitude of the chirp parameter by measuring the product of the temporal and spectral FWHM. Unchirped pulses are termed transform limited since their time bandwidth product equals 1. Finally, one may obtain the output pulse profile by evaluating Eq. 2.5 with the initial spectral shape in Eq. 2.7. The result is[25]:

$$u(z,T)=\sqrt{\frac{T_0^2}{T_0^2-j\beta_2 z(1+jC)}}\,e^{-\frac{(1+jC)T^2}{2[T_0^2-j\beta_2 z(1+jC)]}} \tag{2.10}$$

The output pulse shape is still a complex Gaussian but with modified temporal width and chirp. Note that the temporal pulse width as a function of distance now depends on the chirp parameter. The measure of interest is the ratio of the output to input pulse widths which is found to be[26]:

$$R=\sqrt{(1+\frac{C\beta_2 z}{T_0^2})^2+(\frac{\beta_2 z}{T_0^2})^2} \tag{2.11}$$

The above equation predicts monotonic pulse broadening for $\beta_2 C > 0$. For $\beta_2 C<0$, however, the pulse narrows to a minimum width and subsequently monotonically broadens. At the minimum width, the pulse becomes fully unchirped. Intuitively, if the initial chirp is opposite in sign from β_2, GVD in the fiber imposes a chirp that exactly opposes the initial chirp for a given critical distance. The pulse compression results from the fact that the GVD causes wavelengths at the leading edge to travel slower than those at the trailing edge. After a distance $z=\frac{C}{1+C^2}\frac{T_0^2}{|\beta_2|}$, the incident pulse achieves its minimum width equal to $\frac{T_0}{\sqrt{1+C^2}}$. Thus, the larger the initial chirp, the larger the achievable pulse compression. In Chapter 4.1.1, these last two expressions will be used to estimate the length of fiber required to optimally compress gain switched pulses.

2.4 Nonlinearities in Fiber

2.4.1 Index Nonlinearities due to Third Order Polarization

The devices presented in this thesis are realizable primarily by exploiting nonlinearities in fiber and semiconductors. Thus, it is instructive to briefly discuss the origins of nonlinearities and the basic theoretical framework required to analyze simple devices. One begins by expanding the induced polarization as a power series in the applied electric field. In the frequency domain, it looks like[27]:

$$\begin{aligned}\mathbf{P}(\omega) = \varepsilon_0[&\chi^{(1)}(\omega)\cdot\mathbf{E}(\omega)+\\&\chi^{(2)}(\omega{:}\omega_1,\omega_2){:}\mathbf{E}(\omega_1)\mathbf{E}(\omega_2)+\\&\chi^{(3)}(\omega{:}\omega_1,\omega_2,\omega_3)\vdots\mathbf{E}(\omega_1)\mathbf{E}(\omega_2)\mathbf{E}(\omega_3)+\cdots]\end{aligned}\tag{2.12}$$

where ε_0, is the permittivity of free space, **E** is the incident field, $\chi^{(i)}$ is the i^{th} order susceptibility tensor of rank i+1. $\chi^{(1)}$ is the familiar linear susceptibility, the real part of which gives rise to the linear index. The imaginary part of $\chi^{(1)}$ is responsible for linear loss / gain. It can be shown that $\chi^{(2)}$ is 0 for media that have inversion symmetry[28] (fiber is isotropic and thus has inversion symmetry) and, as a result, second harmonic generation is generally not observed in optical fiber. $\mathrm{Re}\{\chi^{(3)}\}$ gives rise to third harmonic generation (THG)[29], four wave mixing (FWM)[30], and the nonlinear refractive index (which is actually a degenerate form of FWM but deserves distinction)[31]. These three nonlinear optical processes are due to interactions among 4 fields. THG refers to the degenerate mixing process where 3 fields of the same frequency mix to create a field at the third harmonic. The nonlinear refractive index arises from mixing of 2 fields at ω and 1 field at $-\omega$ to create a field at ω. Lastly, FWM refers to the general case where three fields of arbitrary frequency mix to yield a new field whose frequency is formed from sums and / or differences of the source field frequencies. Third harmonic generation requires precise phase matching conditions to be effective. Since third harmonic phase matching is not achieved in fiber without the utilization of special techniques, and the effects of non-degenerate four wave mixing between well separated wavelengths can be filtered out, I will only consider the effects of nonlinear refraction. The primary nonlinear contribution to the polarization is $\mathbf{P}_{\mathrm{NL}}(\omega) = \varepsilon_0 \chi^{(3)}(\omega) \vdots \mathbf{EEE}$. It should be pointed out that $\mathrm{Im}\{\chi^{(3)}\}$ is responsible for a nonlinear absorption process such as 2 photon absorption (TPA). For the present purposes, I will ignore this effect because the TPA coefficient in fiber is small. Moreover, in semiconductor, TPA becomes important only at high optical powers. As such, from now on, I will drop the Re{} notation for $\chi^{(3)}$. In the time domain, the polarization is, in general, a convolution of the applied electric field and the time domain susceptibility function as follows[32]:

$$\mathbf{P}_{\mathrm{L}}(\mathbf{r},t) = \varepsilon_0 \int_{-\infty}^{\infty} \chi^{(1)}(t-\tau) \cdot \mathbf{E}(\mathbf{r},\tau) d\tau \qquad (2.13)$$

$$\mathbf{P}_{\mathrm{NL}}(\mathbf{r},t) = \varepsilon_0 \iiint \chi^{(3)}(t-\tau_1, t-\tau_2, t-\tau_3) \vdots \mathbf{E}(\mathbf{r},\tau_1)\mathbf{E}(\mathbf{r},\tau_2)\mathbf{E}(\mathbf{r},\tau_3) d\tau_1 d\tau_2 d\tau_3$$

First, I consider the case of a single incident field at frequency ω with arbitrary polarization and its modulation of the local index of refraction. Thus, the input field is represented by[33]:

$$\mathbf{E}(\mathbf{r},t) = \frac{1}{2}\{\hat{\mathbf{x}}E_x(\omega) + \hat{\mathbf{y}}E_y(\omega)\}e^{-j\omega t} + c.c \qquad (2.14)$$

Substituting the above equation into Eq. 2.11 gives the nonlinear polarization contribution[34]:

$$\begin{aligned} P_x(\omega) &= \frac{3}{4}\varepsilon_0 \chi_{xxxx}\{(|E_x|^2 + \frac{2}{3}|E_y|^2)E_x + (E_x^* E_y)E_y\} \\ P_y(\omega) &= \frac{3}{4}\varepsilon_0 \chi_{xxxx}\{(|E_y|^2 + \frac{2}{3}|E_x|^2)E_y + (E_y^* E_x)E_x\} \end{aligned} \qquad (2.15)$$

In obtaining Eq. 2.15, it was assumed that the nonlinear response is instantaneous, i.e. $\chi^{(3)}$ is dispersionless and time independent. In the case of fiber, the relevant nonlinearities react on femtosecond time scales. Thus, over the pulse bandwidths of interest in this thesis (< 100 GHz), $\chi^{(3)}$ is effectively instantaneous. Moreover, for isotropic media, the relation $\chi_{xxxx} = \chi_{xxyy} + \chi_{xyxy} + \chi_{xyyx}$, was invoked. The last term in Equation 2.15, responsible for coherent coupling, averages to 0 over propagation distances much greater than a polarization beat length. Thus, for strongly birefringent fiber, it may be ignored, but for the fiber utilized in the devices presented in the thesis, it cannot be considered negligible.

An arbitrary input polarization may be obtained by setting $E_x(\omega)$ to be real and $E_y(\omega) = \sqrt{a}e^{j\phi}E_x(\omega)$. Substituting these relations into Eq. 2.15 gives the induced nonlinear x and y polarizations[35]:

$$\begin{aligned} P_x^{(3)}(\omega) &= \frac{1}{4}\varepsilon_0\chi_{xxxx}|E_x|^2 E_x[3 + a(2 + e^{j2\phi})] \\ P_y^{(3)}(\omega) &= \frac{1}{4}\varepsilon_0\chi_{xxxx}|E_y|^2 E_y[3e^{-j\phi} + \frac{1}{a}(2 + e^{-j2\phi})] \end{aligned} \tag{2.16}$$

From the above equations it can be seen that an elliptically polarized incident wave can be rotated due to the index anisotropy induced by the nonlinearity. However, a linearly polarized wave does not experience a polarization change. Self phase modulation is the effect that refers to the index modulation of Δn_x due to $|E_x|^2$ and Δn_y due to $|E_y|^2$. If we now define the nonlinear index, $n_2 = \frac{3}{8n}\mathrm{Re}\{\chi_{xxxx}^{(3)}\}$ where n is the linear refractive index, we obtain the index change due to self phase modulation for each orthogonal polarization: $\Delta n_j = n_2|E_j|^2$ where j is x or y. The index modulation due to an orthogonally polarized field component may be called cross phase modulation. However, it is important to distinguish between cross phase modulation due to orthogonal polarization components of the same field and wavelength, and cross phase modulation between 2 distinguishable fields at different wavelengths. The latter effect will be described in the next section.

To investigate the nonlinear interaction of two distinguishable beams, i.e. pump and probe, one typically considers two cases. By definition, the probe is a weak signal one uses to "probe" the material and the pump is a strong signal one uses to modulate the material properties and thus the phase and amplitude of the probe. The first scenario is one in which both the pump and probe are linearly polarized along the x direction. Thus, $E_x=E_s+E_p$ and $E_y=0$. Substituting these relations into Eq. 2.16., ignoring terms involving the probe intensity, and assuming that the phases of the pump and probe are incoherent across the region of nonlinear interaction, renders the nonlinear index change that the probe experiences due to the pump[36]: $\Delta n_x^s = \frac{3}{4n}\chi_{xxxx}|E_p|^2 = 2n_2|E_p|^2$. The second case is where the pump and probe are orthogonally linearly polarized, i.e. E_x=E_s, E_y=E_p. Executing the same prescription as above yields: $\Delta n_x^s = \frac{1}{4n}\chi_{xxxx}|E_p|^2 = \frac{2}{3}n_2|E_p|^2$. All these results can be summarized as follows. 1) Cross phase modulation between two distinguishable fields of the same polarization is twice as effective as self phase modulation. 2) Cross phase modulation between two distinguishable fields of the same polarization is 3 times as effective as cross phase modulation between distinguishable fields of orthogonal polarizations. 3) Cross phase modulation between orthogonal polarization components of the same field is 2/3 as effective as self phase modulation.

The most general case of arbitrary polarization and 2 distinguishable fields is more difficult to analyze because the evolution of each beam's polarization must be taken into account. The only practical method of analysis is numerically solving the coupled nonlinear wave equation as presented in the next section.

2.4.2 Nonlinear Wave Equation for Fiber

The linear wave equation in fiber may be modified to include the Kerr effect via the introduction of a nonlinear driving term as follows[37]:

$$\frac{\partial A}{\partial z} + \beta_1 \frac{\partial A}{\partial t} + \frac{1}{2} j\beta_2 \frac{\partial^2 A}{\partial t^2} + \frac{\alpha}{2} A = j\gamma |A|^2 A \tag{2.17}$$

where is the α mode loss coefficient, $\gamma = \frac{n_{2,eff}\omega_0}{cA_{eff}}$ where $n_{2,eff} = \frac{3}{8n}\mathrm{Re}\{\chi_{xxxx}^{(3)}\}$, A_{eff} is the effective modal area in the fiber core, and ω_0 is the center frequency of the soliton. In the derivation of the above equation, it was assumed that the electric field is linearly polarized so that nonlinear polarization rotation, as described in the last section, is not present. Eq. 2.17 can be normalized via the substitutions: $u = \sqrt{\frac{\gamma\tau^2}{|\beta_2|}}A$, $x = \frac{z}{L_D}$, $T = \frac{t}{\tau}$, $\Gamma = \frac{\alpha}{2}L_D$

where $L_D = \frac{\tau^2}{|\beta_2|}$ and τ is the pulse width. The normalized Nonlinear Schröedinger Equation (NLSE) with loss thus becomes[38]:

$$j\frac{\partial u}{\partial x} + \frac{1}{2}\frac{\partial^2 u}{\partial T^2} + |u|^2 u = -j\Gamma u \tag{2.18}$$

If Γ=0, the above equation can be solved analytically via an inverse scattering transform[39] to yield soliton solutions. The fundamental soliton is represented by[40]:

$$u(x,T) = \operatorname{sech}(T) e^{j\frac{x}{2}} \tag{2.19}$$

The primary property of interest is the invariance of the intensity pulse shape with distance. In fact, this is the reason why solitons have attracted considerable attention in the development of high data rate long haul transmission systems. The peak soliton power, P_1, required to maintain a fundamental soliton depends on the dispersion and pulse width in the following manner: $P_1 = \frac{|\beta_2|}{\gamma\tau^2}$. Thus, the lower the dispersion, the less peak power required. Moreover, the product of the peak power and the pulse width squared must be invariant for soliton propagation. The latter relation is referred to as the fixed area constraint for solitons. If Γ is not 0, a perturbational approach may be used to solve Eq. 2.16 within the regime of interest. Alternatively, the salient features of the soliton, such as the root mean square (r.m.s.) pulse width, spectral width, and chirp, may be calculated given an initial pulse shape.

In the case of an arbitrary input polarization, the evolution of the orthogonal field amplitudes may be described by a set of coupled differential equations that incorporate the polarization dependent nonlinearities as discussed in section 2.3. More specifically, the self and cross phase modulation terms are included, in addition to the phase-mismatch-dependent coherent coupling terms. The coupled equations are[41]:

$$\begin{aligned} \frac{\partial A_x}{\partial z} + \beta_{1x}\frac{\partial A_x}{\partial t} + \frac{1}{2}j\beta_2\frac{\partial^2 A_x}{\partial t^2} + \frac{\alpha}{2}A_x &= j\gamma\left(|A_x|^2 + \frac{2}{3}|A_y|^2\right)A_x + \frac{1}{3}j\gamma A_x^* A_y^2 e^{-2j\Delta\beta z} \\ \frac{\partial A_y}{\partial z} + \beta_{1y}\frac{\partial A_y}{\partial t} + \frac{1}{2}j\beta_2\frac{\partial^2 A_y}{\partial t^2} + \frac{\alpha}{2}A_y &= j\gamma\left(|A_y|^2 + \frac{2}{3}|A_x|^2\right)A_y + \frac{1}{3}j\gamma A_y^* A_x^2 e^{2j\Delta\beta z} \end{aligned} \tag{2.20}$$

We can now write a set of equations that describe the evolution of two co-propagating fields with distinct frequencies, which is the scenario of interest for device analysis. It is important that the spectra of the two co-propagating fields do not overlap so that coherent coupling terms between distinct fields can be ignored. We begin by defining the following useful vectors and matrices.

$$\mathbf{A}=\begin{pmatrix} A_x \\ A_y \end{pmatrix};\ \mathbf{B}=\begin{pmatrix} B_x \\ B_y \end{pmatrix};\ \boldsymbol{\beta}_{\mathbf{1A}}=\begin{pmatrix} \beta_{1Ax} & 0 \\ 0 & \beta_{1Ay} \end{pmatrix};\ \boldsymbol{\beta}_{\mathbf{1B}}=\begin{pmatrix} \beta_{1Bx} & 0 \\ 0 & \beta_{1By} \end{pmatrix}$$

$$\mathbf{Q_x}=\begin{pmatrix} 1 & 0 \\ 0 & 0 \end{pmatrix};\ \mathbf{Q_y}=\begin{pmatrix} 0 & 0 \\ 0 & 1 \end{pmatrix};\ \mathbf{R_{SPM}}=\begin{pmatrix} 1 & 0 \\ 0 & 2/3 \end{pmatrix};\ \mathbf{R_{XPM}}=\begin{pmatrix} 2 & 0 \\ 0 & 2/3 \end{pmatrix}$$

A and B are the field variables whose components are their orthogonal polarization components. $\boldsymbol{\beta}_{\mathbf{1j}}$ are the inverse group velocity matrices, $\mathbf{Q_j}$ are projection matrices onto the jth polarization component, and $\mathbf{R_{SPM/XPM}}$ contain the required factors to describe phase modulation between all four polarization components. With the above definitions in hand, one can write down the two coupled vector equations for the two distinct fields. Note that superscript † is the Hermitian operator (conjugate transpose).

$$\left(\frac{\partial}{\partial z}+\boldsymbol{\beta}_{\mathbf{1A}}\frac{\partial}{\partial t}+\frac{1}{2}j\beta_{\mathbf{2A}}\frac{\partial^2}{\partial t^2}+\frac{\alpha}{2}\right)\mathbf{A}=$$

$$j\gamma_A\begin{pmatrix} \mathbf{A}^{\dagger}\mathbf{R_{SPM}}\mathbf{A}+\mathbf{B}^{\dagger}\mathbf{R_{XPM}}\mathbf{B} & 0 \\ 0 & \frac{2}{3}\left(\mathbf{A}^{\dagger}\mathbf{R_{SPM}^{-1}}\mathbf{A}+\mathbf{B}^{\dagger}\mathbf{R_{XPM}^{-1}}\mathbf{B}\right) \end{pmatrix}\mathbf{A}$$

$$+\frac{1}{3}j\gamma_A\begin{pmatrix} \mathbf{A^T Q_y A}e^{-2j\Delta\beta_{A1}z} & 0 \\ 0 & \mathbf{A^T Q_x A}e^{2j\Delta\beta_{A1}z} \end{pmatrix}\mathbf{A}^*$$

$$\left(\frac{\partial}{\partial z}+\boldsymbol{\beta}_{\mathbf{1B}}\frac{\partial}{\partial t}+\frac{1}{2}j\beta_{\mathbf{2B}}\frac{\partial^2}{\partial t^2}+\frac{\alpha}{2}\right)\mathbf{B}=$$

$$j\gamma_B\begin{pmatrix} \mathbf{B}^{\dagger}\mathbf{R_{SPM}}\mathbf{B}+\mathbf{A}^{\dagger}\mathbf{R_{XPM}}\mathbf{A} & 0 \\ 0 & \frac{2}{3}\left(\mathbf{B}^{\dagger}\mathbf{R_{SPM}^{-1}}\mathbf{B}+\mathbf{A}^{\dagger}\mathbf{R_{XPM}^{-1}}\mathbf{A}\right) \end{pmatrix}\mathbf{B}$$

$$+\frac{1}{3}j\gamma_B\begin{pmatrix} \mathbf{B^T Q_y B}e^{-2j\Delta\beta_{B1}z} & 0 \\ 0 & \mathbf{B^T Q_x B}e^{2j\Delta\beta_{B1}z} \end{pmatrix}\mathbf{B}^* \qquad (2.21)$$

As before, the left hand sides of Eq. 2.21 are the linear operators for dispersion and loss, while the two terms on the right hand side are the nonlinear driving terms that include self / cross phase modulation and coherent coupling terms. Eq. 2.21 can be solved numerically via the computationally efficient split step Fourier method. Stress induced polarization scattering (birefringence induced by fiber bending, etc) may be modeled roughly by scrambling the polarization at certain points along the simulation.

2.5 Nonlinearities in Semiconductor

The characterization of semiconductor optical nonlinearities is considerably more complicated than the fiber case, the primary reason being that many physical mechanisms with widely varying time scales contribute to the nonlinearity. Moreover, one can not ignore gain nonlinearities in the semiconductor case since they typically play an important role in the switching characteristics of semiconductor based devices. A considerable amount of work has been done on the characterization of optical nonlinearities in semiconductors and the investigation of associated physical mechanisms. K. Hall, et. al., have done an extensive study of ultra-fast nonlinearities in InGaAsP diode amplifiers via pump probe measurements, utilizing optical pulses with durations less than 200 fs[42]. The ultra-fast (sub-picosecond) nonlinear response of the diodes was modeled by an impulse response composed of a sum of exponentials representing the effects of the underlying physical mechanisms. A delta function was additionally included in the impulse response to account for two photon absorption (TPA). The theoretical impulse response was then fitted numerically to the pump probe data to estimate the time constants and magnitudes of the nonlinearities. The long lived effect, due to pump induced carrier density changes which relax on the time scale of the upper state lifetime (~ 1 ns) was modeled by a unit step response since it does not relax appreciably on the time scale of the pump probe measurement (~ 10 ps).

In this thesis, we are interested in optical data streams of 10 to 100 Gb/s which use pulses with 1 to 10 ps FWHM. Consequently, the impulse response functions of Hall et. al. should be modified accordingly. More specifically, the sub-picosecond nonlinearities can be modeled as instantaneous since their recovery times are shorter than the optical pulsewidths considered. In the high bit rate regime (100 Gb/s), however, one could include a term in the impulse response that accounts explicitly for the slowest contribution to the sub-picosecond effects. Such a contribution (carrier heating for example) has a time constant of around 600 fs. The long lived nonlinearities, on the other hand, cannot be modeled as a unit step since they are clearly visible on the time scales of tens of bit periods. Thus, one should model the long lived effects by an exponential impulse response with a 100 ps to 1 ns time constant. The mathematical formalism behind this modeling will be dealt with in Chapter 3.

Chapter 3: Device Analysis

In this chapter, I will analyze the nonlinear interactions between signal and control pulses in silica fiber and semiconductor. In particular, we are concerned with how to customize the interaction parameters in order to achieve certain desired device performance measures. The metrics we use in this chapter are switching efficiency which determines the achievable logical "0" to "1" contrast ratio, the degree of output pulse distortion, and the sensitivity to timing jitter. In section 3.1.1, I will present analytical results for cross-phase modulation in fiber between pulses with no walk-off or pulse distortion. Although this scenario is probably the simplest case to analyze, it is appropriate for accurately modeling the performance of a demultiplexer using the UNI or SADINI. Section 3.1.2 contains a more involved analysis that takes into consideration pulse walk-through, in addition to pulse distortion due to group velocity dispersion (GVD) and self phase modulation (SPM). This model is useful for predicting the device performance of a logic gate based on the SADINI with a fiber nonlinearity. A very brief discussion of soliton switching is presented in Section 3.1.3 as a model for fiber switches in the very high bit rate regime (100 Gb/s and beyond).

In Section 3.2, I will present theoretical results and simulations of the effects on device performance of cross-phase modulation (XPM) and cross-gain saturation (XGS) in a semiconductor nonlinearity. We adopt a mathematical model of the relevant nonlinearities based on the work of Hall, et. al., due to its intuitive appeal and analytical simplicity. Both the co- and counter-propagating control pulse scenarios are analyzed in order to compare the device performance of the UNI under these two conditions.

3.1 Theoretical Analysis of Fiber Switches

3.1.1 Model of Switch with No Pulse Walk-Through

For demultiplexing using the SADINI, we set both the signal and control wavelengths to be the same and close to the dispersion zero of the fiber to avoid pulse distortion and signal / control walk-off. Consequently, one may derive a simple model for the gate that ignores pulse distortion of the signal and control pulses due to group velocity dispersion (GVD). Moreover, even if self phase modulation broadens the spectrum of the signal, the pulse will not be distorted by GVD. Loss is easily incorporated into this simple model via the definition of an effective interaction length.

We begin by defining the temporal intensity profiles of the input signal and control pulses to be Gaussian with widths τ_s and τ_c respectively. In addition, the control pulse is offset relative to the signal pulse by time T. Thus,

$$\begin{aligned} I_s(t) &= I_{s0} e^{-(\frac{t}{\tau_s})^2} \\ I_c(t) &= I_{c0} e^{-(\frac{t+T}{\tau_c})^2} \end{aligned} \tag{3.1}$$

For the purposes of demonstrating the calculation, from now on we will follow the phase shift accumulated by the signal and the consequent output signal pulse shape and energy. It should be noted, however, that the control pulse also experiences cross phase due to the signal, the calculations for which are analogous. Because the signal and control pulses suffer no distortion and maintain their overlap, the nonlinear phase shift profile that the signal experiences is simply the pulse profile of the control multiplied by appropriate factors. Thus, the nonlinear phase shift accumulated by the signal pulse is:

$$\Delta\phi_{nl}^{s}(t) = \frac{2\pi}{\lambda_s} n_{2_{XPM}} I_c(t) L \tag{3.2}$$

where λ_s is the signal wavelength, $n_{2_{XPM}}$ is the effective nonlinear refractive index, and L is the interaction length. It should be noted that the relationship between $n_{2_{XPM}}$ and $\chi^{(3)}$ will depend explicitly on the polarization of both the signal and control pulses within the nonlinear material, the details of which are presented in Chapter 2. To obtain the switching efficiency, ζ, defined as the ratio of the switched energy to the input energy, we integrate the input and output signal pulse intensity profiles over time. The output pulse profile is simply the input pulse profile multiplied by the temporal interference pattern due to the nonlinear interaction. More specifically,

$$E_{in}^{s} = \int_{-\infty}^{\infty} A I_s(t)dt = \sqrt{\pi} I_{s0} A \tau_s \tag{3.3}$$

$$E_{out}^{s} = A\int_{-\infty}^{\infty} I_s(t)\cos^2\left(\frac{\Delta\phi_{nl}^{s}(t)+\phi_b^{s}}{2}\right)dt = A\int_{-\infty}^{\infty} I_{s0} e^{-(\frac{t}{\tau_s})^2} \cos^2\left[\frac{\pi}{\lambda_s} n_2 I_{c0} L e^{-(\frac{t+T}{\tau_c})^2} + \frac{\phi_b}{2}\right]dt$$

where A is the effective modal area of the beam in the nonlinear material, $\Delta\phi_{nl}^{s}(t)$ is the phase shift imparted to the signal pulse via cross phase modulation (XPM), and ϕ_b^{s} is the linear bias of the interferometer. We will assume that the signal pulse is biased ON and that we are trying to switch it off, i.e. $\phi_b=0$. If we now make the substitutions, $u=\frac{t}{\tau_s}$, $w=\frac{\tau_c}{\tau_s}$, $u_0=\frac{T}{\tau_s}$, $\phi_0=\frac{2\pi}{\lambda_s} n_{2_{XPM}} I_{c0} L$, and simplify the integral kernel, we obtain the desired switching ratio:

$$R=\frac{E_{out}^{s}}{E_{in}^{s}}=\frac{1}{2}+\frac{1}{2\sqrt{\pi}}\int_{-\infty}^{\infty} e^{-u^2}\cos[\phi_0 e^{-(\frac{u+u_0}{w})^2}]du \tag{3.4}$$

Note that ϕ_0 is the peak phase shift imparted to the signal. The simplest case is that of identical signal and control widths and perfect overlap, i.e. w=1 and u_0 = 0. Since we are trying to switch the signal off, we would like R to be as small as possible or, alternatively, the switching efficiency, ζ=1-R, to be maximized. Since the above equation has only one parameter that is free to chose, namely ϕ_0, we minimize R as a function of ϕ_0. Numerically, one finds that the minimum R obtainable is .2236 (~78% switching efficiency). The required peak phase shift for this is ϕ_0=3.73. It is not surprising that the peak phase shift, occurring at the center of the signal pulse, is greater than π since the Gaussian pulse profile does not impart a uniform phase shift across the whole signal pulse. Thus, the optimal peak phase shift is higher than π so that the rest of the signal pulse suffers moderate phase shifts. The fact that the peak phase shift is greater than π, however, causes some pulse distortion after the two orthogonal signal components are interfered. More specifically, the center of the pulse will not be switched OFF or ON as well as the side lobes. Figure 3.1a depicts both the switched OFF and switched ON output pulse shapes for the optimal parameters derived above.

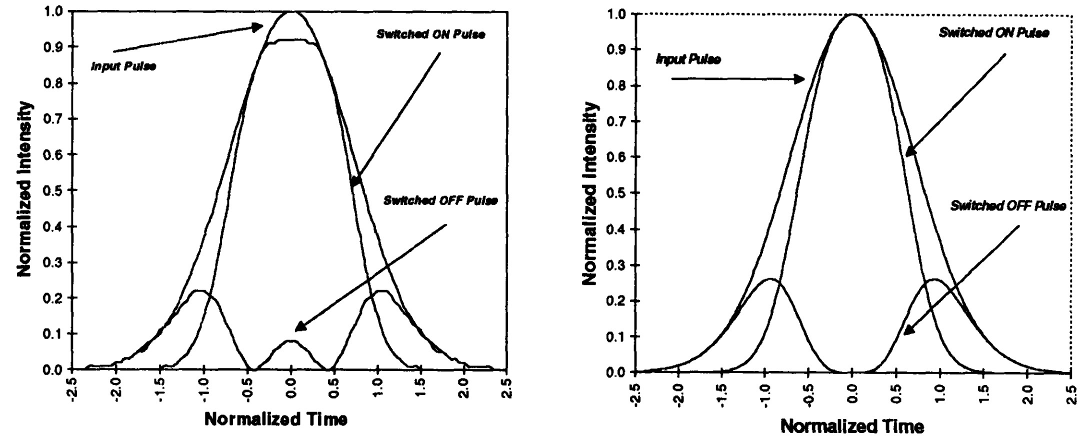

Figure 3.1a and 3.1b

Output Pulse Profiles for Peak Phase Shifts of (a) 3.73 and (b) π

Such pulse distortion is disadvantageous from a device perspective since cascadability is clearly affected. Thus, one may instead choose a peak phase shift of π at the expense of switching efficiency. The question then arises as to the exact trade off between peak phase shift and switching efficiency. Figure 3.2 is a plot of peak phase shift versus R and Figure 3.1b depicts the output pulse shape for a peak phase shift of π. As can be seen from these plots, the switched OFF and ON pulses more closely resemble the shape of input pulse in the case of π peak phase shift as opposed to a peak phase shift of 3.73. However, the switched OFF pulse still exhibits pulse shaping effects due to non-uniform phase shifts.

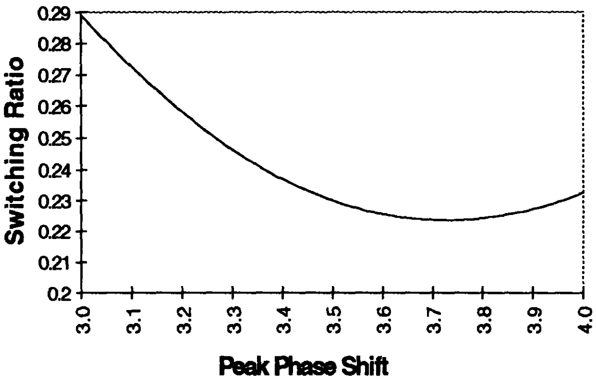

Figure 3.2: ***Effects of Peak Phase Shift on Switching Ratio***

The 78% optimal switching efficiency derived above is slightly disappointing from a device perspective since it limits the 0 to 1 contrast ratio and thus the ultimate bit error rate of the switch. Moreover, the non-uniformity of the phase shift profile was shown to lead to adverse pulse shaping effects. However, there are simple changes that can considerably improve the contrast ratio without adversely affecting the output pulse shape. One obvious option is to increase the pulse width of the control pulse so that the signal pulse sees a more uniform phase shift across its entirety. Figure 3.3b depicts the optimal R as a function of w where w is the control to signal pulse width ratio. This plot was generated by varying w and minimizing R as a function of ϕ_0. Figure 3.3a depicts the required peak phase shift to obtain the optimal switching ratio. As can be seen, the switching efficiency approaches 1 (the switching ratio approaches 0) as the control pulse becomes larger relative to the signal pulse. Asymptotically, the signal pulse suffers a uniform π phase shift across its width. As the control pulse becomes narrower relative to the signal pulse, the switching efficiency goes to 0 and the optimal peak phase shift goes to 4.06. The longer control pulse has solved 2 problems. Namely, the inefficient switching and adverse pulse shaping. Unfortunately, it is at the cost of asymmetry between the inputs to the gate. If, however, the gate was used as a demultiplexer, the asymmetry is not all that bad since the control pulse is interfered out at the output. Of course, the signal intensity must be sufficiently low so that the control pulse does not experience significant phase shifts and consequent loss of full destructive interference at the output.

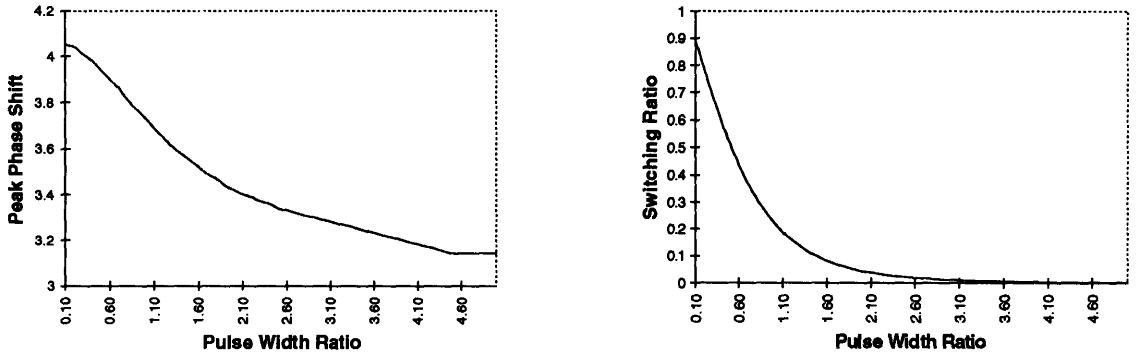

Figure 3.3a and 3.3b:

Effects of Pulse Width Ratio on Optimal Phase Shift (a) and Switching Ratio (b)

A final issue relating to the simple model above is that of timing jitter. It is instructive to consider the effect of small timing errors at the input to the gate because real systems with multiple optical components are likely to be subject to timing jitter. More specifically, input timing jitter causes non-optimal overlap of signal and control pulses in the nonlinear material which ultimately causes degradation of switching efficiency and, as we will see, asymmetry in the output pulse profiles. To investigate this issue, we ran simulations in which the timing offset, u_0, between signal and control was varied. The resulting output pulse profiles and switching efficiencies were then recorded. Figure 3.4 depicts the effect of timing jitter, normalized to the pulse width, on the switching ratio, R. As before, the linear bias of the interferometer is 0, and we are trying to switch the signal pulse OFF.

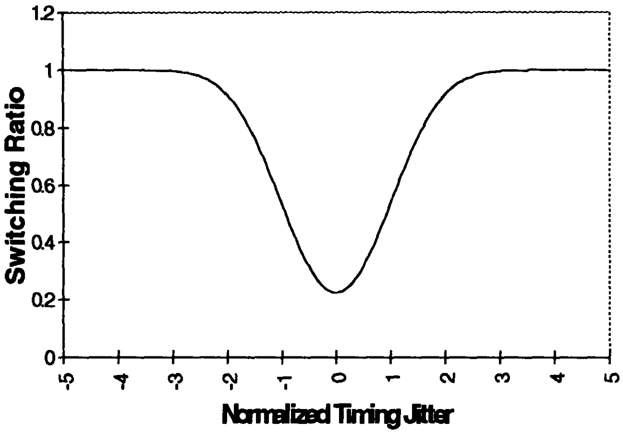

Figure 3.4: ***Effect of Timing Jitter On Switching Ratio***

As can be seen from Figure 3.4, a timing jitter of half a pulse-width degrades the switching efficiency from 77% to about 70%. In real systems, the normalized timing jitter is expected to be much less than 0.5. The device is relatively insensitive to timing jitter. It should be pointed out that the no-walk-through switch is considerably more sensitive to timing jitter than the walk-through switch, as we will see in the next section. Moreover, it is important to realize that the figure of merit we have used here for sensitivity to timing jitter is the switching efficiency. Although this metric may be appropriate for the case of an isolated inverter or XOR gate where we want simply to minimize the output energy in the "0" case, it clearly is not a good metric for demultiplexing operation where the quality of the switched out pulses is extremely important. The reason for the latter, is that the demultiplexed stream is likely to undergo subsequent transmission and processing. Timing jitter not only causes a reduction in switching efficiency, but more importantly in some cases, asymmetry in the switched out pulse shapes. Consequently, one should recognize that Figure 3.4 represents a good metric for timing jitter only in the regime of small timing offsets where asymmetry in the output pulse is insignificant.

Lastly, the effect of loss may easily be incorporated in this model by introducing an effective length, L_{eff}, instead of the actual interaction length in the equations above. The analytical results are easily changed via the substitution: $L_{eff} = \frac{1-e^{-\alpha_l L}}{\alpha_l}$ where α_I is the intensity loss coefficient. With the above results in hand, one may roughly estimate the control peak required to impart a π peak phase shift to the signal pulse using silica fiber for nonlinearity. It is important to remember that the model just presented assumes that the signal and control pulses travel at the same velocity and thus are overlapped over the entire interaction length.

For purposes of the power estimation, we assume optimal overlap (i.e. $u_0=0$), and identical signal and control pulse widths. Furthermore, for simplicity, we assume that the polarizations of the interacting signal and control pulses remain linear and orthogonal over the entire length of fiber (i.e. no polarization scattering). As a result, $n_{2_{XPM}}$ is related to $\chi^{(3)}_{xxxx}$ in the following manner:

$$n_{2_{XPM}} = \frac{1}{4n}\chi^{(3)}_{xxxx} \approx 2.3*10^{-16}\frac{cm^2}{W}$$

Finally, the fiber loss is taken to be 0.25 dB/km which translates into an intensity loss coefficient of $\alpha_I=5.75*10^{-2}$ km^{-1}. Thus, for L=10 km, L_{eff}=7.6 km. Finally, recognizing that the pulse power is I*A where A is the effective fiber core area = 50 μm^2, we solve for P_{peak} in the following relation:

$$\phi_{peak} = \frac{2\pi}{\lambda_s} n_{2_{XPM}} \frac{P_{peak}}{A} L_{eff} = \pi \qquad (3.5)$$

which renders P_{peak} = 222 mW. If the control stream has a 10:1 duty ratio, then the required average control power is 22.2 mW. Such a power is easily generated using Erbium Doped Fiber Amplifiers (EDFA's).

3.1.2. Model of Walk-Through Switch

In the case of XOR operation using the SADINI, both arms are biased ON. To obtain good logical 0:1 contrast ratio, it is important that uniform π phase shifts are imparted to signal and control in the case when both input pulses are present. As we saw in the last section, a nonlinear interaction with no walk through leads to phase profiles that track the pulse shapes. Even though the previous analysis showed that arbitrarily good switching efficiency can be obtained by appropriately choosing the pulse width ratio, requiring two different input pulse widths compromises the symmetry of the gate. By this I mean that the two inputs to the gate become distinguishable, and as such, the device becomes difficult to cascade. More serious is the fact that the signal and control pulses experience different phase shifts as a result of the asymmetry. Thus, for logic gate operation, the input pulse widths should be comparable. In the next section, we consider the effects of input wavelength asymmetry. This allows pulse walk-through which, as will be shown, allows one to optimize switching efficiency without altering the pulse width ratio. The simple model derived in the last section is, however, still very applicable to demultiplexing operation. The model to be derived next, on the other hand, is more appropriate for logic gate operation of the SADINI.

A more general model of the device can additionally incorporate the effects of pulse walk-through, group velocity dispersion and self phase modulation which become important for high intensity short pulses. As a result, the evolution of the signal and control pulse shapes through the nonlinear material cannot be overlooked because it has a direct impact on the output pulse shapes and efficiency of switching. Unfortunately, the added complexity is at the cost of non-analytic results. In the next section, the main equation for the phase shift profiles is derived. Numerical simulation based on that equation is then presented.

We begin with the pulse intensity profiles and incorporate their evolution as a function of time, t, and length along the nonlinear material, x. We assume unchirped Gaussian pulse shapes for signal and control with time dependent centers and widths to account for GVD and SPM. The assumption of unchirped input pulses is appropriate to modeling the setup I implemented. The input pulse shapes are:

$$
\begin{aligned}
I_s(x) &= I_{s0}(t)e^{-(\frac{x-x_{s0}(t)}{\Gamma_s(t)})^2} e^{-\alpha x} \\
I_c(x) &= I_{c0}(t)e^{-(\frac{x-x_{c0}(t)}{\Gamma_c(t)})^2} e^{-\alpha x}
\end{aligned}
\tag{3.6}
$$

where I_{s0} and I_{c0} and the peak intensities of the pulses, x_{s0} and x_{c0} and the points on the x axis of the moving peaks of the pulses, Γ_s and Γ_c are the evolving pulse widths, and α is the intensity loss coefficient in the nonlinear material which is assumed to be approximately the same for both the signal and control. In addition, the product of the peak intensity and the pulse width must be a time invariant constant (determined by the initial conditions) to satisfy the fixed area constraint of GVD/SPM. The peak centers move as a function of time according to

$$
\begin{aligned}
x_{s0}(t) &= x_{s0}(t_0) + v_s t \\
x_{c0}(t) &= x_{c0}(t_0) + v_c t
\end{aligned}
\tag{3.7}
$$

where t_0 is the initial time of evolution, and v_s and v_c are the group velocities of the signal and control pulses respectively. The pulse widths evolve in a manner consistent with the effects of GVD and SPM. Higher order dispersion is not considered because the pulse widths of interest are not small enough for third order dispersion (TOD) or fourth order dispersion (FOD) to become important. Arguably the only condition in which TOD should be considered is that in which the signal or control pulses are at the dispersion zero of the material. In such cases, TOD leads to asymmetric broadening of the pulse involving dispersive oscillatory structures that take energy away from the central part of the pulse. These wings, however, typically would not be effective in imparting significant phase shift to another pulse. Thus, the primary contribution of TOD to the phase profile is due to a reduction in peak power of the control pulse. We can write down the pulse evolution equations as a function of time[43].

$$
\begin{aligned}
\Gamma_s(t) &= v_s \tau_{s0} \sqrt{(1+\frac{\beta_{2s}\gamma_s(v_s t)^2}{\tau_{s0}^2})^2 + (\frac{\beta_{2s} v_s t}{\tau_{s0}^2})^2} \\
\Gamma_c(t) &= v_c \tau_{c0} \sqrt{(1+\frac{\beta_{2c}\gamma_c(v_c t)^2}{\tau_{c0}^2})^2 + (\frac{\beta_{2c} v_c t}{\tau_{c0}^2})^2}
\end{aligned}
\tag{3.8}
$$

where β_{2j} are the GVD parameters as described in Chapter 2, τ_{j0} and the initial pulse widths, γ_j are the nonlinear coefficients defined by the relation $\gamma_j = \frac{2\pi}{\lambda_j} n_{2_{SPM}} I_{j0}(t_0)$. Thus, the nonlinear index due to cross phase modulation that the signal and control see at point x in space as a function of time are

$$\begin{aligned} \Delta n_s(t,x) &= n_{2_{XPM}} I_{c0}(t) e^{-\left(\frac{x - x_{c0}(t)}{\Gamma_c(t)}\right)^2} e^{-\alpha x} \\ \Delta n_c(t,x) &= n_{2_{XPM}} I_{s0}(t) e^{-\left(\frac{x - x_{s0}(t)}{\Gamma_s(t)}\right)^2} e^{-\alpha x} \end{aligned} \tag{3.9}$$

To determine the output pulse profiles, we now transform to a reference frame that moves with the pulse centers so that the absolute distance coordinate vanishes. This is accomplished via the Galilean transformations:

$$\begin{aligned} &\text{Signal Transformation: } x = x_{s0}(t) + x_s \\ &\text{Control Transformation: } x = x_{c0}(t) + x_c \end{aligned} \tag{3.10}$$

where x_s and x_c are the points on the signal and control pulses relative to their respective moving centers. Looking in this new coordinate system gives the temporal index changes for the signal and control pulses:

$$\begin{aligned} \Delta n_s(t,x_s) &= n_{2_{XPM}} I_{c0}(t) e^{-\left(\frac{\Delta x_0 + vt + x_s}{\Gamma_c(t)}\right)^2} e^{-\alpha[x_{s0}(t) + x_s + v_s t]} \\ \Delta n_c(t,x_c) &= n_{2_{XPM}} I_{s0}(t) e^{-\left(\frac{-\Delta x_0 - vt + x_c}{\Gamma_s(t)}\right)^2} e^{-\alpha[x_{c0}(t) + x_c + v_c t]} \end{aligned} \tag{3.11}$$

The accumulated phase shift profiles are calculated by integrating the above expressions over the interaction time, t which is equivalent to integrating over the interaction length, the more customary routine. Executing the temporal integral, we obtain the phase modulation profiles for the signal and control pulses:

$$\begin{aligned} \Delta\phi_s(x_s,\Delta x_0) &= \frac{2\pi}{\lambda_s} v_s \int_{t_0}^{T=L/v_s} \Delta n_s(t,x_s)\,dt \\ \Delta\phi_c(x_c,\Delta x_0) &= \frac{2\pi}{\lambda_c} v_c \int_{t_0}^{T=L/v_c} \Delta n_c(t,x_c)\,dt \end{aligned} \tag{3.12}$$

To obtain the output temporal pulse profiles, we again transform via the substitutions:

$$\begin{aligned} &\text{Signal Transformation: } x = v_s t_s \text{ ; } \Delta x_0 = v_s \Delta t_0 \\ &\text{Control Transformation: } x = v_c t_c \text{ ; } \Delta x_0 = v_c \Delta t_0 \end{aligned} \tag{3.13}$$

where t_j are now the time indices for the observed output pulse in the time domain. Finally, one may derive the output pulse profiles by multiplying by the interference term.

$$\begin{aligned} I_{out}^{s}(t_s) &= I_{s0}(t) e^{-(\frac{t_s}{\tau_s(T)})^2} e^{-\alpha L} \cos^2[\frac{\Delta\phi_s(t_s, \Delta t_0) + \phi_b^s}{2}] \\ I_{out}^{c}(t_c) &= I_{c0}(t) e^{-(\frac{t_c}{\tau_c(T)})^2} e^{-\alpha L} \cos^2[\frac{\Delta\phi_c(t_c, \Delta t_0) + \phi_b^c}{2}] \end{aligned} \tag{3.14}$$

As in the simplified model, it should be noted that the relationship between $n_{2_{XPM,SPM}}$ and $\chi^{(3)}$ is determined by the polarization states of the signal and control pulses. Lastly, the above expressions can be integrated over t_j to obtain the output pulse energies.

Clearly, exact analytical results will be impossible to get. However, a few approximations may be made at this point to accommodate an analytical solution. Firstly, we will ignore the pulse broadening effect on the modulation profile but will continue to incorporate the x dependence of the intensity due to dispersive spreading. The error thus introduced into the nonlinear phase profile comes primarily from the wings of the control pulse. Secondly, we will neglect the second term within the square root in the pulse width evolution equation (Eq. 3.8). This is valid if the main contribution to dispersive spreading is due to self phase modulation, i.e. the peak powers are high. Finally, the remaining term will be approximated by an exponential to accommodate the analytical solution. Again, for means of demonstration, we will follow the signal pulse and its associated phase modulation profile. We begin from equation 3.12 and remember that $I_{c0}(t)\Gamma_c(t) = I_{c0}(t_0)\Gamma_c(t_0)$. We make the following approximation for $I_{co}(t)$[44]:

$$I_{c0}(t)=\frac{I_{c0}(t_0)\Gamma_c(t_0)}{\Gamma_c(t)}=\frac{I_{c0}(t_0)}{\sqrt{(1+\frac{\beta_2\gamma_c(v_ct)^2}{\tau_{c0}^2})^2+(\frac{\beta_2 v_c t}{\tau_{c0}^2})^2}}\approx\frac{I_{c0}(t_0)}{1+\frac{\beta_2\gamma_c(v_ct)^2}{\tau_{c0}^2}}$$

$$\approx I_{c0}(t_0)[1-\frac{\beta_2\gamma_c v_c^2}{\tau_{c0}^2}t^2]\approx I_{c0}(t_0)e^{-(\frac{\beta_2\gamma_c v_c^2}{\tau_{c0}^2})t^2} \tag{3.15}$$

Now we can analytically perform the integral in Eq. 3.14 ignoring the time dependence of the control pulse width and transform to the output signal time index to render the following functional form:

$$\Delta\phi_s(t_s)\approx\frac{2\pi}{\lambda_s}n_{2_{XPM}}I_{c0}(t_0)v_s\tau_{c0}\sqrt{\frac{\pi}{4}\frac{v_s^2}{v_{eff}^2+v^2}}$$

$$*\exp\left[\frac{\alpha v v_s^2\Delta t_0-v_{eff}^2(\frac{\Delta t_0}{\tau_{c0}})^2-\alpha(v_{eff}^2+v^2)x_{s0}(t_0)+\frac{1}{4}\alpha^2\tau_{c0}^2v_s^4}{v_{eff}^2+v^2}\right]$$

$$*\exp\left[\frac{(\alpha v v_s v_c-\alpha v_{eff}^2 v_s-2v_{eff}^2\frac{\Delta t_0}{\tau_{c0}^2})t_s-\frac{1}{4}v_{eff}^2(\frac{t_s}{\tau_{c0}})^2}{v_{eff}^2+v^2}\right]$$

$$*\left(erf\left[\frac{v(\frac{t_s+\Delta t_0}{\tau_{c0}})+\frac{1}{2}\alpha v_s^2t_{c0}+\frac{L}{\tau_{c0}}(\frac{v_{eff}^2+v^2}{v_s^2})}{\sqrt{v_{eff}^2+v^2}}\right]\right.$$

$$\left.-erf\left[\frac{v(\frac{t_s+\Delta t_0}{\tau_{c0}})+\frac{1}{2}\alpha v_s^2\tau_{c0}}{\sqrt{v_{eff}^2+v^2}}\right]\right) \tag{3.16}$$

where we have introduced the effective velocity, $v_{eff}^2 = \frac{\beta_2 \gamma_c v_c^2}{\tau_{c0}^2}$. A corresponding phase profile for the control pulse can be written that is similar to Eq. 3.16. One can see that if loss and dispersion are 0, the phase profile is a difference of two error functions. Thus the phase profile is relatively flat over the region of pulse walk-through and falls off on both sides in approximately one pulse width. The introduction of loss and dispersion serve to asymmetrize the phase profiles because the leading edge sees less phase shift due to the decreased intensity of the control pulse. Consequently, the trailing edge of the signal pulse will be more effectively phase modulated and thus switched out. Even if one accounts for the asymmetrical effects of loss and dispersion, the phase profiles attainable with walk through of signal and control pulses are considerably more uniform than those of the simpler scenario analyzed previously[45]. Thus, one would expect that much better switching efficiencies are attainable with a pulse walk through scheme as compared to the constant overlap scenario with comparable signal and control pulse widths. In the next section, I will present results of numerical simulations conducted for the general model just described. Computer code has been written to implement the full prescription from Eq. 3.6 to Eq. 3.14, without approximation. A listing of the simulation code may be found in section 6.1.

Since the main feature of the general model is the inclusion of pulse distortion effects, it is very important to be able to accurately estimate the dispersion parameters for the fiber in question. As will be explained in the next chapter, dispersion shifted fiber was used for nonlinearity. The manufacturers of the particular fiber purchased provided a model for the dispersion parameter D(λ) that is very accurate over the range of wavelengths we are interested in, namely those within the erbium band. The dispersion is accurately represented by the following relation:

$$D(\lambda) = \frac{S_0 \lambda}{4}[1 - (\frac{\lambda_0}{\lambda})^4] \qquad (3.17)$$

where the parameters S_0 and λ_0 are provided by the manufacturer. S_0 is called the dispersion slope and λ_0 the dispersion zero. For the particular fiber used for the experiment, S_0=0.067 ps/nm^{2}km and λ_0=1547 nm. As shown in chapter 2, β_2 and D are related by $\beta_2(\lambda) = -\frac{\lambda^2}{2\pi c} D(\lambda)$. The third order dispersion parameter is used to calculate the group velocities of the signal and control. As such, one needs the following equations to obtain β_3.

$$\beta_3(\lambda) = \frac{d\beta_2(\omega)}{d\omega} = -\frac{\lambda^2}{2\pi c}\frac{d}{d\lambda}\left\{-\frac{\lambda^2}{2\pi c}D(\lambda)\right\} = \left(\frac{\lambda^2}{2\pi c}\right)^2\left\{\frac{dD}{d\lambda} + 2\frac{D}{\lambda}\right\} \qquad (3.18)$$

$$\frac{dD}{d\lambda}(\lambda) = \frac{S_0}{4}[1 + 3(\frac{\lambda_0}{\lambda})^4]$$

To accurately determine the group velocities of the signal and control, we begin with the propagation constant expansion around the dispersion zero of the fiber.

$$\beta(\omega) = \beta_{00} + \beta_{10}(\omega - \omega_0) + \frac{1}{2}\beta_{20}(\omega - \omega_0)^2 + \frac{1}{6}\beta_{30}(\omega - \omega_0)^3 + \cdots$$

$$\beta_{m0} = \left[\frac{\partial^m \beta}{\partial \omega^m}\right]_{\omega=\omega_0} \qquad (3.19)$$

where ω_0 is the dispersion zero frequency, NOT the center frequency of the pulse. The inverse group velocity equals $\frac{\partial\beta}{\partial\omega}$. Thus, taking the derivative of Eq. 3.20 and realizing that β_{20}=0 at the dispersion zero yields:

$$v_g^{-1}(\omega) = \beta_{10} + \frac{1}{2}\beta_{30}(\omega - \omega_0)^2 \qquad (3.20)$$

Finally, β_{10} ~ 1.445/c and β_{30} may be calculated by evaluating Eq. 3.20 at the dispersion zero.

For the purposes of simulating the nonlinear interaction, parameters were chosen to be commensurate with a 5 Gb/s system using full pulse walk through. As such, both input pulses have a 25 ps FWHM and a peak power of 1/3 W, as shown in Figure 3.5. From now on, I will no longer make the distinction between signal and control since both pulses have comparable intensity in the simulation scenario. As such, the two inputs will now be called A and B.

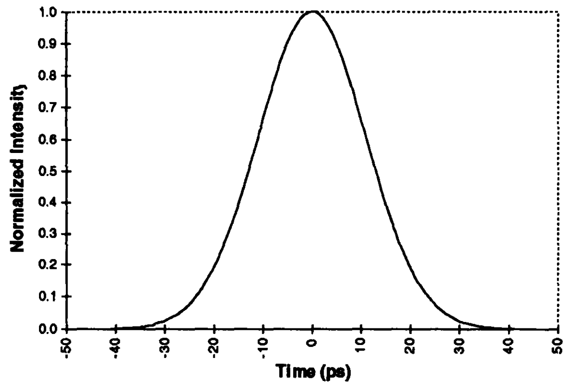

Figure 3.5: ***Input Pulse Shapes***

To obtain pulse walk-through, the A to B timing offset is set to 25 ps. More specifically, pulse B initially lags pulse A by 25 ps. To obtain relatively flat phase profiles, the walk through was chosen to be 50 ps. The wavelengths that enable a 50 ps walk through are λ_A = 1560.2 nm, λ_B = 1547 nm. Pulse B was chosen to be at the dispersion zero to minimize pulse distortion due to SPM/GVD. Pulse A was chosen to be in the anomalous dispersion regime to take advantage of slight pulse narrowing. The phase modulation profiles are shown in Figures 3.6a and 3.6b.

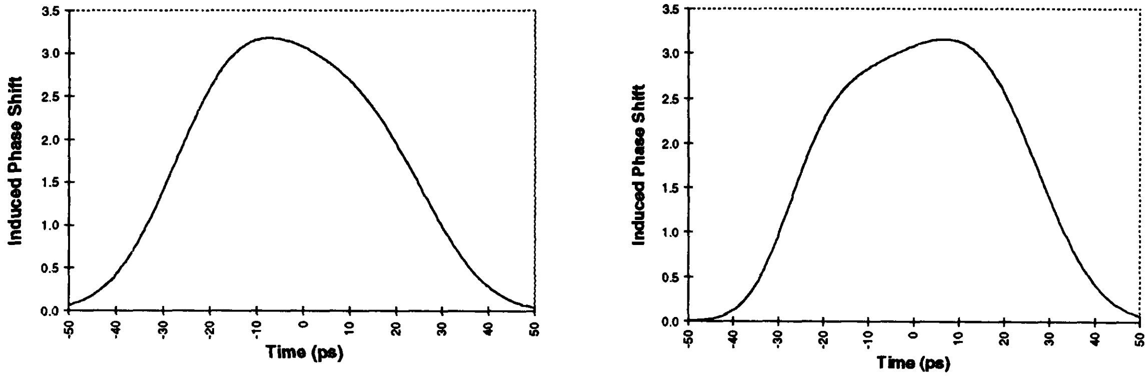

Figure 3.6a and 3.6b

Phase Modulation Profiles for Pulse A (a) and Pulse B (b)

Figure 3.7a and 3.7b demonstrate that a pulse walk through scenario enables more uniform phase profiles for the same pulse widths than the degenerate wavelength case. The phase profiles are relatively uniform ($\Delta\phi$ ~ [2.5, 3.14] radians) over a 20 to 25 ps interval. Since the pulse widths are on this order, most of the pulse should be effectively phase modulated. This phase uniformity should allow better switching extinction ratios and thus better switching efficiencies. Indeed, that is the case as will be shown in the next section. A notable feature of the above profiles is the temporal asymmetry. As alluded to before, loss and dispersion due to SPM/GVD causes this asymmetry. Since Pulse B initially lagged Pulse A, its leading edge is more effectively phase modulated as evidenced by Figure 3.6b. Similarly, the trailing edge of Pulse A is more effectively phase modulated. As the walk through occurs, the intensity of each pulse decreases and consequently, the nonlinear phase shifts decrease.

The output pulse shapes are obtained via Eq. 3.14 and are shown in Figure 3.7a,b. As a reference, the output pulse shape in the absence of phase modulation are also plotted. Figure 3.8a,b depict an enlarged view of the output pulse shape. As can be seen, the walk-through case produces much higher extinction ratios than the degenerate wavelength case due ultimately to the higher uniformity of the phase modulation profiles. Again, the asymmetry in the output pulse profiles is due to loss and GVD/SPM induced pulse distortion. Lastly, the effects of propagation in the anomalous dispersion regime can be seen in the unmodulated output pulse shape in Figure 3.7a. The output pulse width of pulse A, in the absence of switching, has decreased from 25 ps to 16.5 ps. The enlarged plots in Figure 3.8a,b exhibit side lobes due to sub-optimal phase modulation similar to the degenerate wavelength case. Note, however, that on the full scale in Figure 3.7a,b, these pulse shaping effects are not particularly important.

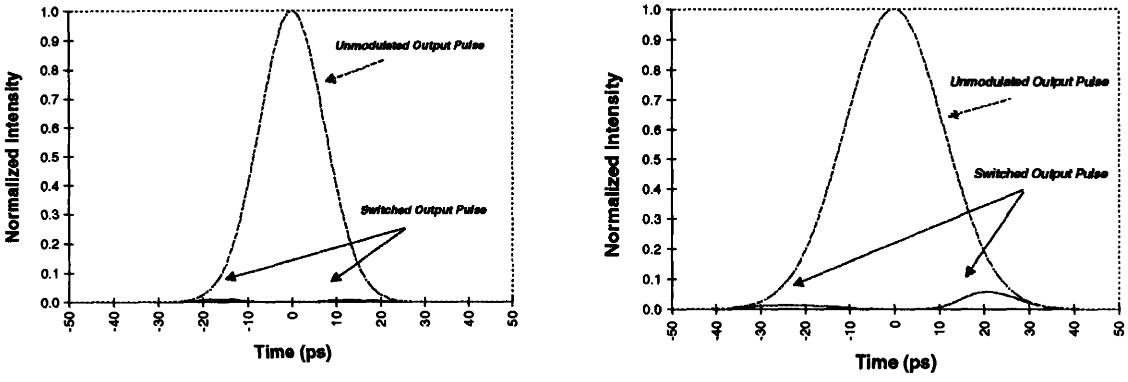

Figure 3.7a and 3.7b

Modulated and Unmodulated Output Pulse Shapes, Pulse A (a) and Pulse B (b)

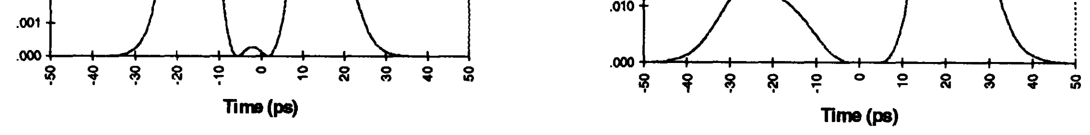

Figure 3.8a and 3.8b

Enlarged View of Switched Output Pulses, Pulse A (a) and Pulse B (b)

As with the simplified model, it is useful to investigate the effects of timing jitter on the switching efficiency. Due to the asymmetry of the nonlinear interaction, one must now consider the switching ratios for both input pulses. Figures 3.10a,b are plots of the pulse width normalized timing jitter to switching ratio, $R = E_{out}/E_{in} = 1 - \zeta$. Note that both inputs are biased ON and being switched OFF, so small R means high switching efficiency.

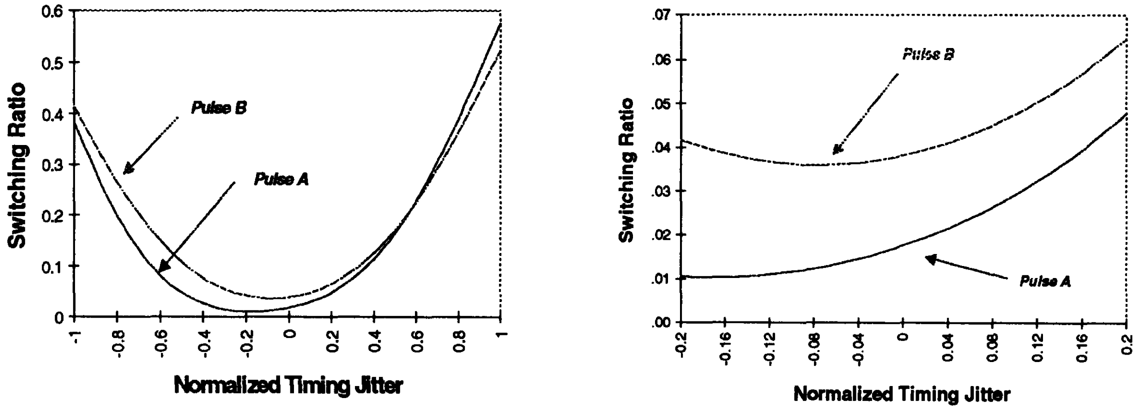

Figure 3.9a and 3.9b

Effects of Timing Jitter on Switching Ratio

As can be seen from Figures 3.9a and 3.9b, a timing jitter of half a pulse width = 12.5 ps degrades the switching efficiency to 95%. As stated earlier, timing jitter in real systems is expected to be considerably less than half a pulse width. As a comparison to the degenerate wavelength case, the pulse-walk-through device is less sensitive to timing jitter as evidenced by the smaller curvature of the timing jitter curves around the optimal timing point. More importantly, however, is the fact that the walk-through switching scheme is less prone to adverse pulse shaping effects than the no-walk-through scheme.

3.1.3 Soliton Switching

As the bit rate requirements of optical processing devices increase, the requisite pulse widths must decrease commensurately. As the pulse widths approach picosecond or sub picosecond time scales, dispersion becomes a major obstacle in devices with long interaction lengths. Moreover, peak pulse powers become high enough that soliton effects must be considered in the anomalous dispersion regime. Soliton based switching has the advantage that the problem of pulse broadening is greatly ameliorated and consequently, higher rate switching may be achieved. Thus, in the next section, I consider a different model for the high bit rate regime.

We assume that the inputs to the nonlinear material are unchirped fundamental solitons at different wavelengths. The wavelengths are chosen to optimize the phase modulation and power requirements via pulse walk through. Fiber loss is included via soliton broadening. The analytical theory for the soliton switching case is very similar to that of the general case presented in the last section. The only differences are the input pulse shapes and the pulse width evolution equations. The space dependent intensity pulse shapes are:

$$\begin{aligned} I_s(x) &= I_{s0}\mathrm{sech}^2\left(\frac{x-x_{s0}(t)}{\Gamma_s(t)}\right)e^{-\alpha x} \\ I_c(x) &= I_{c0}\mathrm{sech}^2\left(\frac{x-x_{c0}(t)}{\Gamma_c(t)}\right)e^{-\alpha x} \end{aligned} \tag{3.21}$$

The exact pulse width evolution is, in general, complicated due to the fact that the NLSE with loss is not integrable. However, an accurate analytical functional form has been derived for the r.m.s pulse width evolution assuming an initial fundamental soliton[46]:

$$\sigma_T^2 \cong \sigma_T^2(0) + \frac{1}{3}x^2 - \frac{1}{3\eta}x + \frac{1}{6\eta^2}(1-e^{-2\eta x}) \tag{3.22}$$

where the r.m.s. pulse width and the FWHM for a solitonic pulse are related via:

$$FWHM = \frac{4\sqrt{3}\ln(1+\sqrt{2})}{\pi}\sqrt{\sigma_T^2} \tag{3.23}$$

x is a normalized distance related to the actual propagation distance, z, via the relation, $x = \frac{\tau^2}{|\beta_2|} z$, where $\tau = \frac{\eta}{v}$ and η is the mode loss coefficient. For the device regime of interest, $\frac{\tau^2}{|\beta_2|} \sim 1$, and the loss is assumed to be .25 dB/km. These numbers give rise to $\eta \sim 0.0433$. Figure 3.10 is a plot of the square root of the r.m.s. pulse width. Note that for large distances, the pulse width increases linearly since the pulse peak power is not sufficient to maintain a fundamental soliton. Consequently, as expected, it is equivalent to linear propagation for long distances.

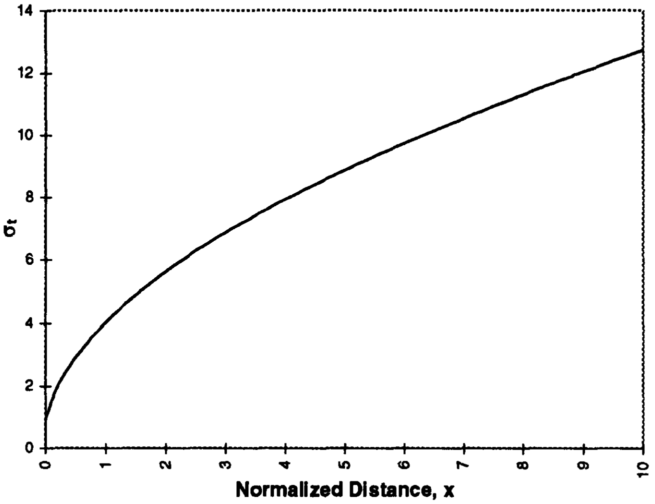

Figure 3.10: σ_t *vs. Normalized Distance for Lossy Soliton Propagation*

3.2 Theoretical Analysis of Semiconductor Switches

3.2.1 Refractive Index and Gain Nonlinearities

As discussed in Chapter 2, in general, the relevant optical nonlinearities in semiconductor have many contributions with time constants varying from 100's of femtoseconds to milliseconds. For the purposes of analyzing the first order switching characteristics of the single arm interferometer utilizing a semiconductor nonlinearity, it is sufficient to assume that the gain and index nonlinear responses can be written as a convolution of the intense incident control field with an impulse response composed of a weighted sum of exponentials characterizing the recovery of the associated nonlinearity[47]. The latter is simply a consequence of nonlinear dispersion (non-instantaneous nonlinear response) as shown in Eq. 2.13. Thus, the nonlinear phase change, for example, can be written as:

$$\Delta\phi_{NL}(t) = \frac{2\pi}{\lambda_c} n_2 L\left(I_c \otimes h(t)\right) = \frac{2\pi}{\lambda_c} n_2 L \int_{-\infty}^{t} I_c(t')\sum_{i=1}^{n} a_i e^{-\left(\frac{t-t'}{\tau_i}\right)} dt' \qquad (3.24)$$

where $I_c(t)$ is the control pulse shape, a_i are the weighting coefficients for the i^{th} nonlinear contribution, and τ_i are the relaxation time constants for the i^{th} nonlinear contribution. In addition to the phase modulation which is due to a change in the real part of the material index, gain modulation due to a change in the imaginary part of the index is also present. As such, an expression similar to Eq. 3.24 may be written for gain modulation.

The sign of the gain and index changes depends on the degree of inversion of the semiconductor material. Previous studies have shown that in the absorption regime (no inverted population), the transient and long lived index changes are negative leading to a negative nonlinear phase change[48]. Alternatively, in the gain regime where a population inversion exists, the transient and long lived index change is positive leading to a phase advancement. At transparency, no long lived phase change is observed. These results may be explained via a simple plasma model of the semiconductor material in which the carriers are treated as non-interacting particles[49]. The index for such a material can be related to the plasma frequency, $\omega_p^2 = \frac{Nq^2}{\varepsilon_0 m}$, via the relation, $n^2 = 1 - \frac{\omega_p^2}{\omega^2}$, where N is the carrier density, q is the electronic charge, ε_0 is the free space permittivity, and m is the particle mass. Thus, an increase in the carrier density leads to an increase in the plasma frequency which results in a decreased refractive index. In the absorption regime, absorption of the control leads to an increase in the carrier density and a decrease in the index. In the gain regime, stimulated emission leads to a decrease of the carrier density and an increase in the index. At transparency, there is no long-lived carrier density change and thus no long-lived index change.

In the case of the gain, for the pulse widths of interest (1 - 10 ps), the transient effect is a reduction in gain in all three regimes. The long-lived gain change, however, does depend on the degree of population inversion. More specifically, in the absorption regime, a long-lived increase in gain is observed due effectively to pumping of the material by the control pulse. Alternatively, in the gain regime, a long-lived gain reduction is observed due to stimulated emission. In our experiment, we used a semiconductor laser amplifier (SLA) biased above threshold, and thus we were operating in the gain regime. Consequently, we expect a transient and long-lived reduction in gain, in addition to an increase in index.

3.2.2 Switching Analysis, Co-propagating Control Case

The first case I will analyze is the co-propagating signal and control case, applicable to the UNI geometry. As before, we begin with Gaussian incident pulse shapes. An analogous analysis can be carried out using solitons. In fact, in a scenario in which pulses at the end of a long haul high speed point-to-point link are to be demultiplexed, the soliton assumption is more realistic. However, since we are interested in the case of a semiconductor nonlinearity with an interaction length short in comparison to the pulse widths, the exact pulse shape is of little consequence since pulse distortion due to waveguide nonlinearities or dispersion is insignificant. Moreover, analytic results are obtainable with the Gaussian assumption.

$$I_s(t) = I_{s0} e^{-(\frac{t}{\tau_s})^2}$$
$$I_c(t) = I_{c0} e^{-(\frac{t+T}{\tau_c})^2} \qquad (3.25)$$

Since the interaction length is small (i.e. ~ 1mm), the effect of group velocity dispersion in the nonlinear medium is small. A such, the signal and control pulses can be assumed to propagate at the same velocity and without pulse distortion through the nonlinear medium. Consequently, the analysis is similar to the no-walk-through case with fiber nonlinearity as presented in Chapter 3.1.1. Thus, the induced phase modulation profile on the signal pulse is simply proportional to the temporal index change profile.

We now assume that the nonlinear response is composed primarily of 2 contributions. The first is essentially instantaneous, and reacts on time scales on the order of τ_1 = 500 to 1000 fs. This contribution is the slowest of the sub-picosecond nonlinearities and most likely is due to carrier heating[50]. The second is a slow response reacting on time scales on the order of τ_2 ~ 1 ns[51]. This slow response is due to the relaxation of the carriers from the upper energy level manifold by spontaneous emission. However, it has been found that upper state lifetimes can be considerably reduced in the high carrier density regime due to a number of effects including non-radiative, or so called Auger, recombination which is critically dependent on carrier density[52]. As such, gain recovery has been observed with time constants of τ_2 ~100 ps[53]. Given that we are operating the SLA in the high gain regime, it is reasonable to assume that τ_2 is some hundred picoseconds. Thus, we can write an impulse response, h(t), for the nonlinearity:

$$h(t) = a_1 e^{-\frac{t}{\tau_1}} + a_2 e^{-\frac{t}{\tau_2}} \qquad (3.26)$$

Figure 3.11 shows a typical impulse response for a_1=1, a_2=0.1, τ_1=0.6 ps, τ_2 = 100 ps.

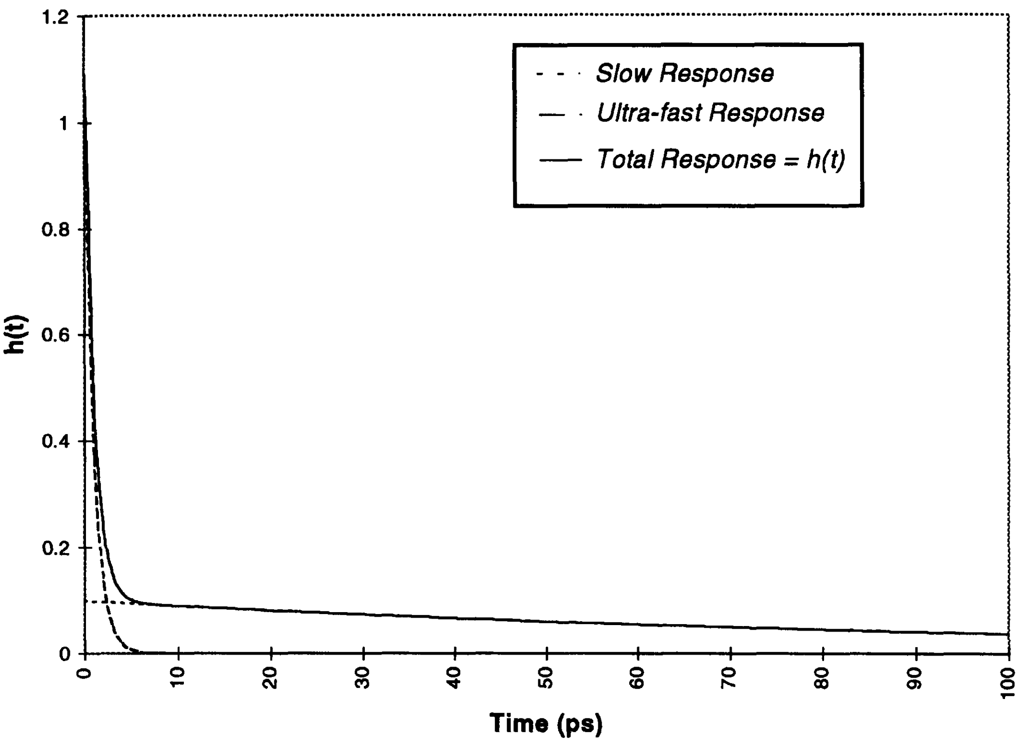

Figure 3.11: ***SLA Impulse Response***

Given h(t), one can simulate the effect of an incident pulse stream on the instantaneous gain of the SLA by convolving the pulse stream with the impulse response. Figure 3.12 shows the simulation results of such a convolution for a 40 Gb/s random control bit stream composed of 8 ps Gaussian pulses. Note that the gain compression is pattern dependent due to the long lived recovery. The latter has a direct impact on device performance since the gain that a probe pulse experiences is dependent on the history of the control stream. If, however, the control stream bit period is 100 ps or more, the pattern dependent gain is negligible. Such is likely the case in demultiplexing operation where a high speed data stream is gated by a lower rate (for example 10 Gb/s) control stream.

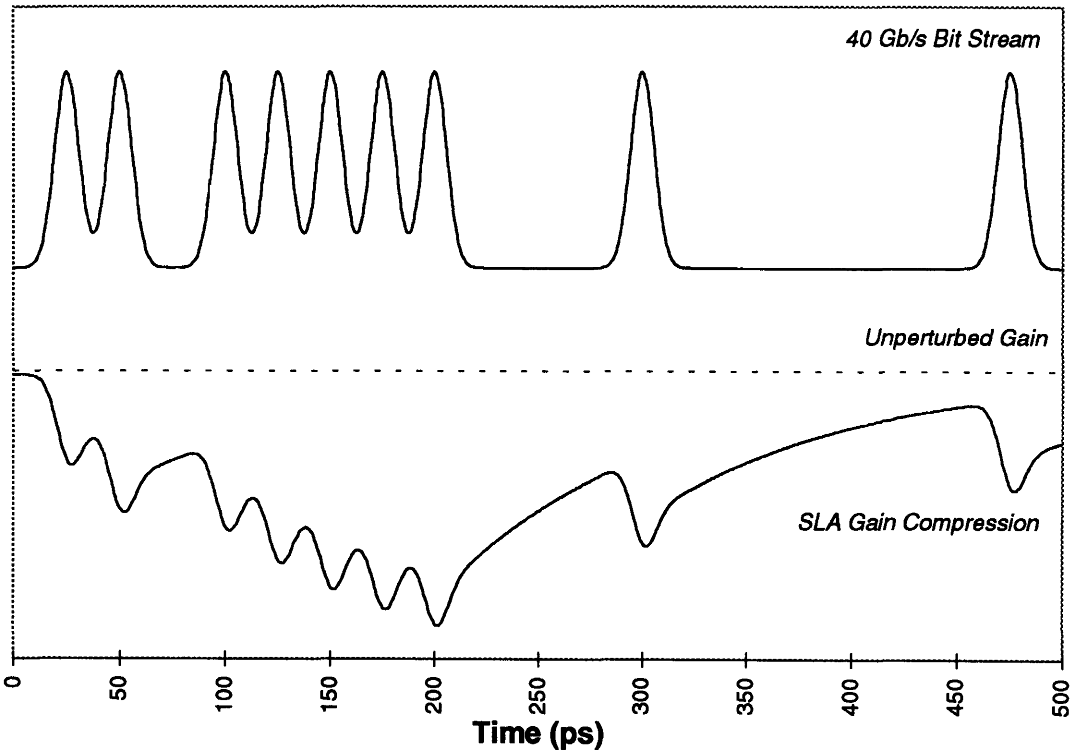

Figure 3.12: ***Simulated Gain Compression due to a High Speed Control Stream***

It should be noted that the gain compression can be harmful or beneficial, depending on the intended device function. For demultiplexing (i.e. AND gating) where the UNI is biased OFF and is turned ON only in the presence of the control, the gain compression reduces the output intensity of the demultiplexed stream and thus opposes the fast index nonlinearity. However, in an inverting scenario, the gain compression and index nonlinearity both help to turn the signal pulse OFF. As a result, good 0:1 contrast ratios can be obtained. Indeed, as will be shown in Chapter 5, the performance of the UNI in a high speed inverter configuration using a semiconductor nonlinearity is better than a UNI using a fiber nonlinearity. In this way, the optimal 78% switching efficiency derived in section 3.1.1 can be overcome. To summarize the gain effects, the long-lived gain recovery leads to an overall decrease in the output signal pulse amplitude since both orthogonal polarization components experience the same long-lived gain. The fast gain compression is equivalent to a transient change in the interferometer bias since it causes a differential gain change between orthogonal polarization components, which when interferometrically recombined, results in a transient output intensity offset.

As with the gain modulation, the induced index change is pattern dependent due to a similar long lived effect. The temporal phase change induced by a single control pulse can be obtained by convolving the Gaussian control pulse with the impulse response. Substituting Eq. 3.26 and Eq. 3.25 into Eq. 3.24 gives the induced phase modulation profile as a function of time. The result is a sum of error functions weighted by appropriate exponentials. As τ_1 and τ_2 approach 0, the induced phase change follows the pulse shape, as expected. This limit is, in fact, the case analyzed for the fiber nonlinearity in section 3.1.1.

$$
\begin{aligned}
\Delta\phi_{NL}(t) &= \frac{2\pi}{\lambda_c} n_2 I_{c0} L \int_{-\infty}^{t} e^{-\left(\frac{t'}{\tau_c}\right)^2} \left\{ a_1 e^{-\left(\frac{t-t'}{\tau_1}\right)} + a_2 e^{-\left(\frac{t-t'}{\tau_2}\right)} \right\} dt' \\
&= \frac{2\pi}{\lambda_c} n_2 I_{c0} L \tau_c \left[a_1 e^{\frac{1}{4}\left(\frac{\tau_c}{\tau_1}\right)^2} e^{-\frac{t}{\tau_1}} * erf\left(\frac{t}{\tau_c} - \frac{1}{2}\frac{\tau_c}{\tau_1} \right) \right. \\
&\qquad \left. + \; a_2 e^{\frac{1}{4}\left(\frac{\tau_c}{\tau_2}\right)^2} e^{-\frac{t}{\tau_2}} * erf\left(\frac{t}{\tau_c} - \frac{1}{2}\frac{\tau_c}{\tau_2} \right) \right]
\end{aligned}
\tag{3.27}
$$

As stated before, an analogous expression for the gain modulation can be written. Note that since we are in the gain regime of the SLA (biased above threshold), the sign of the index change is positive. Moreover, as the magnitude of the long-lived index change increases, the phase profile becomes increasingly asymmetric due to the slowly decaying tail. This tail may provide an increase in the obtainable switching efficiency if the signal to control pulse temporal offset is chosen such that the majority of the signal pulse sees the relatively uniform tail of the induced index change. As such, the switched output pulse shape would not be distorted as much. Unfortunately, however, long-lived gain compression accompanies the long-lived index change, and thus would probably counter the increase in 0:1 contrast. The complex electric field at the output of the interferometer is: $E_{out}(t)=\frac{1}{2}A(t)g(t-\frac{T}{2})e^{-j\omega t}+\frac{1}{2}A(t)g(t)e^{-j\omega t}e^{j\phi(t)}$, where A(t) is the slowly varying envelope of the input electric field of the signal pulse, T is the bit period, $g(t)$ is the gain compression term due to pump induced cross gain saturation, and $\phi(t)=\phi_b+\Delta\phi_{NL}(t)$. Calculating the squared magnitude of this field yields the output intensity profile:

$$I_{out}(t)=I_s(t)g(t)g(t-\tfrac{T}{2})\cos^2\left(\frac{\phi_b+\Delta\phi_{NL}(t)}{2}\right)+\frac{1}{4}I_s(t)\left[g(t)-g(t-\tfrac{T}{2})\right]^2 \qquad (3.28)$$

Finally, the switching efficiency is obtained by integrating $I_{out}(t)$ over all time and dividing by the input pulse energy. Note that the last term represents an interferometer bias offset.

As with the pattern dependent gain compression shown in Figure 3.12, we have run simulations comparing the effects of long-lived refractive index nonlinearities on balanced and unbalanced geometries. A typical unbalanced geometry is the Mach Zehnder interferometer, while the SAI-based devices presented in this thesis are examples of balanced devices. Figure 3.13 shows the results. The impulse response parameters are $a_1=1$, $a_2=0.025$, $\tau_1=0.6$ ps, $\tau_2 = 100$ ps. We generate pseudo-random signal and control bit streams at 40 Gb/s employing 4 ps pulses (the top two traces). The simulated induced index change is shown in the third plot where we have set the experimental parameters such that the peak index change of the first pulse corresponds to an induced π phase shift on the signal. This corresponds to picking a control power that induces a π phase shift on an isolated signal pulse. Plots 4 and 5 are the simulated output streams for an unbalanced and a balanced geometry respectively. Plot 5 was generated by calculating the phase difference between temporally corresponding points on the orthogonal signal polarization components separated by 12.5 ps, as would be the situation in an SAI based device. Lastly, the device is biased OFF, so we expect AND operation (an output pulse only in the presence of both a signal and a control pulse). The output pulses are numbered from 1 to 11 for reference.

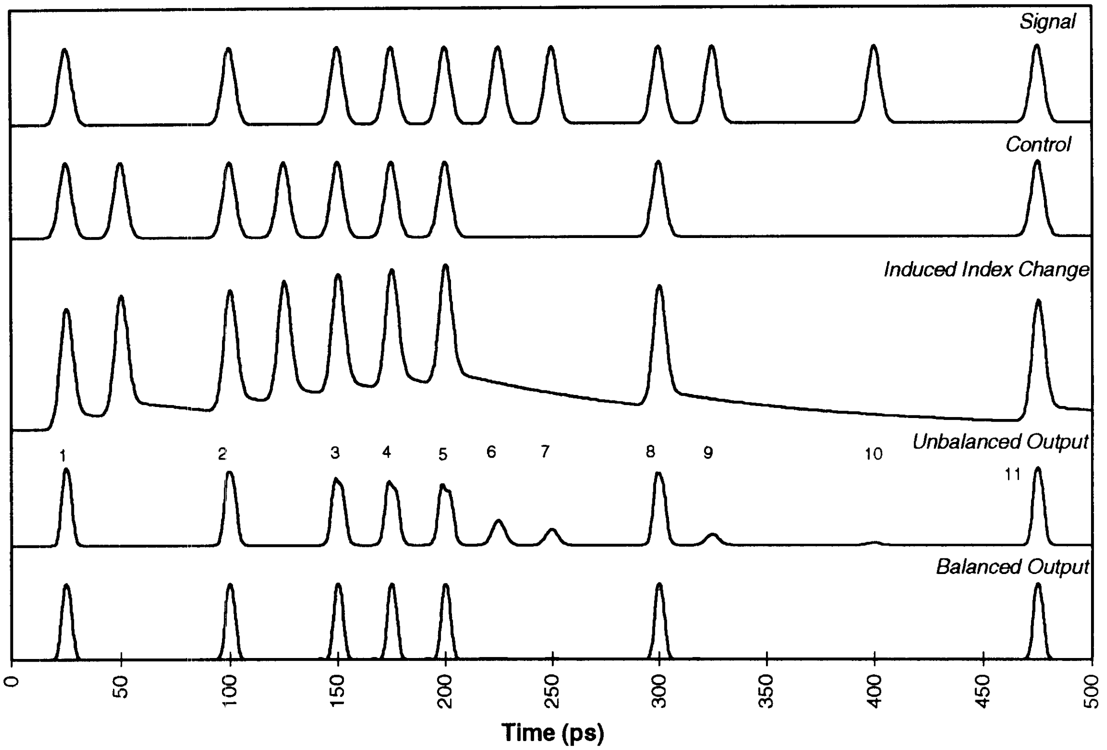

Figure 3.13: *Simulated Effects of Long Lived Refractive Index Nonlinearities*

Note that in Plot 4, a pattern dependent output is observed. More specifically, the long lived index response leads to the presence of pulses outside the window of the control pulses (output pulses 6,7,9,10). Moreover, peak phase shifts greater than π lead to output pulse distortion as observed in output pulses 3,4,5. All these effects will lead to a degradation in the bit error rate of the device as compared to a balanced geometry, as shown in Plot 5. Two assumptions in the above simulation need to be pointed out. The primary, and most obvious one is that gain compression was ignored in Figure 3.13 so that the effects of long lived-index nonlinearities and long-lived gain nonlinearities could be separated. Secondly, I ignored saturation of the nonlinearities. Namely, long run lengths of 1's in the control stream will eventually saturate both the index and gain nonlinearities at which point, the induced index and gain modulation, averaged over a bit period, would reach steady state. The latter effect may be modeled phenomenologically by multiplying the induced modulations by an average power dependent term that acts to saturate the nonlinearity.

Finally, we performed a simulation, shown in Figure 3.14, that included the effects of both refractive index and gain nonlinearities using Eq. 3.28. We chose the parameters such that the index and gain changes were related as follows: an induced phase shift of π corresponds to a 50% reduction in gain. With the knowledge of the operating carrier densities, this relationship may be translated into the more familiar linewidth enhancement factor. The notable feature of Figure 3.17, as expected, is the pattern dependent output pulse intensities.

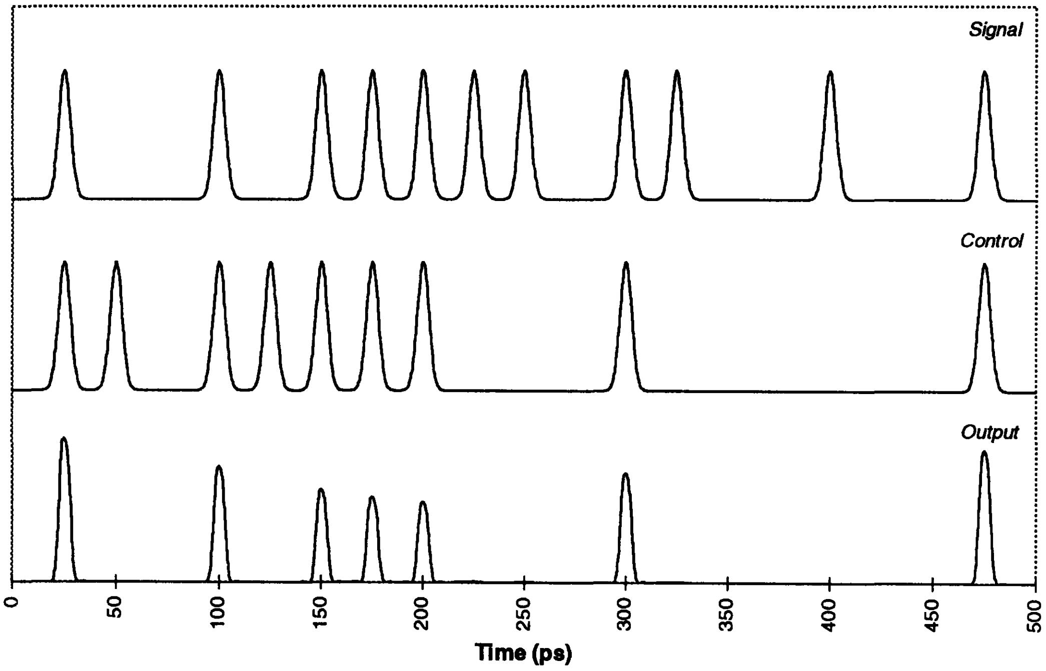

Figure 3.14: ***40 Gb/s UNI AND Gate Simulation***

It should be noted that to accurately estimate the time constants and weighting coefficients for the fast and slow gain nonlinearities, gain and index pump probe measurements should be conducted in the operating regime of interest. In fact, the single arm interferometer geometry was first conceived of and used by K. K. Anderson, et. al, to investigate band edge ultra-fast index nonlinearities in AlGaAs waveguides[54]. Additional work, however, needs to be done as concerns the effects of the long lived gain and index nonlinearities on device performance. Although the SAI geometry is relatively immune to long lived phase changes, it certainly is effected by long lived gain changes which directly translate to pattern dependent output pulse intensity fluctuations. For this reason, it is desirable to be operating in a regime in which the magnitude of the long lived gain nonlinearities are small in comparison to index nonlinearities. The latter may be accomplished by using a below-band pump so that long-lived pump induced carrier density changes are small. An investigation of the wavelength dependence of gain and index nonlinearities in the SLA and their relation to device performance will be the subject of future work.

3.2.3 Switching Analysis, Counter-propagating Control Case

We can now analyze the last scenario of interest. Namely, that of the counter-propagating control in the SLA. For mathematical simplicity, we assume that the long lived index change is small in comparison to the ultra-fast response so that the induced phase shift essentially follows the control pulse shape. Consequently, the analysis of the phase profile reduces to the interaction of 2 counter-propagating pulses. We begin with the space - time pulse shapes for signal and control:

$$\begin{aligned} I_s(x) &= I_{s0} e^{-\left(\frac{x-x_{s0}(t)}{\Gamma_s}\right)^2} e^{-\alpha x} \\ I_c(x) &= I_{c0} e^{-\left(\frac{x-x_{c0}(t)}{\Gamma_c}\right)^2} e^{-\alpha(L-x)} \qquad 0 \le x \le L \end{aligned} \tag{3.29}$$

where α is the intensity loss coefficient, assumed to be the same for both the signal and control and L is the device length (~ 1 mm). The pulse widths are taken to be constant over the length of interaction since the effects of GVD are small for the 1-10 ps pulsewidths of interest. The time dependent pulse centers evolve according to:

$$\begin{aligned} x_{s0}(t) &= x_{s0}(t_0) + vt \\ x_{c0}(t) &= x_{c0}(t_0) - vt \end{aligned} \tag{3.30}$$

The group velocities, v, for each pulse are of the same magnitude but opposite sign. The control induced index change follows the control pulse shape because pulse distortion due to GVD and gain dynamics is ignored. As in section 3.2.2, we then move into the signal reference frame via the substitution, $x = x_{s0}(t)+x_s$ to yield the index change seen by the signal:

$$\Delta n(t,x_s) = n_2 I_{c0} e^{-\left(\frac{-\Delta x_0+2vt+x_s}{\Gamma_c}\right)^2} e^{-\alpha(L-x_{s0}(t_0)-vt-x_s)} \tag{3.31}$$

where $\Delta x_0 = x_{c0}(t_0) - x_{s0}(t_0)$. We now integrate over the interaction time to obtain the phase profile:

$$\begin{aligned}\Delta\phi(x_s,\Delta x_0) &= \frac{2\pi}{\lambda_s} v_s \int_{t_0}^{t_0+L/v_s} \Delta n(t,x_s)dt \\ &\propto e^{\frac{1}{2}\alpha x_s}\left\{erf\left[\frac{x_s}{\Gamma_c}-\frac{1}{4}\alpha\Gamma_c+\frac{L}{\Gamma_c}\right]-erf\left[\frac{x_s}{\Gamma_c}-\frac{1}{4}\alpha\Gamma_c-\frac{L}{\Gamma_c}\right]\right\}\end{aligned} \tag{3.32}$$

Finally, one can transform Eq. 3.32 into the pulse time frame via the substitutions $x_s = vt_s$ and $\Gamma_c = v\tau_c$. This result is very similar to that obtained in section 3.2.2 except that asymmetry due to GVD is not present. Since the pulse widths are larger than the device length by a factor of 2 or 3, the phase profile has essentially the same width as the control pulse. As both the signal and control pulse widths decrease, the phase profile becomes flatter due to the larger pulse width normalized interaction length. It is important to note that the only reason why a counter-propagating configuration yields sufficient phase shift for switching is that the nonlinear index for semiconductor is typically 4 orders of magnitude larger than that of fiber. Clearly, a counter-propagating interaction in fiber would yield essentially no switching potential.

From these results, it is apparent that the co and counter-propagating scenarios yield very similar switching characteristics if the interaction length of the semiconductor is comparable to the pulse widths in the spatial domain. Thus, we can gain device functionality, namely cascadability, and a complexity reduction since a filter is not required, with no incurred penalty in switching performance. In the case that the pulses are shorter than the device nonlinear medium, the expected switching performance decreases because one control pulse begins to interact with more than one signal pulse. As a result, the switching window becomes larger than the signal pulse window resulting in incorrect device operation. One may therefore decrease the semiconductor interaction length at the obvious sacrifice of decreasing the obtainable phase shifts for similar peak powers.

In conclusion, we have presented a theoretical analysis of various switching devices based on the SAI geometry. Namely, 2 models of the nonlinear interaction in fiber were analyzed to investigate the performance of fiber based demultiplexing and XOR gating respectively. A very basic model of the nonlinear interaction in semiconductor was outlined. Considerable simplification was justified by the fact that most of the ultra-fast nonlinearities in semiconductor do not have considerable effect on the index modulation by 10 picosecond pulses. It was shown that the co-propagating and counter-propagating schemes yield similar induced phase profiles for pulse widths comparable to the nonlinear interaction length.

Chapter 4: Experimental Setup and Results

4.1 Description of Experiment

4.1.1 Data Rates

To experimentally demonstrate optical switching based on the single arm interferometer geometry, we chose a bit rate that is not only sufficiently high to show viability at optical transmission throughputs, but also sufficiently low such that moderate device characterization is still possible. In the case of demultiplexing, a high rate optical stream is sampled at a lower rate called the frame rate. We chose 10 Gb/s for the frame rate because sufficient electronics around 10 GHz exists in our lab. Namely, RF drives for mode-locking and electro-optic modulation, photodetectors and digital sampling scopes with bandwidths up to 50 GHz, and a bit error rate tester (BERT) capable of rates up to 12.5 GHz. To obtain higher rate optical streams, passive multiplexing of the 10 Gb/s data was used. For the initial demonstration of the devices, we decided that an aggregate optical data rate of 40 Gb/s was feasible for demultiplexer and inverter operation using the UNI while 20 Gb/s was feasible for logic functions using the SADINI. The reason for these numbers concerns the obtainable pulsewidths from the mode-locked lasers and the requirements on orthogonally polarized pulse overlap in the nonlinear medium, as will be described in the next section.

First we consider the pulse width constraints for the UNI. A 40 Gb/s data rate corresponds to a 25 ps bit interval. Because the signal pulse is split into delayed orthogonal polarizations, the temporal extent of the pulses must not exceed half the bit period (12.5 ps). It is important to remember here that I am not talking about the FWHM, but rather the full support of the pulse. The latter point is critical because slightly overlapping orthogonal signal components will cause deleterious cross phase modulation, resulting in the inability to fully cancel the signal pulse.

The reason why we expect the SADINI to operate well at bit rates lower that the UNI for the same input pulse widths is that 4 pulses (2 orthogonally polarized components for both the signal and the control) must now fit in the bit period, as shown in Figure 4. Figure 4.1a shows the desired case where orthogonal polarizations from the same input do not overlap and thus, a good output extinction ratio is expected. Figure 4.1b depicts a scenario in which the pulse overlap criterion is not met. Figure 4.1c shows the demultiplexer setup in which no signal / control pulse walk-through is desired. Figure 4.1d shows the XOR case in which the two interacting signal and control pulses are initially temporally separated to allow pulse-walk through and its consequent effect on output extinction ratio. Note however, that in this last case, full pulse walk-through cannot be achieved since pulse P1 will start to interact via cross phase modulation with pulse P3 and pule P2 will begin to interact with pulse P4. The latter would, in fact, decrease the magnitude of the differential phase shift profiles. This last problem can be fixed by further reducing the input pulse widths while maintaining the same bit period as shown in Figure 4.1e.

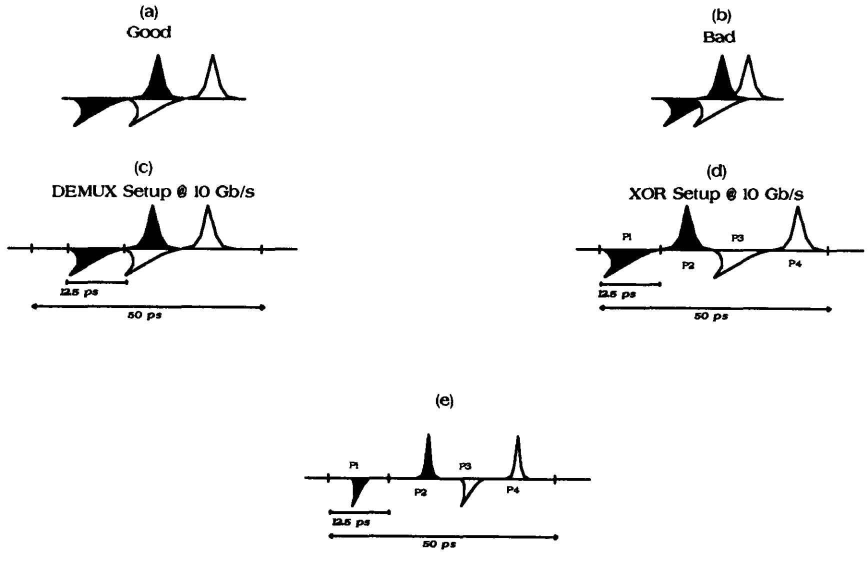

Figure 4.1: ***Pulse Overlap Requirements***

4.1.2 Sources

Two options for pulse sources were considered, the first being gain-switched distributed feedback (DFB) semiconductor lasers. The advantages of these sources are their compact packages and reliability. The most immediate problem, however, was the output pulse widths. Via direct RF modulation at 5 and 10 GHz, typical pulse FWHM exceeded 30 ps. Consequently, a linear pulse compression scheme was considered. Gain switched pulses are typically chirped due to dynamic refractive index changes in the gain medium brought about by carrier density and gain modulation due to the direct RF drive. Although the chirp profile is nonlinear, a significant central portion of the pulse is approximately linearly chirped. Thus, chirped pulse propagation through fiber with large dispersion can counteract the initial chirp and compress the pulse. From the spectrum and autocorrelation of the pulse, the time bandwidth product was computed for the available DFB sources, and a typical linear chirp parameter was estimated. The Gaussian pulse propagation results from Chapter 2 were then used to estimate the length of dispersion compensating fiber required to optimally compress the pulses. Approximately 400 m of DCF was used to compress the gain switched pulses, the results of which are shown in Figure 4.2. The uncompressed and compressed pulse widths were 25 ps and 8 ps respectively.

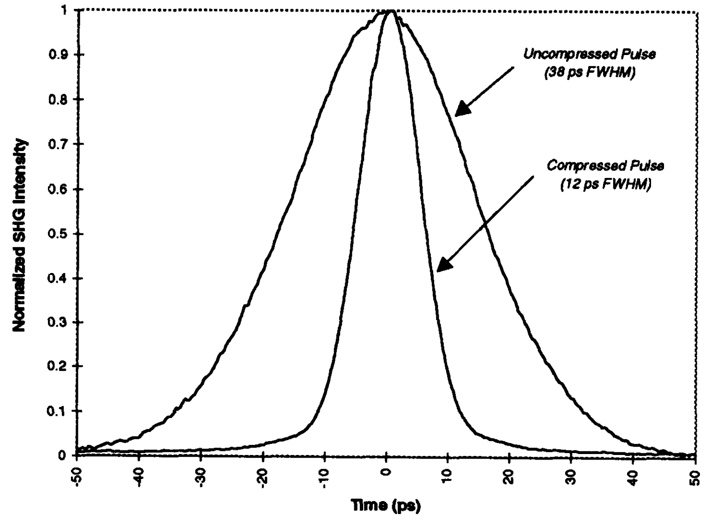

Figure 4.2: ***Autocorrelation Traces of Uncompressed and Compressed Gain Switched Pulses***

Although the compressed gain-switched pulse-widths satisfy the orthogonal polarization pulse overlap criterion, it was found that in demultiplexing operation, the timing jitter of these pulses led to a very noisy demultiplexed stream. The reason is that timing or phase jitter from the DFB pulses leads to phase modulation jitter in the nonlinear material which then causes amplitude and timing jitter in the interfered output stream. The ultimate consequence of using these sources is closing of the eye and a degradation in the achievable bit error rate. Moreover, for XOR operation in which wavelength tunability is required, DFB lasers clearly are not the ideal source.

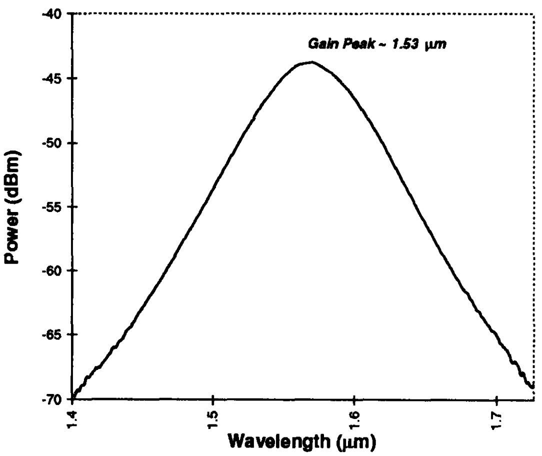

Figure 4.3: ***SLA Gain Band***

The second source considered was an external cavity mode-locked semiconductor laser. The gain medium is a semiconductor laser amplifier (SLA) with a gain spectrum shown in Figure 4.3. The laser cavity is formed between one facet of the SLA and a grating that allows wavelength tunability over the SLA gain band, as shown in Figure 4.4. The interior facet of the SLA is coated with an antireflection (AR) coating to stop lasing within the SLA. The SLA is driven with an RF signal at the desired repetition rate and is biased with a DC current. Coupling in and out of the SLA waveguide is achieved through lenses. Lastly, the laser output is coupled into fiber. Typical mode-locked pulse widths are sub 10 ps. Autocorrelation traces of the 2 sources used in the experiment are shown in Figure 4.5. The signal and control source deconvolved pulse widths were 8.3 and 6.5 ps respectively. Due to the narrow laser linewidth, at least in comparison to the gain switched DFB lasers, timing / phase jitter was substantially less than that of the gain switched DFB laser.

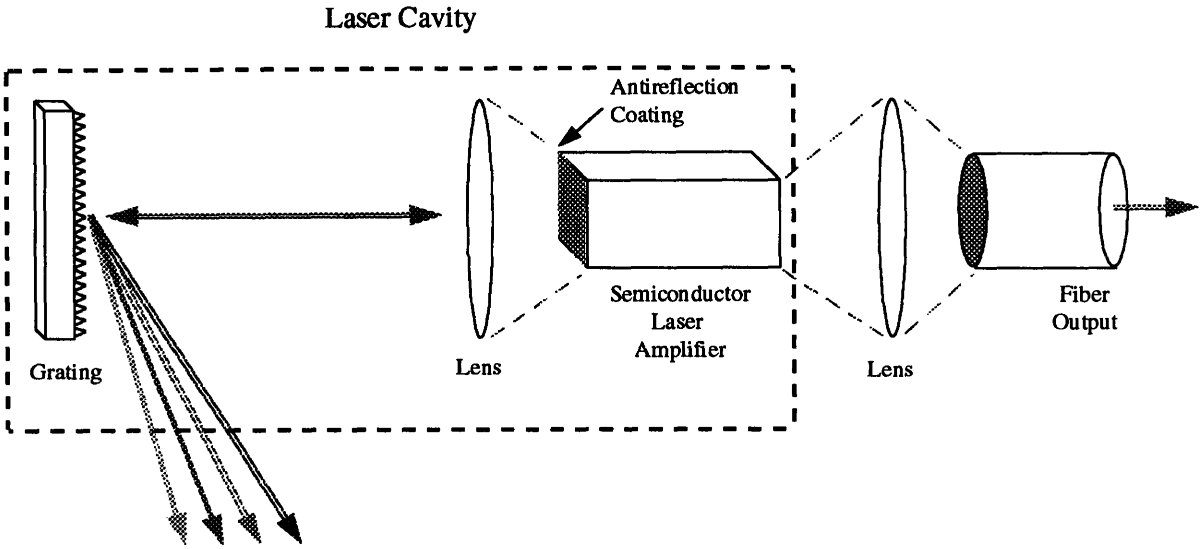

Figure 4.4: *External Cavity Mode-Locked Semiconductor Laser*

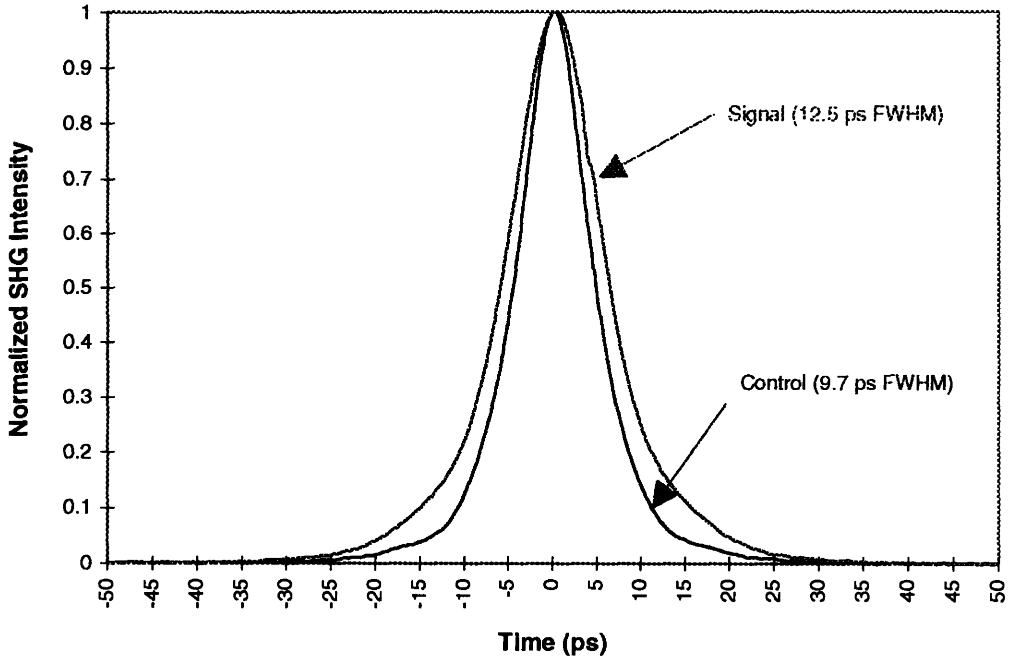

Figure 4.5: *Source Autocorrelation Traces*

In order to demonstrate a high speed bit-wise inverter using the UNI, we require a high repetition rate pulse source for use as a clock stream. Eric Swanson et. al., in our lab, have developed such a source at repetition rates over 100 GHz, based on adiabatic soliton compression of an optical beat signal[55]. Figure 4.6 shows a diagram of the 40 Gb/s Soliton Compression Source (SCS)[56]. The CW output of a DFB laser with center wavelength around 1548 nm is electro-optically modulated using a $LiNbO_3$ amplitude modulator driven by a 20 GHz RF signal. The E/O Modulator is biased at a transmission null so that the 20 GHz RF drive produces a 40 GHz amplitude modulation of the optical signal. The bias is actively stabilized using a simple feedback circuit. The 40 GHz optical sine wave is amplified in a high power EDFA and then enters the soliton compression fiber (SCF) composed of alternating sections of standard and dispersion shifted fiber designed for optimal adiabatic compression. A 10 MHz RF signal at -20 dBm is applied to the DFB laser to broaden its spectrum and thus reduce Stimulated Brillouin Scattering (SBS) in the SCF. Figure 4.7 is an autocorrelation trace of the 40 Gb/s stream showing 4 ps FWHM pulses.

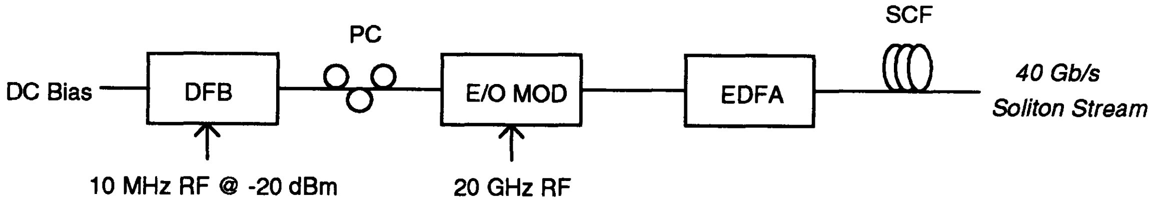

Figure 4.6: ***40 Gb/s Soliton Compression Source (SCS)***

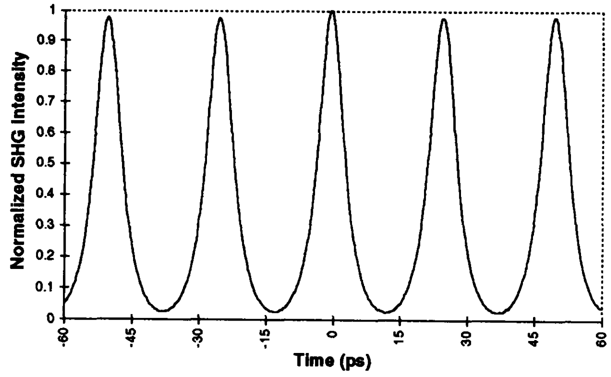

Figure 4.7: ***40 Gb/s Soliton Stream Autocorrelation Trace***

4.1.3 Passive Multiplexer / Bit Interleaver

To obtain pseudo-random high rate optical streams, the 10 Gb/s mode-locked pulses were amplitude modulated using a $LiNbO_3$ electro-optic modulator driven with a pseudo-random bit stream (PRBS) at 10 Gb/s. This 10 Gb/s PRBS was then passively multiplexed to 20 and 40 Gb/s using an optical bit interleaver as shown in Figure 4.6. It is important to point out that the passive multiplexer must be designed so that the interleaved streams are delayed with respect to each other by much larger than a bit period. The latter is required to ensure that the output stream is still a PRBS. The obvious example of a mis-designed multiplexer is where the bit interleaver delay is only half a bit period. The resulting output stream then consists of even numbered run-lengths of 1's and 0's. A diagram of the passive optical MUX is shown in Figure 4.8. Stage 1 is a 10:20 Gb/s MUX while stage 2 is the 20:40 Gb/s MUX. A fiber polarization sensitive isolator is placed at the output to ensure a single polarization output PRBS. The 3 polarization controllers (PC 's) are used to maximize the power from each arm of the MUX through the polarizer. Note that PC 3 can be set such that the output stream is a 20 Gb/s and PC 2 can additionally be set to obtain the original 10 Gb/s stream. The insertion loss of the device is approximately 6 dB.

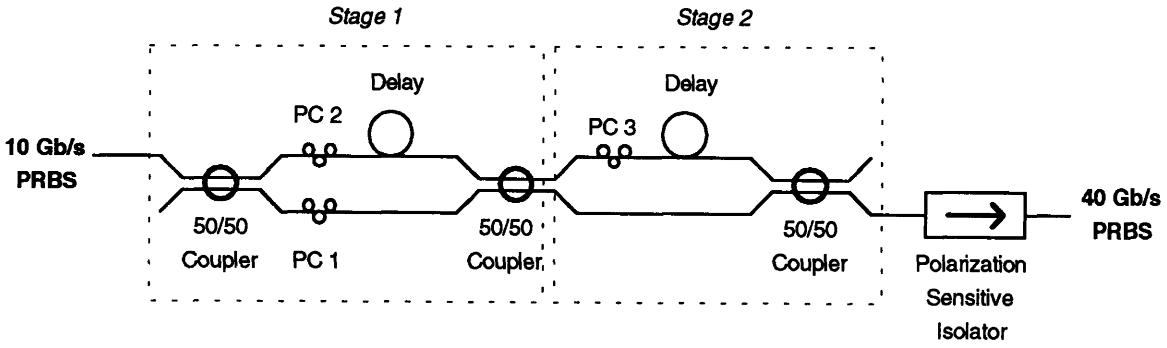

Figure 4.8: *Passive Optical Multiplexer / Bit Interleaver*

4.1.4 Optical Receiver

In order to perform bit error rate measurements at low received powers (~ -40 dBm), our optical receiver was composed of a high sensitivity erbium-doped fiber pre-amplifier (EDFA) followed by a DC to 20 GHz bandwidth photodetector. Figure 4.9 shows the EDFA design which is composed of 2 amplifying stages using counter-propagating pumps at 980 nm coupled in using wavelength division multiplexers (WDM's). Each stage uses a length of highly doped LICOM erbium fiber for amplification. Polarization Insensitive Fiber Isolators (PIFI's) are used to block leakage of the counter-propagating pump and the extra WDM port is angle cleaved at 12 degrees to prohibit back reflections of the pump. 1 nm band-pass filters (BPF's) are used at the end of each stage to filter out amplified spontaneous emission (ASE) noise outside the signal band.

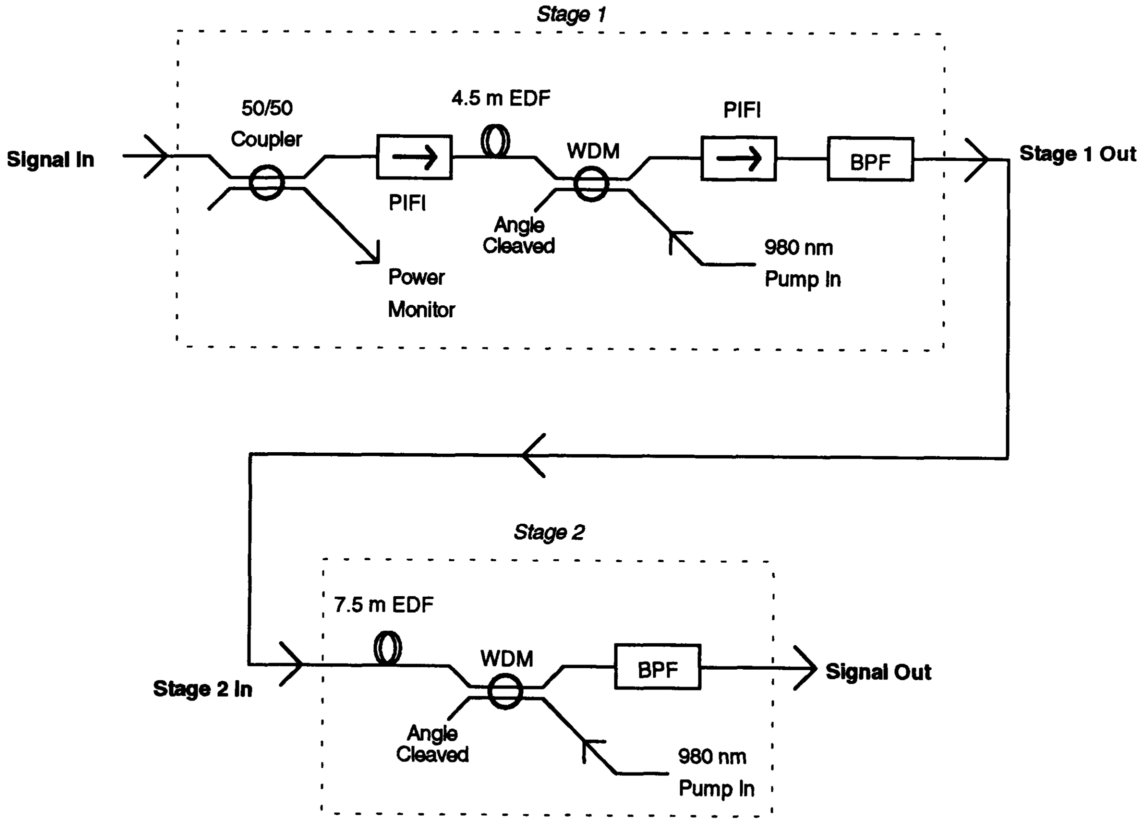

Figure 4.9: *Optical Pre-Amplifier in Receiver*

4.1.5 Device Implementations

A diagram of the UNI is shown in Figure 4.10. The PSD consists of a polarization controller (PC), birefringent fiber (BRF), polarization controller (PC) combination. The first PC is used to align the polarization state at 45° with respect to the slow and fast axes of the BRF. It was experimentally determined that the BRF had an orthogonal polarization walk-off parameter of approximately 1.6 ps/m, giving rise to the desired 12.5 ps polarization sensitive delay for a 7.5 m length of BRF. The second PC in the PSD is used for biasing the interferometer. A fiber 50/50 coupler is used to combine the control pulse with the two orthogonally polarized signal pulses. All three pulses then travel through the nonlinear medium (NLM). An additional PSD is used to recombine orthogonal polarizations. Finally, a fiber polarization sensitive isolator is used to interfere the signal components and a 3 nm band pass filter (BPF) filters out the control pulse. In the case of demultiplexing, the UNI is biased OFF, the data stream enters the signal port and the sampling stream at the frame rate enters the control port. Alternatively, for inverting operation, the UNI is biased ON, a clock stream at the desired bit rate enters the signal port while the data stream enters the control port.

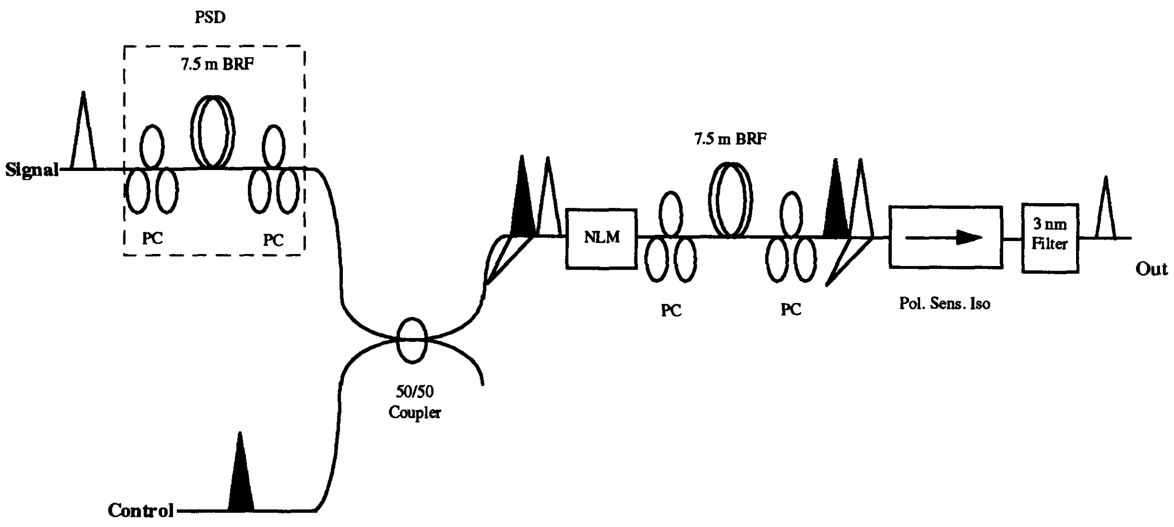

Figure 4.10: ***UNI Fiber Implementation***

The implementation of the UNI with counter-propagating control is very similar to the previous device except that the NLM is replaced by a short interaction length semiconductor (an SLA for instance) and the 50/50 coupler is placed after the NLM, as shown in Figure 4.11. Moreover, a 3 nm BPF is not required at the output. The extra port of the 50/50 coupler is angled polished at 12° to prevent back reflection of the control pulse.

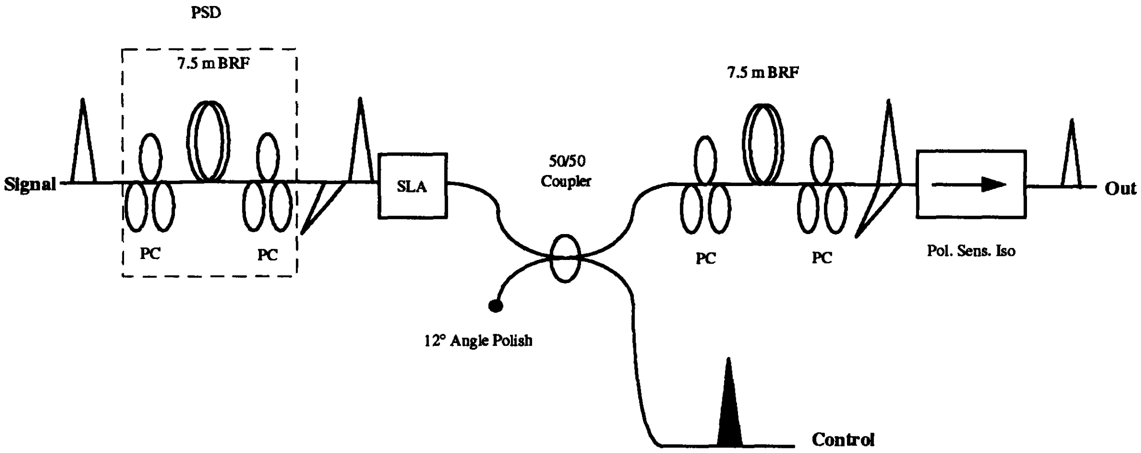

Figure 4.11: ***Fiber Implementation of UNI with Counter-Propagating Control***

An OR/ NOR gate based on the above geometry is easily implemented with the addition of a second control pulse as shown in Figure 4.12. A clock (*CLK*) stream at the bit rate serves as the signal stream while the logical inputs, *A* and *B*, serve as the control stream.

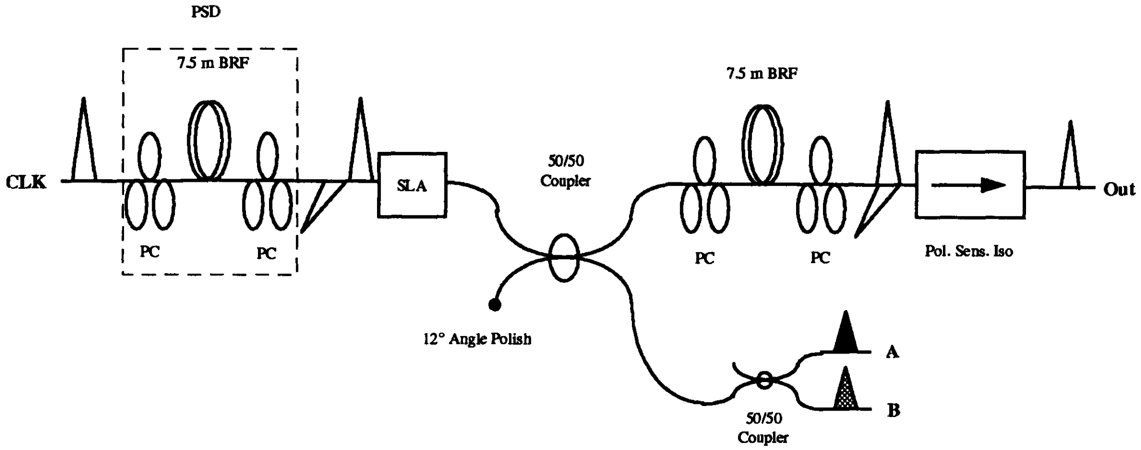

Figure 4.12: ***Fiber Implementation of an OR/ NOR Gate Based on the UNI***

Lastly, the SADINI is similar to the UNI apart from the addition of a PSD in the control arm, and the removal of the output BPF, as shown in Figure 4.13. Each arm can be biased independently to yield a particular logic function *f(A,B)*. Note that the output time slots for the signal and control differ by a pulse width, as alluded to earlier. To remedy this situation, one could insert a piece of dispersion shifted fiber after the polarizer in which the signal and control pulses could walk into the same time slot via GVD. No attempt was made in this thesis to demonstrate that capability, however.

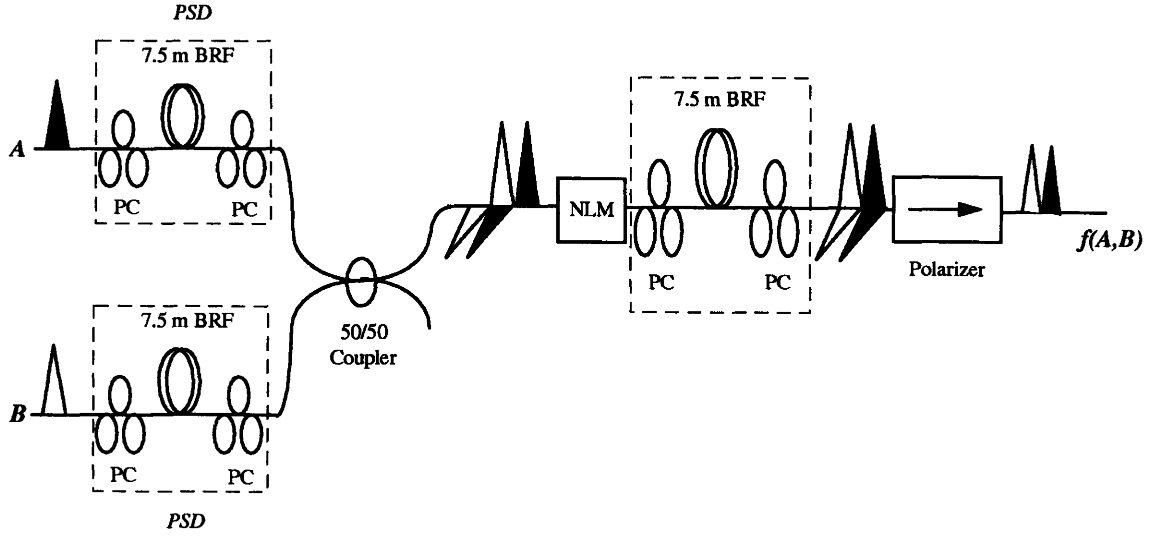

Figure 4.13: ***SADINI Fiber Implementation***

Lastly, although we found empirically that the devices just presented were stable enough to perform bit error rate measurements, we have designed a feedback circuit that can stabilize the interferometer bias in a UNI and SADINI over thermal time-scales. The details of the design can be found in section A.2.

4.2 Generic Experimental Setup

Figure 4.16 shows the generic experimental setup for the switching demonstrations. Double lines represent signals in the optical domain and single lines represent electronic signals. In the case of demultiplexing for example, a 20 or 40 Gb/s optical pseudo-random bit stream (PRBS) passively multiplexed from 10 Gb/s (as described in section 4.1.2) enters the signal port (*S*) of the switching device and a 10 Gb/s clock stream enters the control port (*C*). The demultiplexed optical stream enters a variable optical attenuator to vary the received power in order to perform BER measurements. The attenuated signal enters the receiver described in section 4.1.3 and the resulting 10 Gb/s electronic signal is fed into the BERT and a high speed sampling scope with a 50 GHz bandwidth. For inverting, XOR, OR, and NOR operation, the setup is similar except that the ports for the appropriate device are utilized differently, the details of which will be made apparent in the next sections.

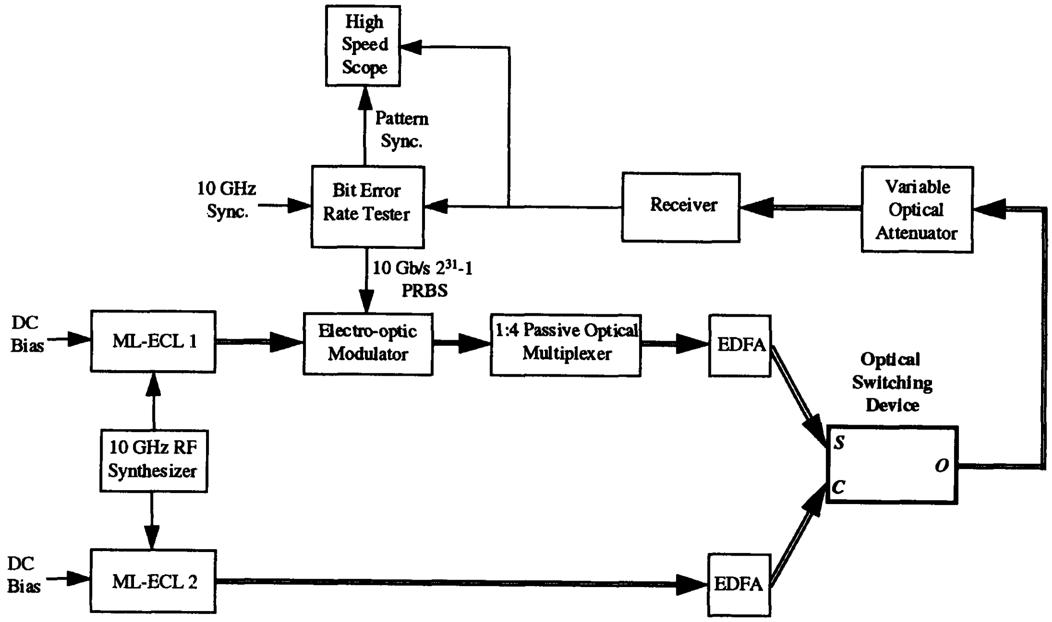

Figure 4.14: ***Generic Experimental Setup***

4.3: Switching Results using a Fiber Nonlinearity

4.3.1 UNI / DSF - Demultiplexing and Inverting

Using the experimental setup shown in Figure 4.14, we have demonstrated demultiplexing of 20 and 40 Gb/s aggregate streams using a clock stream at a frame rate of 10 Gb/s. For nonlinearity in the UNI, we used an 8.8 km length of dispersion shifted fiber (DSF) with a dispersion zero of 1547 nm. The clock (control) and data (signal) wavelengths were 1549.3 and the 1545 nm respectively. These wavelengths were chosen to straddle the dispersion zero so as to avoid pulse walk-off leading to intersymbol interference (ISI). The UNI was biased OFF and the output filter was set to pass the signal pulses. The clock and data average powers entering the DSF for 20 Gb/s demultiplexing were 26 mW and 5.2 mW respectively. Those for 40 Gb/s demultiplexing were 28 mW and 6 mW respectively. The theoretical average 10 Gb/s clock power required to induce a π peak phase shift to the signal is ~ 25 to 30 mW (depending on the exact polarization relationship between signal and control), in good agreement with experimental data. Figure 4.15 shows oscilloscope traces of 20 Gb/s and 40 Gb/s demultiplexing operation. The top trace is the passively multiplexed data using a 10 Gb/s PRBS word length of 2^7-1 (the oscilloscope trace cannot be triggered using a 2^{31}-1 PRBS pattern sync.), the middle trace is the 10 Gb/s clock stream, and the bottom trace is the demultiplexed stream. As expected, the 10 Gb/s clock stream samples the data stream at the frame rate. Since we are using a 45 GHz bandwidth detector and a 50 GHz bandwidth oscilloscope, we expect that much of the background noise, especially on the “0” level” is due to ringing. The bit error rate (BER) measurement is shown in Figure 4.16 with received power in dBm on the horizontal axis and -log(BER) on a log-scaled vertical axis. The word length of the 10 Gb/s PRBS was 2^{31}-1. Consequently, the lowest frequency component in the PRBS is $10\text{GHz}/(2^{31}-1) = 4.66$ Hz, justifying the use of a DC to 18 GHz photodetector.

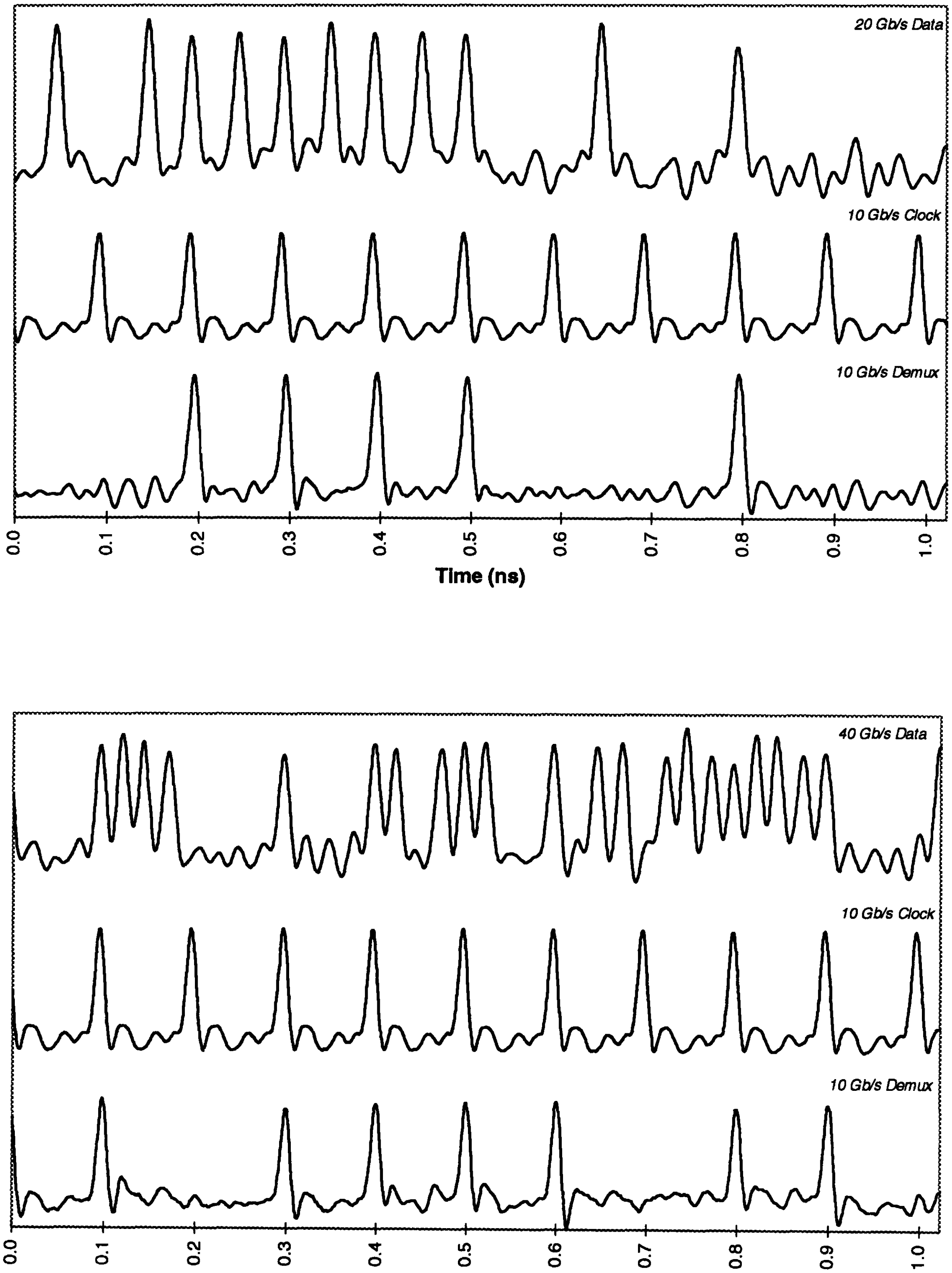

Figure 4.15: UNI *Demultiplexer Scope Traces at 20 Gb/s (a) and 40 Gb/s (b)*

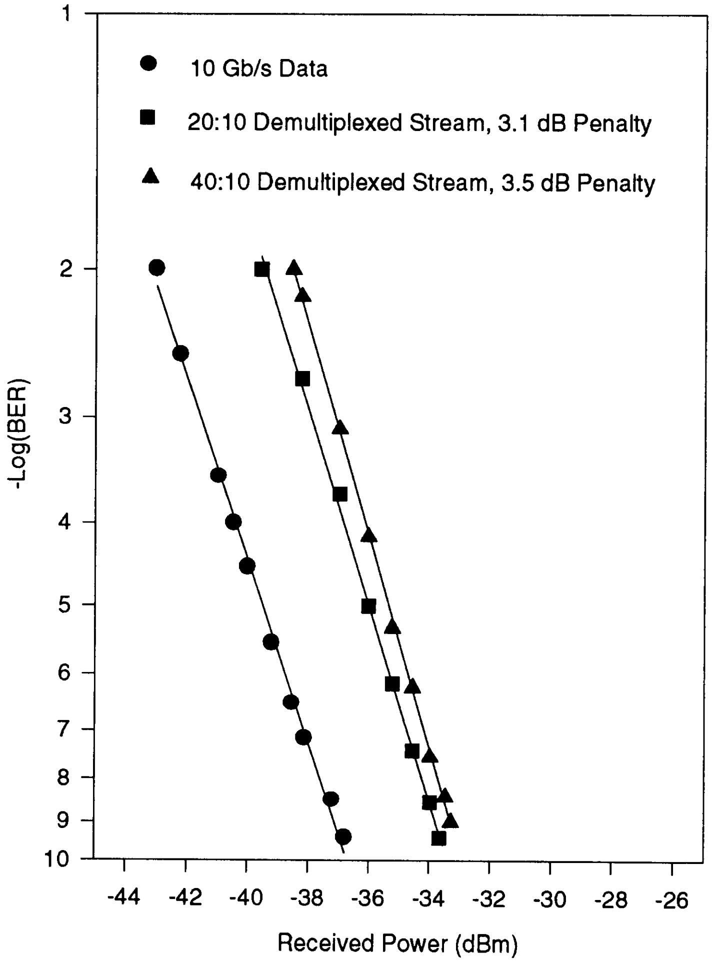

Figure 4.16: ***UNI Demultiplexer BER***

The baseline BER data was obtained from the 10 Gb/s electro-optically modulated PRBS. We see a BER of 10^{-9} at a received power of -37 dBm (200 nW) corresponding to 155 photons/bit (quantum limit is 45 photons/bit). The BER measurement shows incurred power penalties due to demultiplexing of 3.1 and 3.5 dB respectively

To investigate the degree of pulse distortion, and intersymbol interference, at the output of the UNI, we measured the output pulse widths. Figure 4.17a shows an autocorrelation trace (ATC) of the output signal pulse in the absence of the control (i.e. the UNI was biased ON to transmit the signal). Figure 4.17b shows an ATC of the output control pulse. Figure 4.17c shows an output demultiplexed pulse from a 40 Gb/s data stream of all 1's. We see that in the absence of the control pulse, the signal actually broadens slightly from 8.3 ps to 10.3 ps due to GVD in the normal dispersion regime, thus indicating that the observed narrowing of the switched output pulse must be due to the control pulse. The control pulse, on the other hand, is clearly compressed to 2.8 ps due to soliton effects. The theoretical peak power required to maintain a fundamental soliton with a 2.8 ps pulsewidth in the DSF is approximately 27 mW. The actual control peak power in the experiment was 260 mW (assuming a 10:1 duty ratio). As evidenced by the temporal side-lobes and pedestal in Figure 5.3b, high order soliton compression is occurring. Due to the control pulse compression, the switched output pulse has also narrowed from 8.3 ps to 4.8 ps (a 43% reduction) because an appreciable phase shift is imparted only to a small central fraction of the signal pulse. The output pulse, however, does not assume the same pulsewidth as the output control pulse due to the non-instantaneous evolution of the high order soliton. Considering the width of the demultiplexed output pulse, intersymbol interference is not likely to be a major contributing factor to the BER

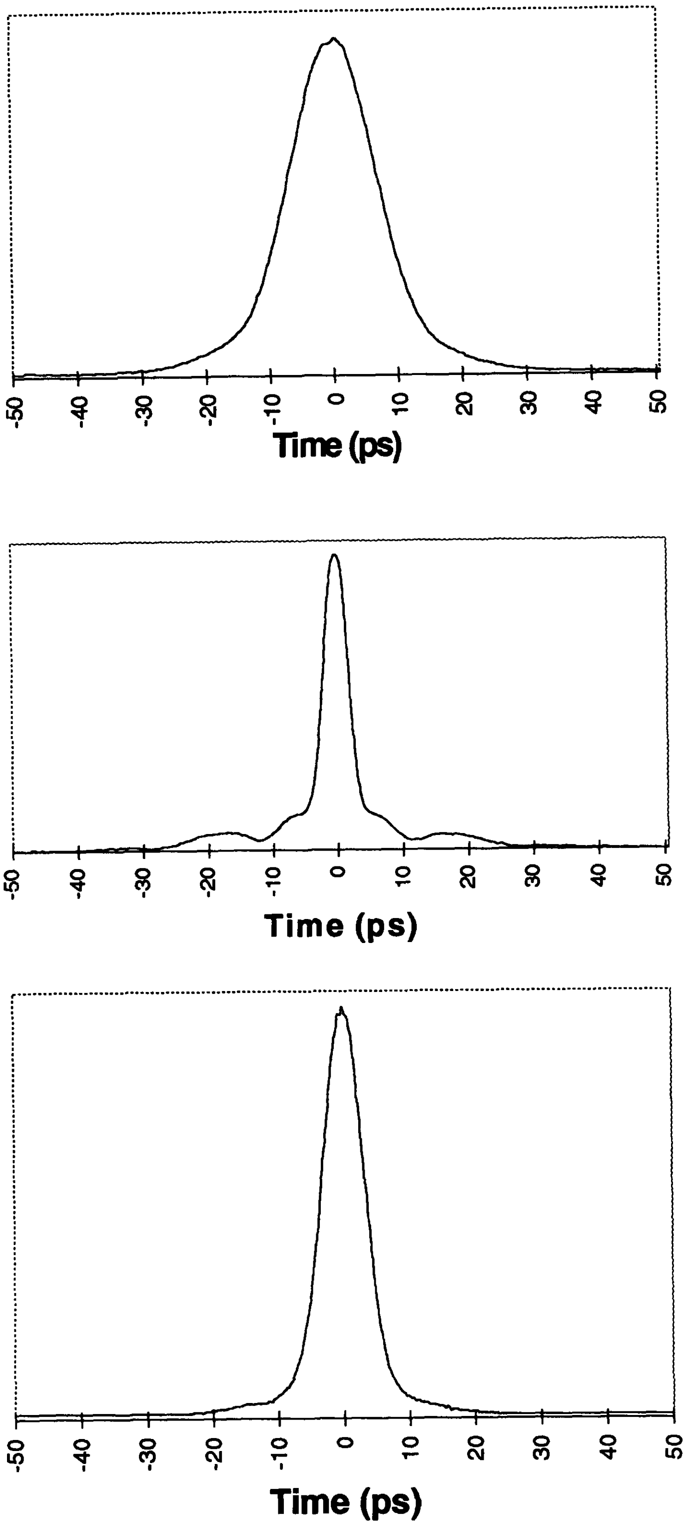

Figure 4.17a,b,c: *Output Autocorrelation Traces*

We have also demonstrated a 10 Gb/s bit-wise inverter using the UNI with a fiber nonlinearity. The role of the clock and data are now switched. Namely, the 10 Gb/s data PRBS enters the control port of the UNI, the 10 Gb/s clock stream enters the signal port, and the UNI is biased ON. The clock and data wavelengths were 1548.2 nm and 1544.5 nm respectively. We chose the data wavelength to be in the normal dispersion regime in order to obtain slight pulse broadening and thus, more uniform phase shifts imparted to the clock (signal) pulses. Since the data bit period is 100 ps (as opposed to 25 ps in the demultiplexer experiment), ISI due to control pulse broadening is insignificant. The clock and data average powers entering the DSF were 3.86 mW and 16.3 mW respectively. Figure 4.18 shows an oscilloscope trace of the bit-wise inverter. As before, a 2^7-1 word length PRBS was used. We see that the 0:1 contrast ratio is 1:4 (75%). We attribute this non-ideal contrast ratio to the inability to obtain a uniform π phase shift across the signal pulse, despite our efforts to take advantage of control pulse broadening. The theory predicts that there was no walk-through of signal and control (wavelengths approximately straddled 1547 nm) in addition to the fact the data pulse should broaden from 8.3 ps to 10.1 ps. Thus, the control to signal pulse-width ratio (defined in section 3.1.1) evolves from 1.3 to 1.5 along the length of fiber. According to Figure 3.3b, we would thus expect a switching ratio between 0.1 and 0.13 which translates to a contrast ratio of approximately 88%. The discrepancy between the observed and theoretical results could be due to a number of things. It is possible that the signal and control overlap was not optimized, or that the data (control) power was too high leading to phase shifts greater than those necessary to obtain an optimal contrast. Figure 4.19 shows the BER measurement. The incurred power penalty due to inverter operation is approximately 3.8 dB. As we will show in section 4.3.2, a 75% contrast ratio should lead to an additional 2.2 dB power penalty as compared to the ideal contrast case. In fact, we see only a 0.3 to 0.7 dB additional power penalty with respect to demultiplexing. The latter suggests that the inverter was not optimized at the time the oscilloscope trace was taken, leading to an unexpectedly low contrast ratio and thus high theoretical power penalty.

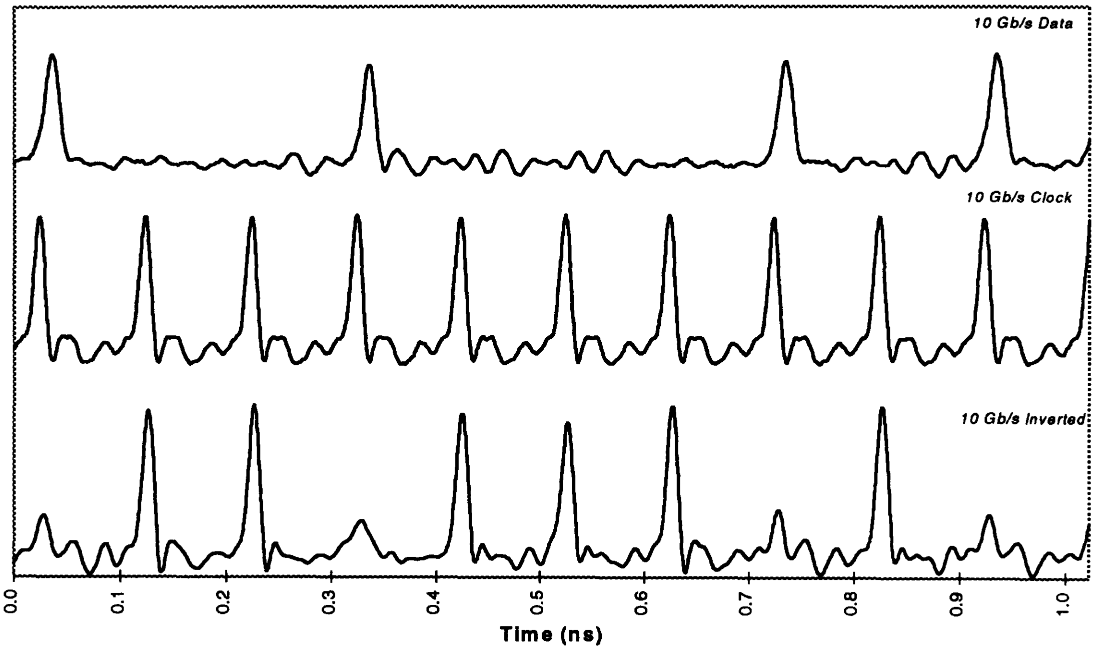

Figure 4.18: *10 Gb/s Inverter using a UNI*

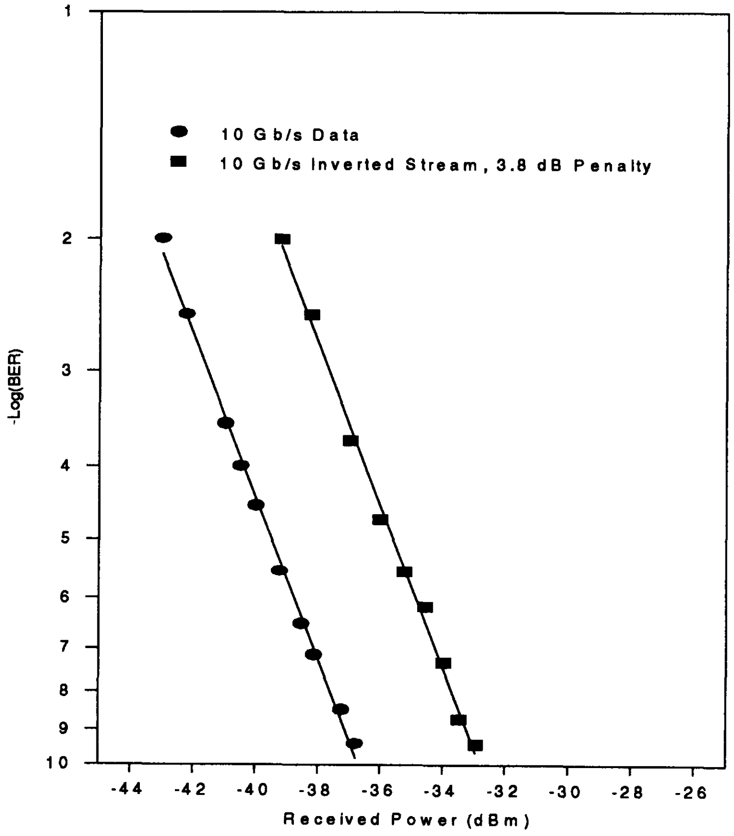

Figure 4.19: *UNI Inverter BER*

4.3.2 SADINI - Demultiplexing and XOR Gating

Recall that in the SADINI geometry, the signal and control pulses are both interfered. This obviated the use of a filter at the device output in addition to allowing XOR gating. To compare the performance to the UNI, we have used the SADINI geometry to perform 20 Gb/s demultiplexing using the setup of Figure 4.14. As stated in section 3.1, demultiplexing requires both inputs of the SADINI to be biased OFF. We found experimentally that the primary contributing factor to the lack of full destructive interference between the orthogonal polarizations was cross phase modulation between the wings of the 2 components. The reason why this causes interference degradation is because the two polarization components are asymmetrically phase modulated by each other. More specifically, the trailing edge of one is modulated, while the leading edge of the other pulse is modulated. Consequently, when the two components are recombined, high quality interference is only obtained over the central portion of the pulse. Since the two source external cavity lasers were not identical, the achievable pulse widths for each were different, as shown in Figure 4.5. Thus, I chose the shorter pulse source with a FWHM of 6.5 ps to be the control which would be more vulnerable to cross phase modulation between adjacent orthogonal polarizations due to its higher intensity. The signal and control wavelengths were set at the dispersion zero of the DSF (Figure 4.20) to avoid pulse walk-off. The signal and control average powers were 3.6 mW and 22 mW respectively, again in good agreement with theory.

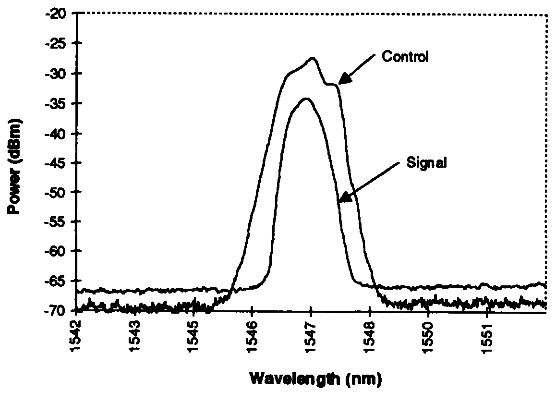

Figure 4.20: ***Mode-locked Source Power Spectra,*** $\lambda_s = \lambda_c = 1547$ ***nm***

An oscilloscope trace of 20 Gb/s demultiplexing is shown in Figure 4.21. From top to bottom are the 20 Gb/s data (signal), 10 Gb/s clock (control), and 10 Gb/s demultiplexed streams. Figure 4.22 shows that the output demultiplexed pulsewidth is 9.3 ps, broadened by 1 ps from the input signal pulse.

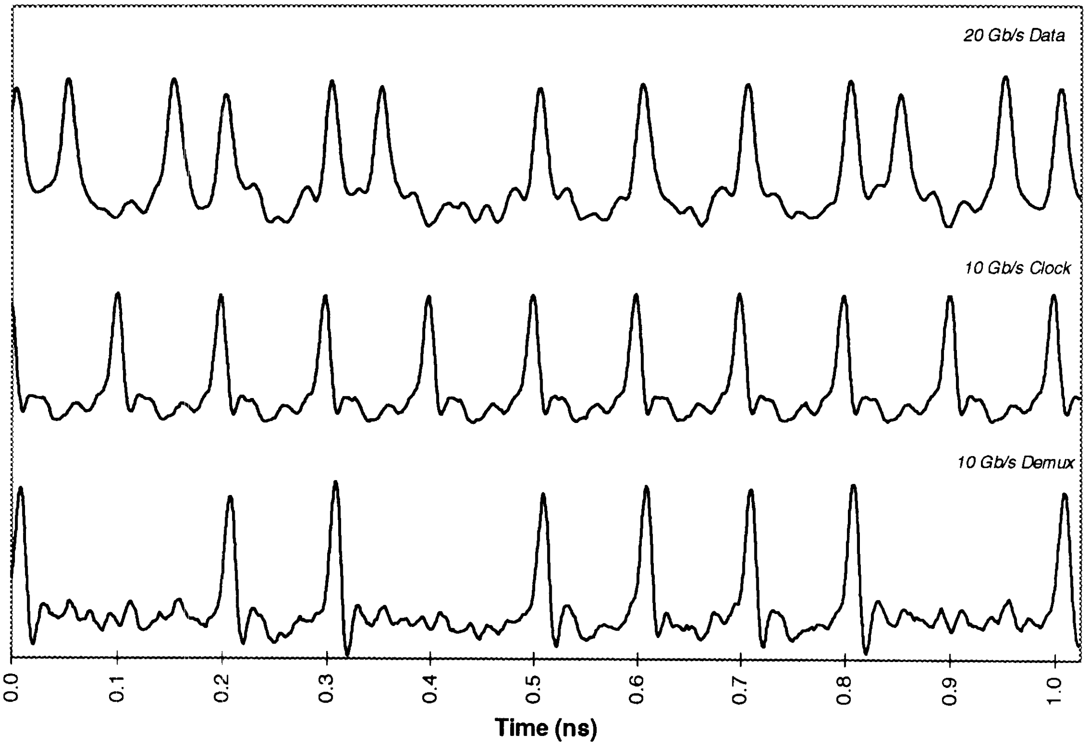

Figure 4.21: ***20 Gb/s Demultiplexing Using a SADINI***

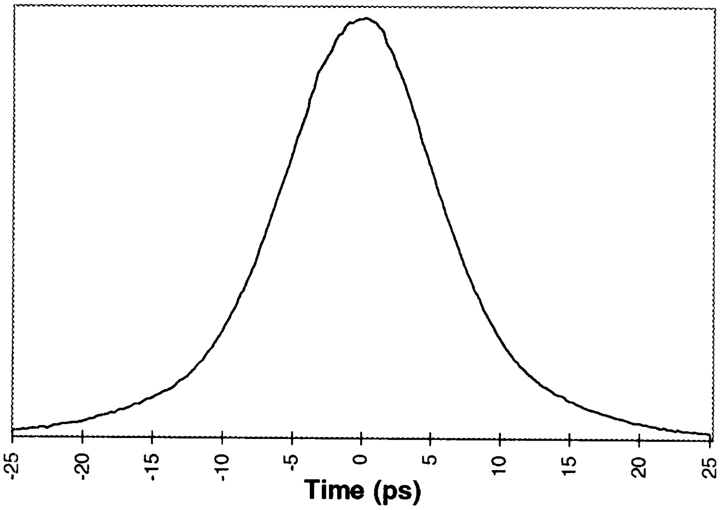

Figure 4.22: ***Demultiplexed Output Pulse Autocorrelation Trace***

The results of the BER measurement are shown in Figure 4.23. A 3.3 dB power penalty is incurred due to demultiplexing. As compared to 20 Gb/s demultiplexing using the UNI with control filtering, only a 0.2 dB difference in power penalty is observed. Thus, it is reasonable to assume that device performance is not sacrificed by biasing the control stream OFF, as opposed to filtering it out.

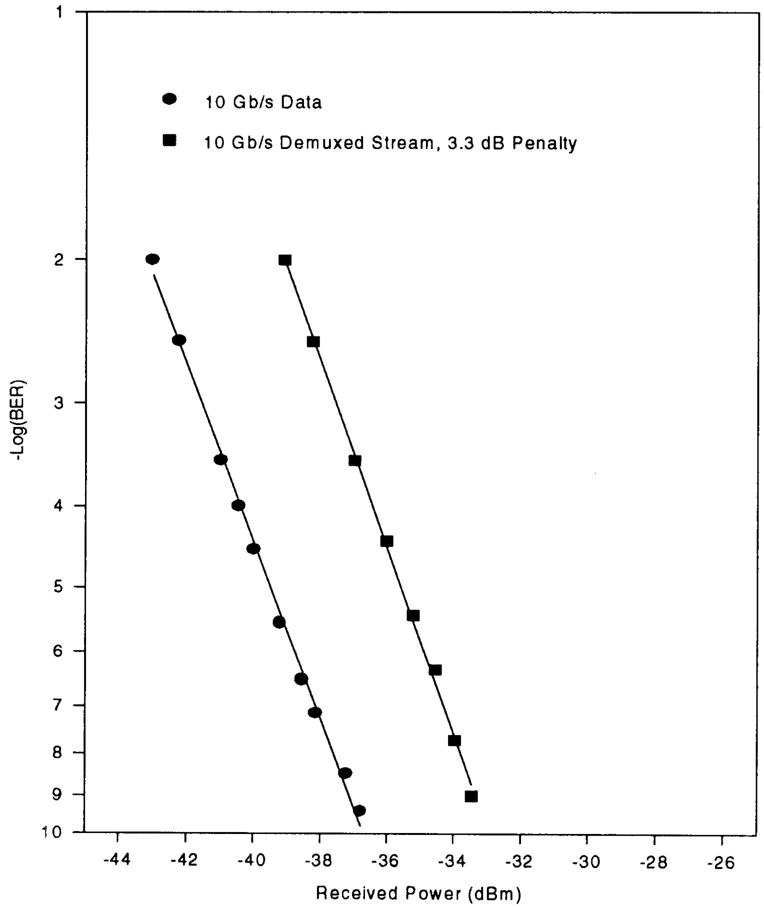

Figure 4.23: ***SADINI Demultiplexer BER***

The interesting new function obtainable with the SADINI is XOR in which both inputs (A, B) are biased ON and are of comparable intensity. To perform BER measurements, we chose a 10 Gb/s PRBS as input A and a 10 Gb/s clock stream for input B. The desired output stream should be the logical inverse of A. We use the same experimental setup as before. The only difference is that a 15 m length of BRF (instead of 7.5 m) was used to give rise to a PSD of 25 ps. The input wavelengths were chosen to be 1547.8 and 1551.9 nm, both above the dispersion zero and giving rise to a calculated pulse walk-through of approximately 7 ps. The A and B average powers entering the DSF were 19.3 mW and 25.4 mW respectively. Figure 4.24 shows the oscilloscope trace of 10 Gb/s XOR gate operation. We see a 4:1 contrast ratio on the output stream. We attribute this again to non-uniform phase shifts since full pulse walk-through is not achieved. Indeed, due to the manner in which the four pulses are timed, a maximum walk-through of half a polarization sensitive delay (~12.5 ps) is allowed before similarly polarized pulse components from different inputs begin to interact.

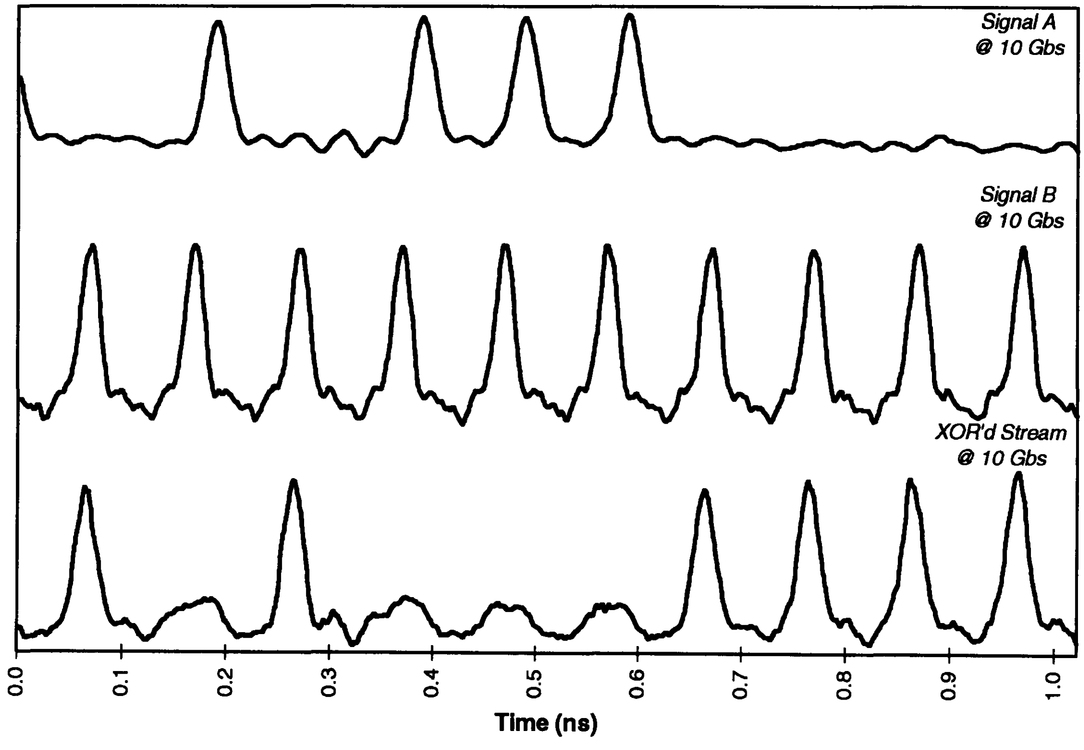

Figure 4.24: *XOR Gating Using a SADINI*

Due to the long nonlinear interaction length (8.8 km) and high pulse peak powers (~ 0.2 W), we observed four wave mixing (FWM) spectral components at the output of the device. Figure 4.25 shows a power spectrum at the output of the SADINI showing the effects of FWM. The generated side-bands are equally spaced in frequency (and also approximately in wavelength over this small regime) because FWM generates sum and difference frequency components. We see that the largest FWM component is 8 dB below signal A. Since FWM is a cross-correlation mechanism, FWM pulses at the output of the SADINI appear in the presence of both signal A and B pulses, performing an AND operation. Consequently, FWM can cause a reduction in the 0:1 contrast ratio in the case of XOR because when both input pulses are present, we desire a "0" at the output. This led us to place a filter after the SADINI to reduce the power in the FWM components. It should be noted that the filter pass band should be placed between signal A and B so as to avoid significantly changing the relevant output spectrum. Figure 4.26 shows the filtered output spectrum where we have placed the filter center to maintain the power difference between signals A and B. The largest FWM component is now about 17 dB down from signal A.

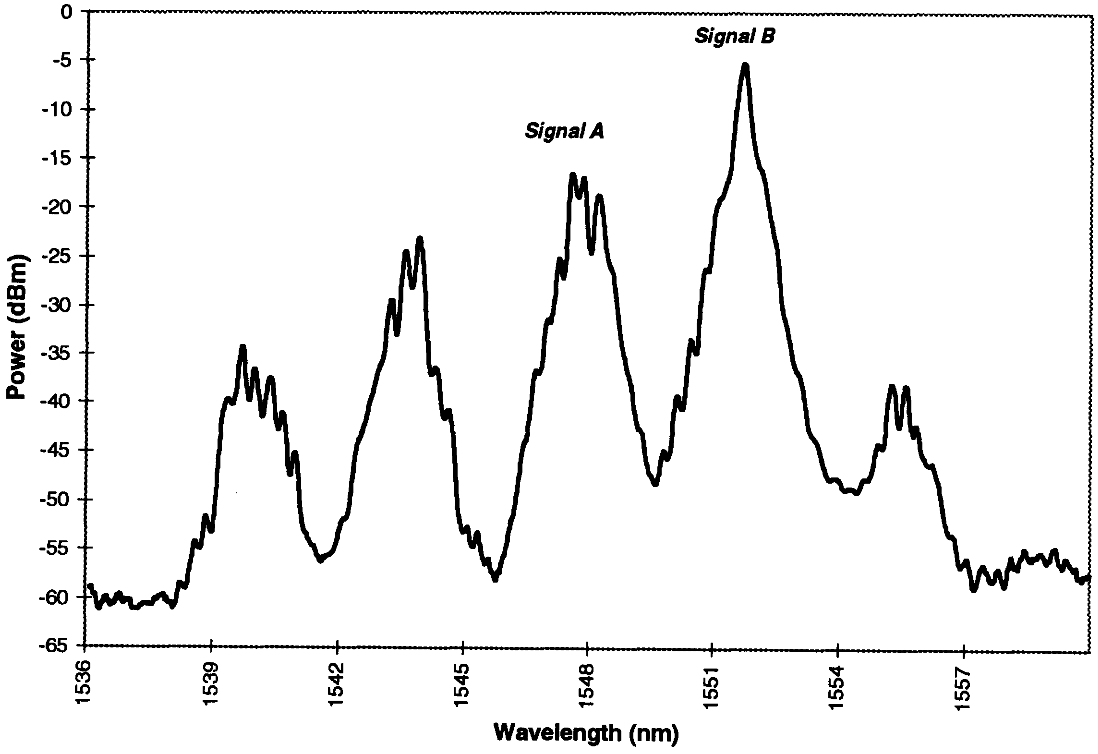

Figure 4.25: *Output Power Spectrum for XOR Operation Using the SADINI*

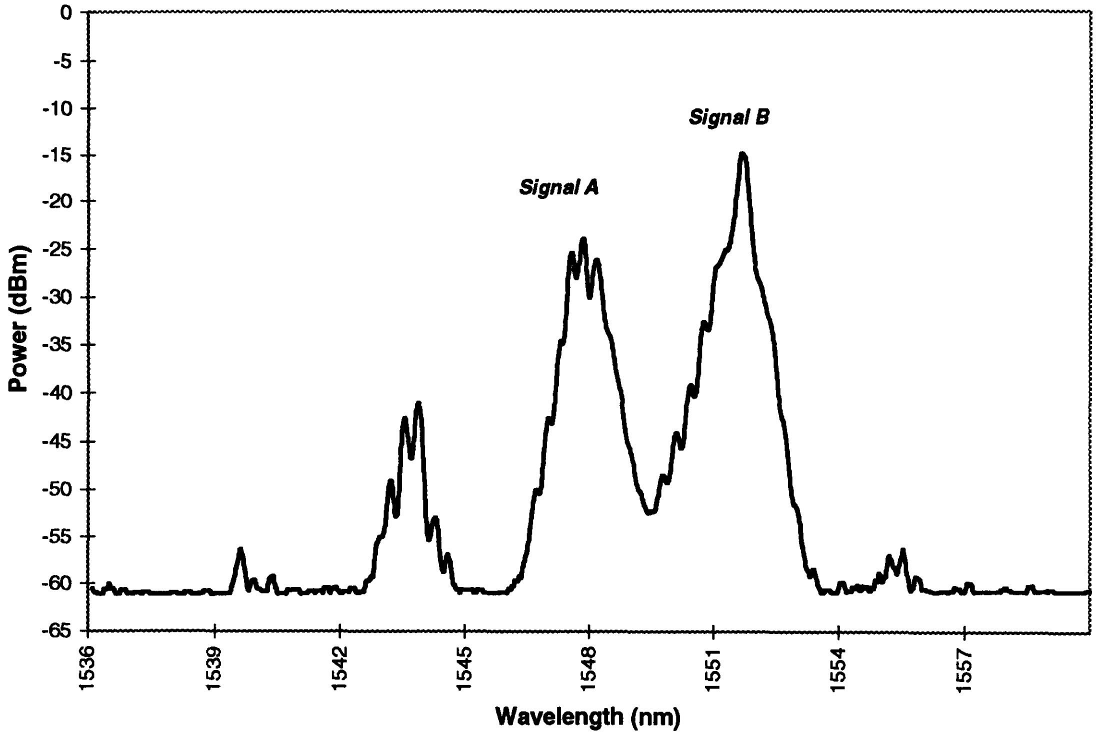

Figure 4.26: *Filtered Output Spectrum*

Finally, the BER measurement for XOR operation is shown in Figure 4.27 where we see a 6 dB power penalty, considerably larger than in the case of demultiplexing. However, the additional 2.7 dB penalty is easily explained by the 4:1 contrast ratio. One can do a simple analysis of the probability of error for a binary pulse amplitude modulated (PAM) signal with arbitrary 0:1 contrast ratio in white Gaussian noise (WGN). We define the received optical powers for the logical "0" and "1" to be s_0 and s_1 respectively. The average received optical power is $(s_0 + s_1)/2$, and the extinction ratio is defined to be $r = s_0 / s_1$. Since the signal is amplified in an EDFA before entering the BERT, the noise variances for the logical "0" and "1" are in general, different. Thus, we model the noise as Gaussian with variances σ_0 and σ_1. The resulting probability of error is: $\Pr[E] = Q\left\{ \frac{2P}{\sigma_0+\sigma_1}\frac{1-r}{1+r} \right\}$

where $Q\{x\} = \frac{1}{\sqrt{2\pi}} \int_x^\infty e^{-\frac{1}{2}u^2} du$. The factor (1-r)/(1+r) is the power penalty. For r=.25, as is the case for the observed XOR operation, we find an incurred penalty of approximately 2.2 dB with respect to the case of ideal contrast ratio (i.e. r=0). This compares nicely to the observed 2.7 dB power penalty between XOR and demultiplexing operation. Of course, we have explicitly assumed that r = 0 for the demultiplexing experiment. Lastly, we expect that the contrast ratio can be improved with the utilization of shorter pulses so as to allow full walk-through. Unfortunately, as the pulse widths approach a few picoseconds, dispersion becomes a major obstacle to overcome. Placing the input wavelengths in the anomalous dispersion regime and taking advantage of soliton effects would probably yield the best results.

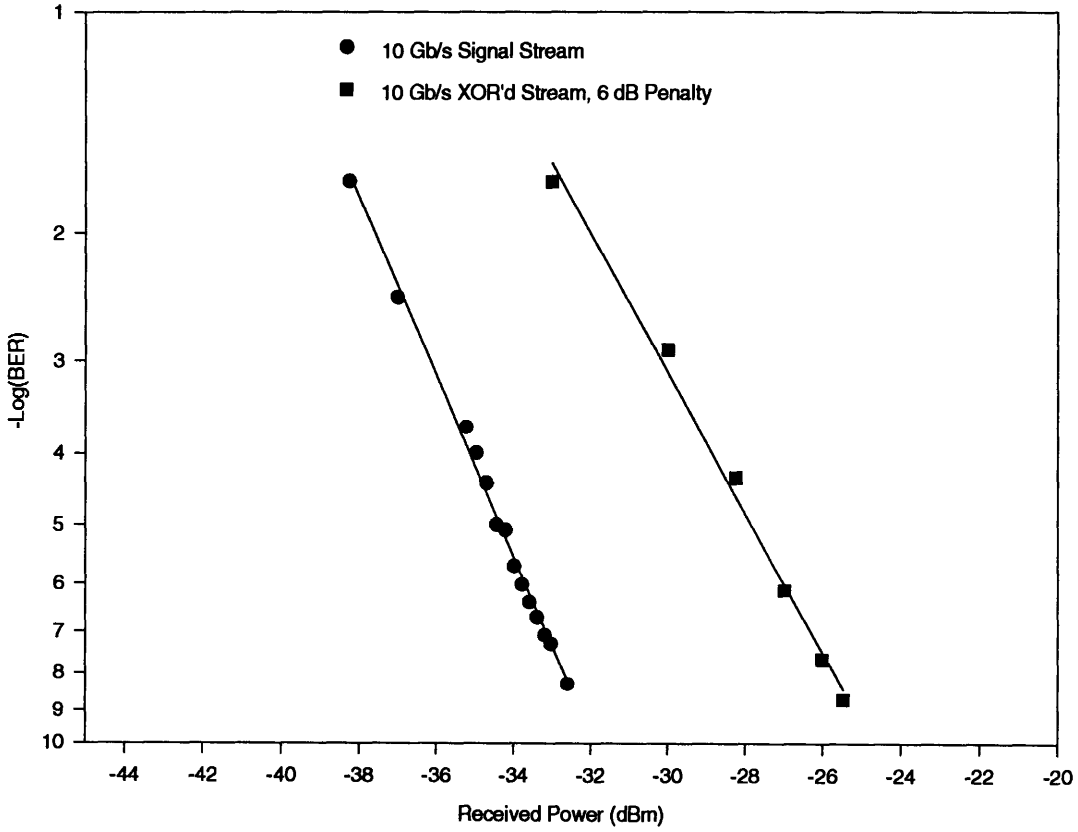

Figure 4.27: ***SADINI XOR BER***

4.4 Switching Results Using a Semiconductor Nonlinearity

4.4.1 UNI / SLA - Demultiplexing and Inverting

Instead of using dispersion shifted fiber for nonlinearity in the UNI, we have used a semiconductor laser amplifier (SLA) to perform demultiplexing and inverting at rates up to 40 Gb/s. The particular SLA we used was a multiple quantum well (MQW) laser diode with antireflection coated facets and a gain peak around 1490 nm. In the experiments to be described in this section, the SLA was biased with a 200 mA current. We expect that the high bias current and thus high equilibrium carrier density reduces the upper state lifetime of the material to a few hundred picoseconds via non-radiative recombination of carriers within the active region. A pump-probe study of the carrier density dependence of the upper state lifetime should verify this.

To avoid large gain nonlinearities, we chose the signal and control wavelengths to be above the gain peak of the SLA where refractive index nonlinearities are expected to be dominant. This can be theoretically understood since the linewidth enhancement factor, α, diverges at the band edge. It is important to note that although the gain nonlinearities become insignificant close to the band edge, two photon absorption is still present, especially if the incident optical power is high. Moreover, the refractive index nonlinearities become progressively weaker as one moves towards and below the band edge. One must strike a balance between the increase in α and a decrease in the magnitude of the refractive index nonlinearity depending on the desired device function.

An upper limit on the source wavelengths was set by the band pass filters we used to filter out ASE from the EDFA's which had cut off wavelengths at 1567 nm. Note that even if this limit did not exist, the amplification obtainable from EDFA's decreases rapidly above 1570 nm and thus we still could not increase the source wavelengths considerably. Figure 4.28 shows the gain spectrum of the SLA, the Erbium band, and our placement of the source wavelengths.

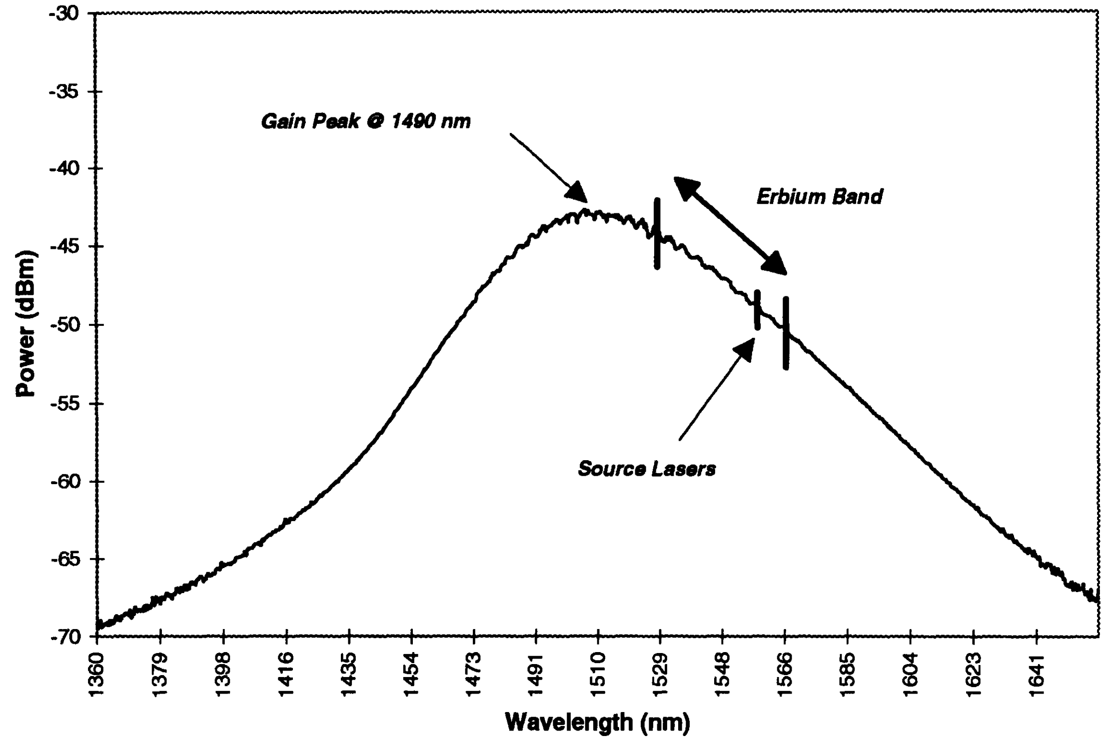

Figure 4.28: *SLA Gain Spectrum*

The experimental setup for demultiplexing using the UNI / SLA is the same as before (Figure 4.14). The signal and control wavelengths were 1561.5 nm and 1564.72 nm respectively. For 20 Gb/s demultiplexing, the average data (signal) and clock (control) powers entering the SLA were 4.3 mW and 18 mW respectively. Those for 40 Gb/s demultiplexing were 10.2 mW and 25 mW. The UNI was biased ON and the output filter was adjusted to pass the data pulses. Oscilloscope traces of 20 Gb/s and 40 Gb/s demultiplexing are shown in Figure 4.29. The top trace is obtained by biasing the UNI ON (i.e. transmitting the data pulses) in the absence of the clock pulses. The middle trace is the clock stream and the last trace is the demultiplexed stream. On both the data stream and the demultiplexed stream, patterning due to gain dynamics is observable. The BER measurement is shown in Figure 4.30 where we observe a 3.0 dB and 3.1 dB power penalty for 20 Gb/s and 40 Gb/s demultiplexing. It is interesting to note that the results are no worse than in the fiber case. Thus, we have reduced the nonlinear interaction length by 7 orders of magnitude without a sacrifice in performance.

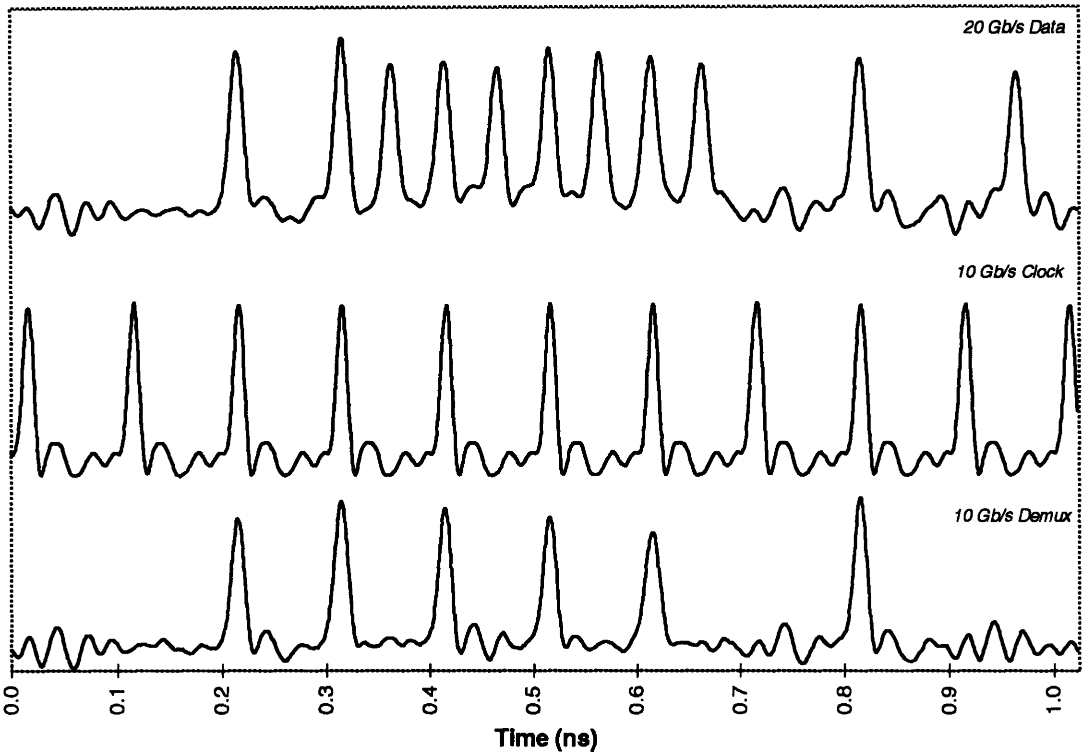

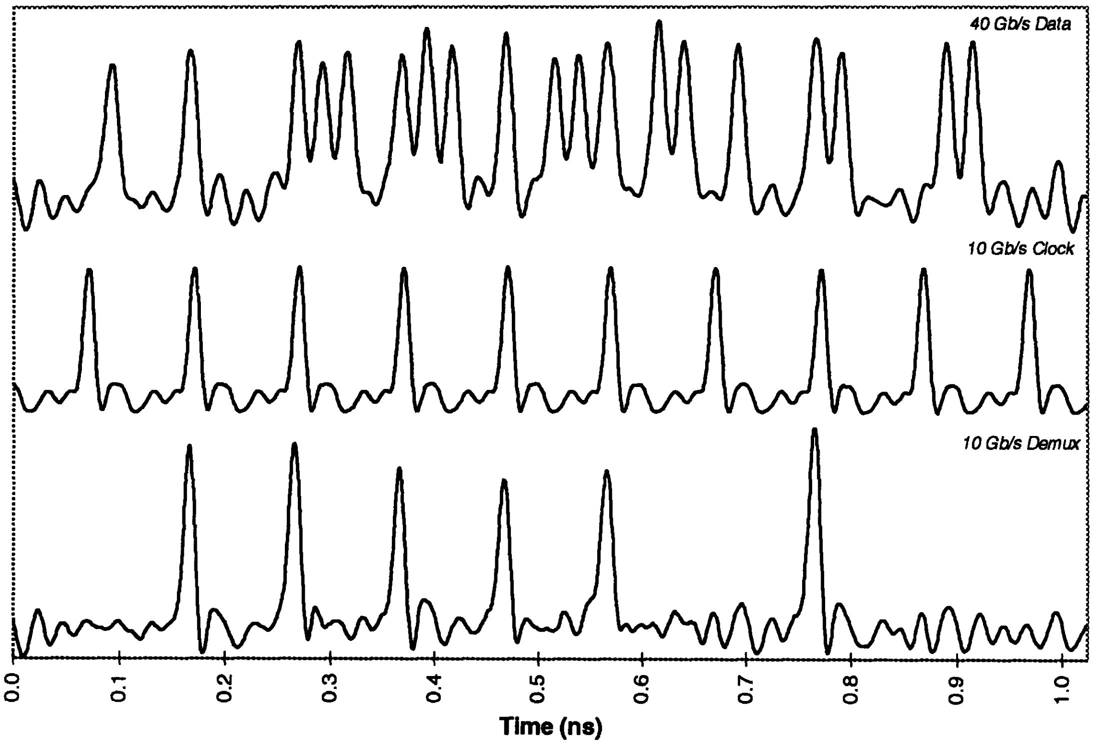

Figure 4.29: *Demultiplexing Using a UNI / SLA*

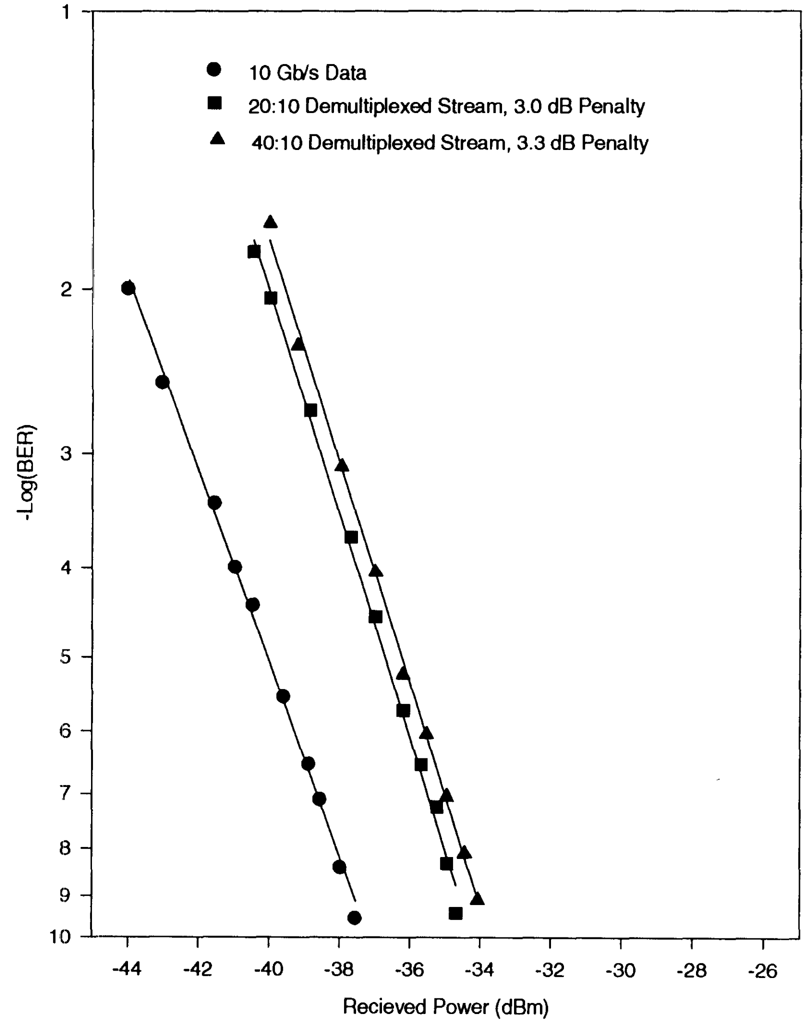

Figure 4.30: ***UNI / SLA Demultiplexer BER***

As before, we measured the output signal pulse widths in the absence of the control (i.e. UNI biased ON) and the output demultiplexed pulse widths. Of course, in this case we used a data stream of all 1's. Figure 4.31a shows an autocorrelation trace of the output signal pulse in the absence of the control pulse. It has broadened only slightly from 8.3 ps to 8.7 ps. Figure 4.31b shows the demultiplexed output pulse which has narrowed slightly to 7.7 ps. We expect that this is due to shaping by the control pulse which is 6.5 ps. The background on the lower trace is due to data pulses that are not adequately switched out. More refined biasing of the interferometer would likely alleviate this problem.

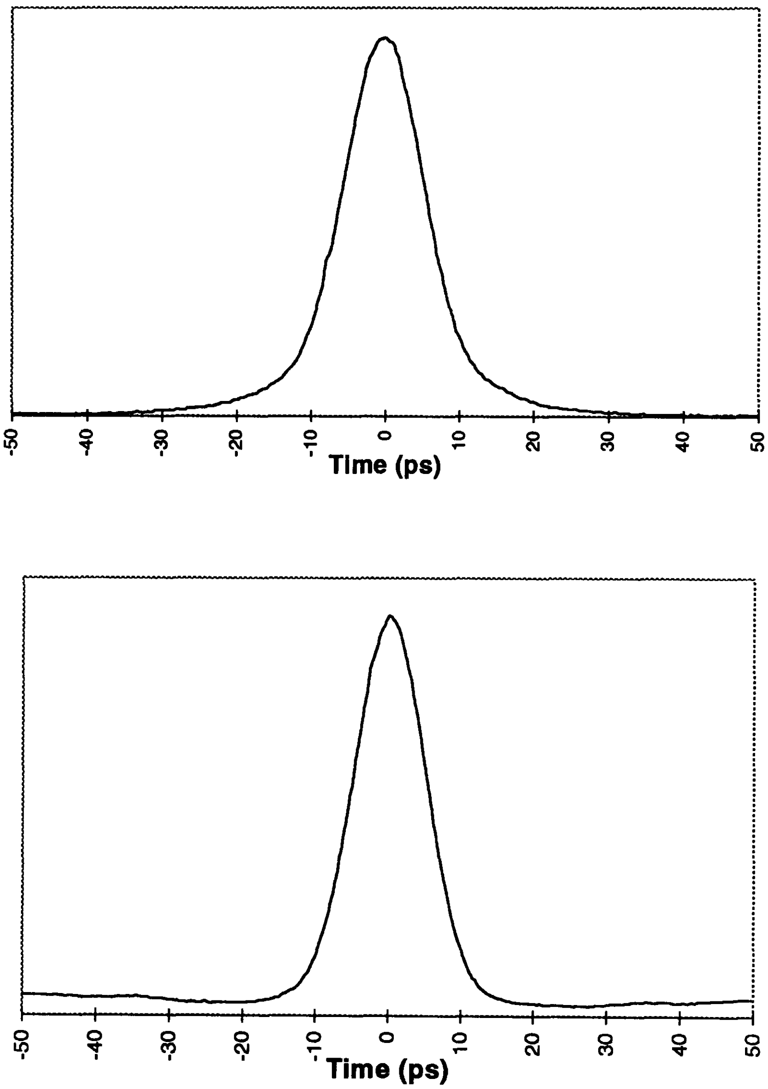

Figure 4.31a,b: ***UNI / SLA Output Autocorrelation Traces***

We have also performed bit-wise inversion at rates up to 40 Gb/s using the UNI / SLA. The data stream enters the control port of the UNI while the clock stream enters the signal port and the UNI is biased ON. The wavelengths were the same as in the demultiplexing experiment. For the case of 10 Gb/s inverter operation, the average clock and data powers entering the SLA were 6 mW and 36 mW respectively. Figure 4.32 shows an oscilloscope of 10 Gb/s inverter operation. We see much better contrast ratio that in the fiber inverter case and this shows as a marked improvement in the BER measurement (Figure 4.33) where we observe a 2.9 dB power penalty. This improvement can be attributed to the fact that cross gain saturation is helping to non-interferometrically turn the signal pulses OFF by reducing the overall output pulse intensity.

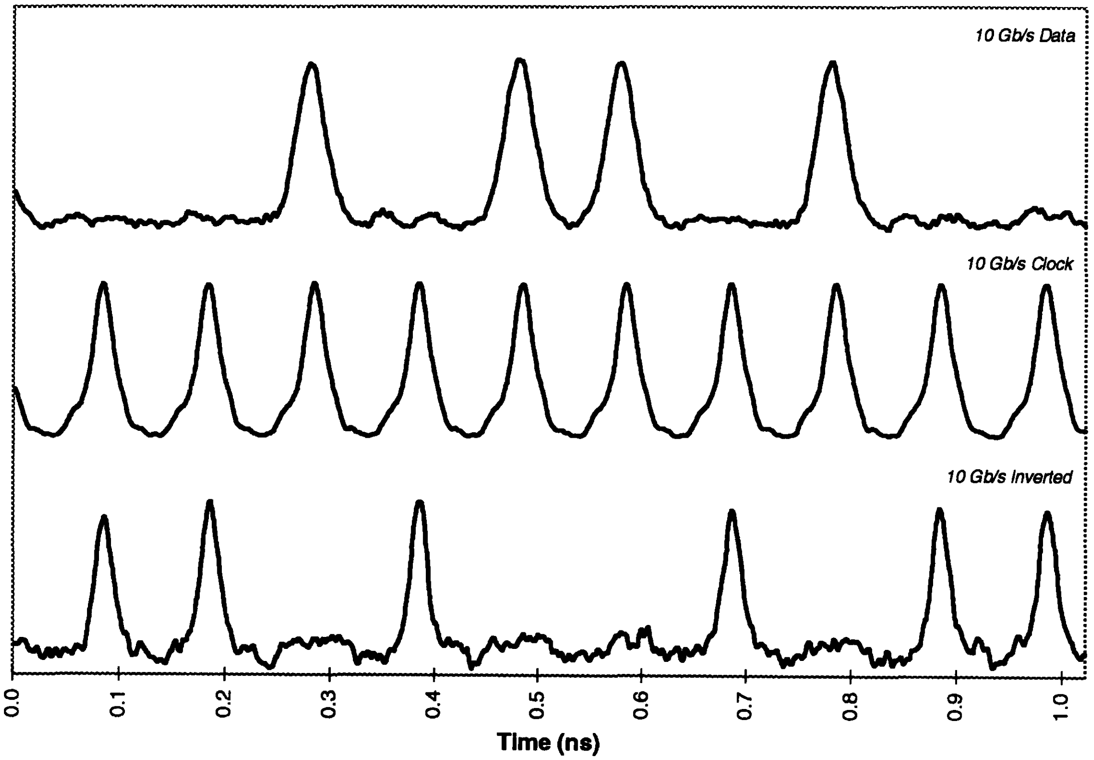

Figure 4.32: *10 Gb/s Bit-Wise Inverting Using a UNI / SLA*

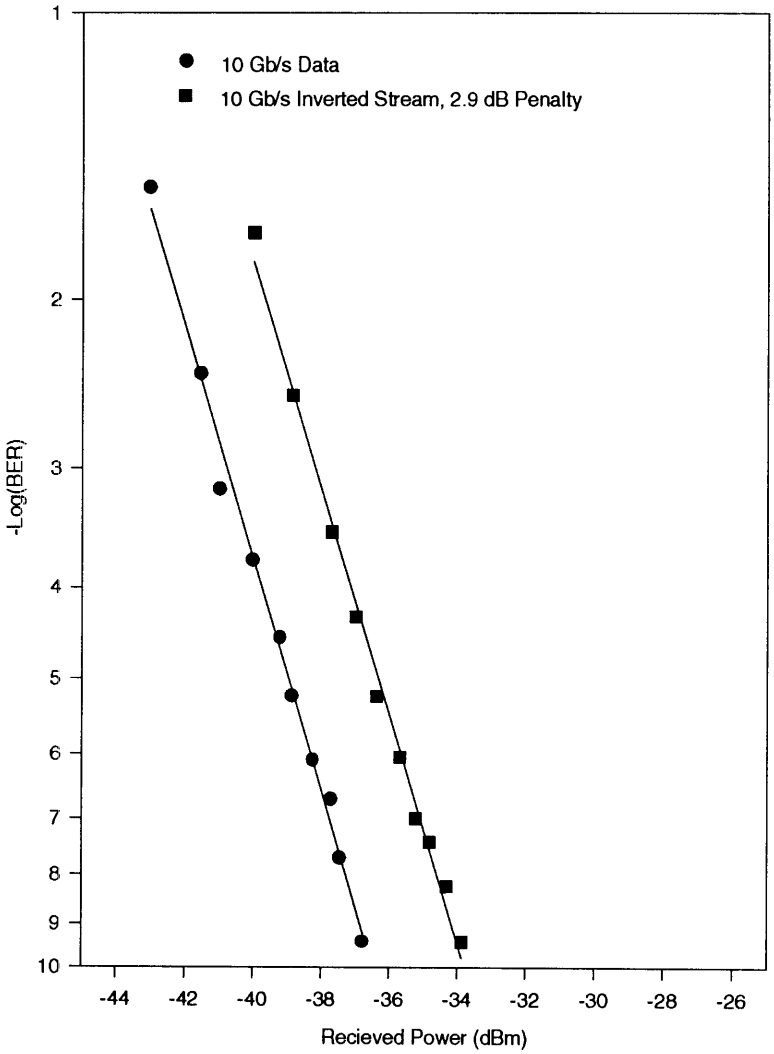

Figure 4.33: *UNI / SLA Inverter BER*

Lastly, we have demonstrated 40 Gb/s bit-wise inversion as shown in Figure 4.34. The clock stream was generated by a soliton compression source (SCS) as described in section 4.1.2. The clock and data average powers entering the SLA were approximately 20 mW and 85 mW respectively. Pulse distortion and patterning due to gain dynamics are clearly observed. This is due to the fact that the long-lived gain modulation relaxes on time scales longer than 25 ps (the bit period). The noise on the "0" level is most likely due to ringing in the 45 GHz detector. As it is, the 4 ps clock pulse train is clearly not resolved by the detector.

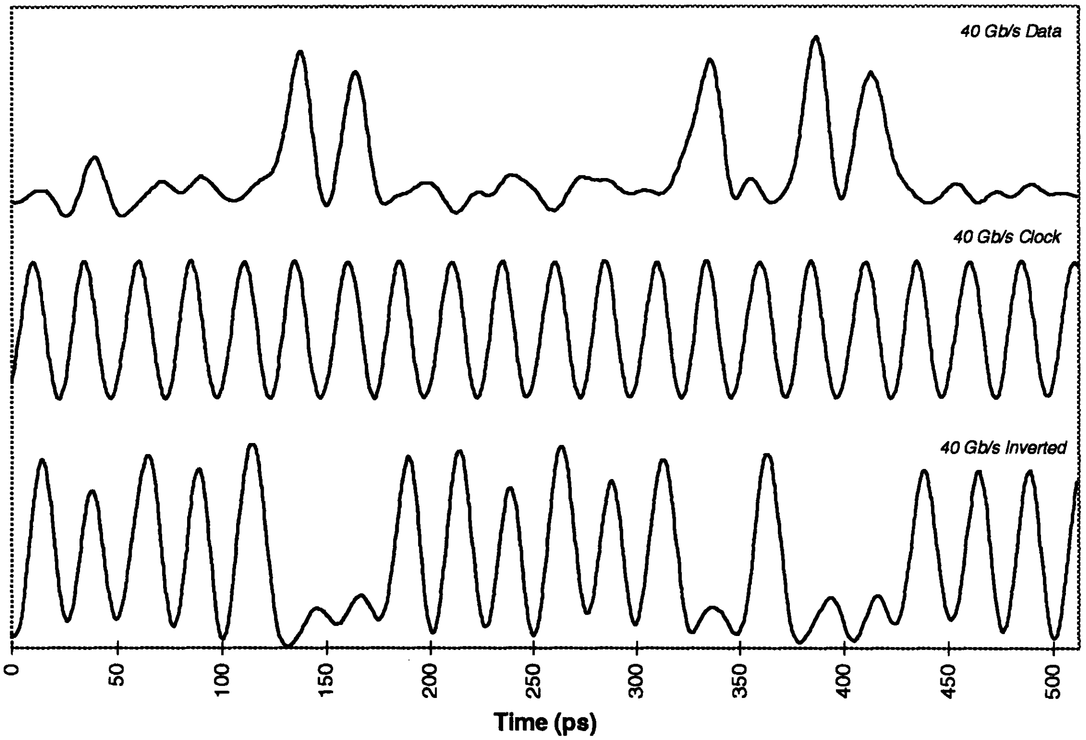

Figure 4.34: *40 Gb/s Inverting Using a UNI / SLA*

4.4.2 UNI / SLA with Counter-Propagating Control - Demultiplexing, Inverting, and OR, NOR Gating

Recall that by using a counter-propagating control in the UNI geometry, we gain device cascadability and a reduction in implementational complexity by removing a filter at the device output. Moreover, the theory from section 3.2.3 predicted that as long as the pulse widths in the spatial domain are comparable to the length of the SLA, the nonlinear interaction is very similar to the co-propagating case. Indeed, we observe no difference in switching performance between the two geometries as we will show next.

As usual, we use the generic experimental setup for demultiplexing. To show device cascadability, we chose both the data and the clock wavelengths to be 1560 nm. For 20 Gb/s demultiplexing, the data and clock average powers entering the SLA were 8 mW and 27 mW respectively. Those for 40 Gb/s demultiplexing were 13 mW and 30 mW. Figure 4.35 shows the oscilloscope traces for 20 and 40 Gb/s demultiplexing. We observe correct demultiplexing operation and very good contrast ratio. The BER measurement is shown in Figure 4.36 showing a 2.9 dB and 3.1 dB power penalty for 20 Gb/s and 40 Gb/s demultiplexing. The interesting result is that we observe no degradation in the BER measurement as compared to the co-propagating control case. Although this measurement yields incurred powers penalties a few tenths of a dB better than the co-propagating scenario, we cannot say that the counter-propagating scheme works better based on such a small difference. The parameter space for these experiments is so large that it is difficult to make definitive statements on performance comparisons unless the results are clearly dissimilar. We can at least say, however, that for the regime in which the pulse widths are comparable to the SLA interaction length, the two device geometries are equivalent from a performance perspective (as was predicted by the theory).

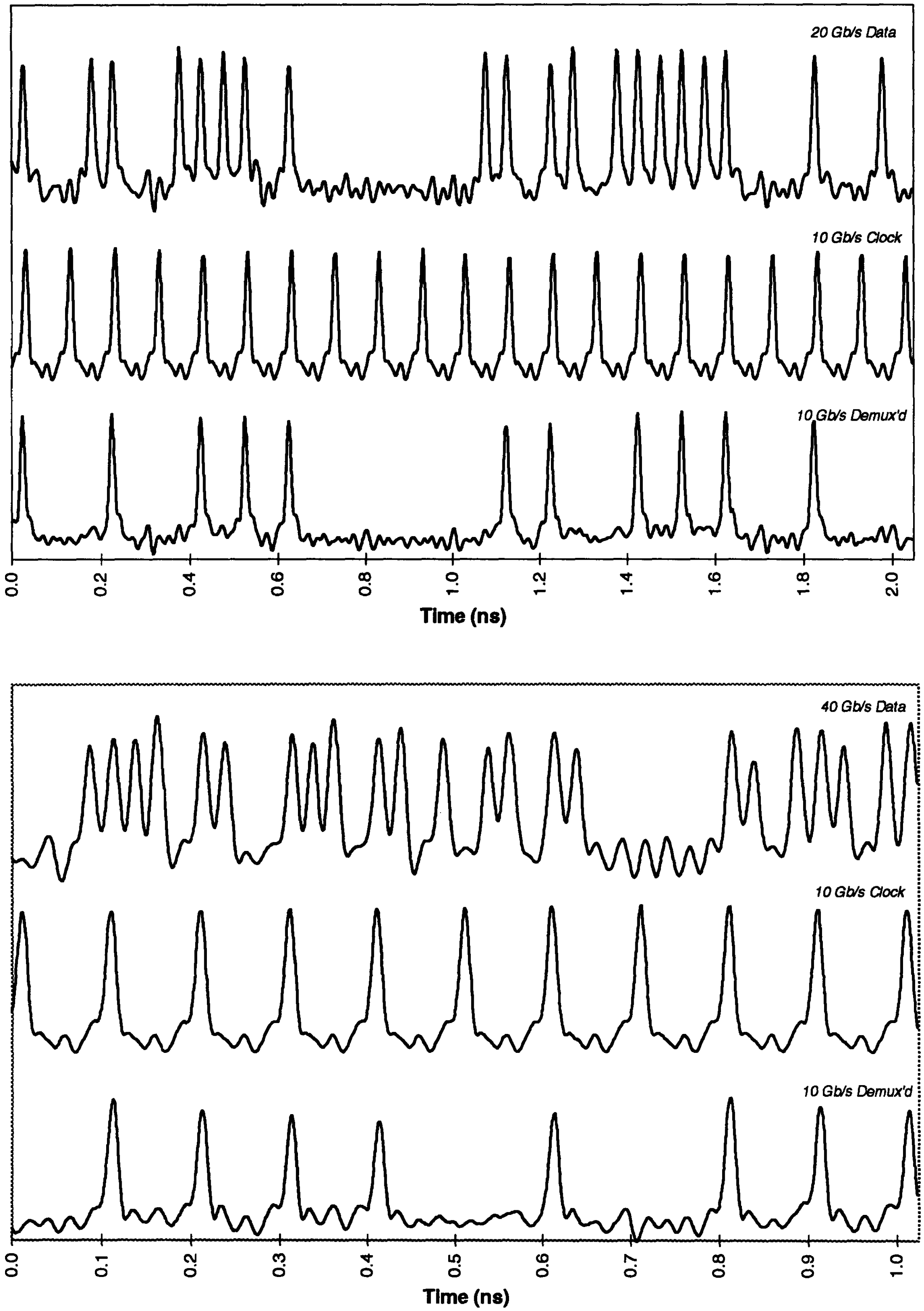

Figure 4.35: ***Demultiplexing Using the UNI with Counter-Propagating Control***

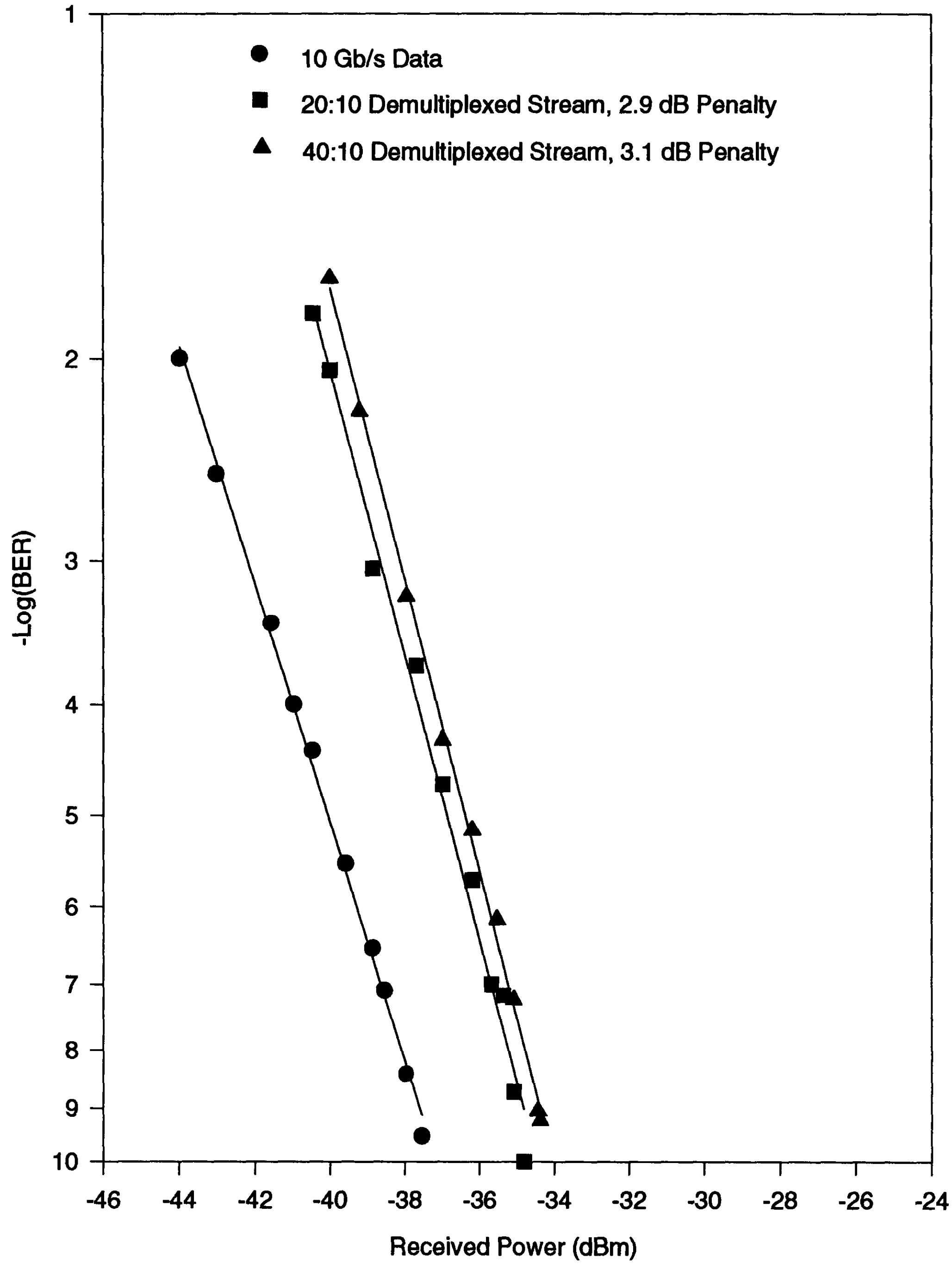

Figure 4.36: ***UNI w/ Counter-Propagating Control Demultiplexer BER***

Inverting operation at 10 Gb/s using the same wavelengths has been demonstrated. As usual, the clock stream enters the signal port of the device, the data stream enters the control port and the UNI is biased ON. In this case, the clock and data average powers entering the SLA were 6 mW and 35 mW respectively. Figure 4.37 shows an oscilloscope trace of inverter operation and Figure 4.38, the BER measurement, shows approximately a 2.9 dB power penalty for inverting operation. Inverter operation at 40 Gb/s is shown in Figure 4.39. The 40 Gb/s clock stream was generated by an SCS and the average signal and control powers were very similar to those in the co-propagating case. Again, we see pattern dependent gain on the input and output streams due to long lived gain recovery. Note that Figure 4.39 also demonstrates non-inverting (top trace) and inverting (bottom trace) wavelength conversion from 1560 nm to 1542 nm. Moreover, since the top trace was obtained by biasing the UNI "OFF" in the absence of the control pulses, it also represents the result of 40 Gb/s bit-wise AND operation.

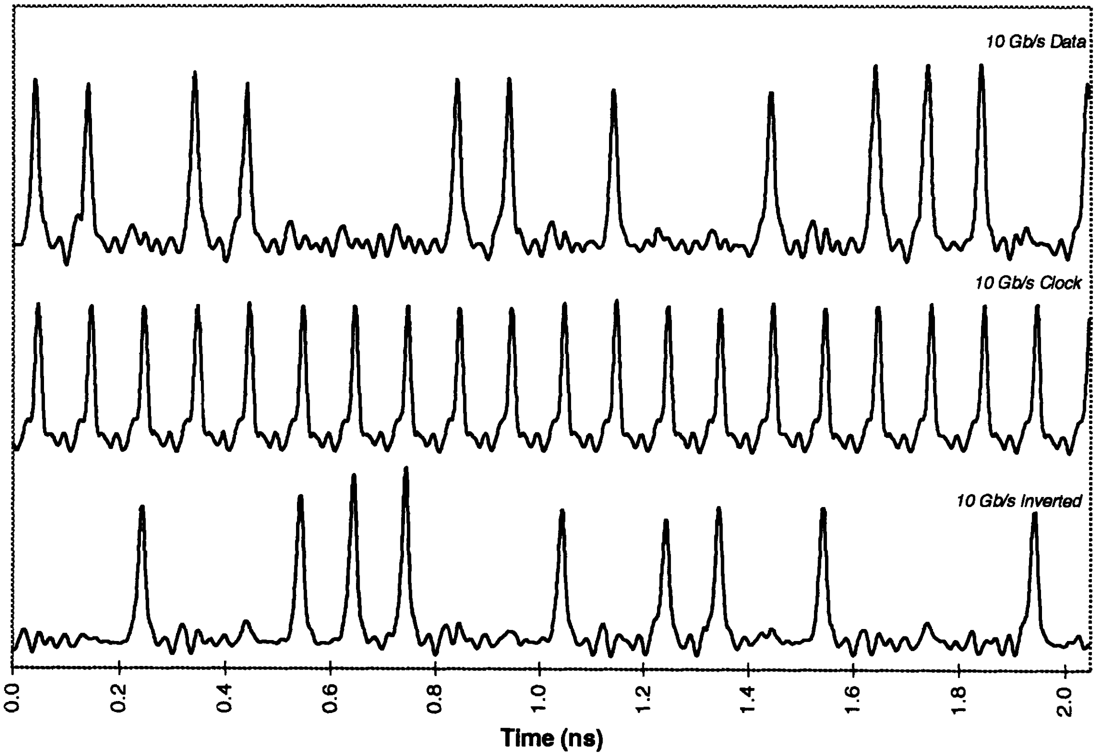

Figure 4.37: *10 Gb/s Inverting Using a UNI with Counter-Propagating Control*

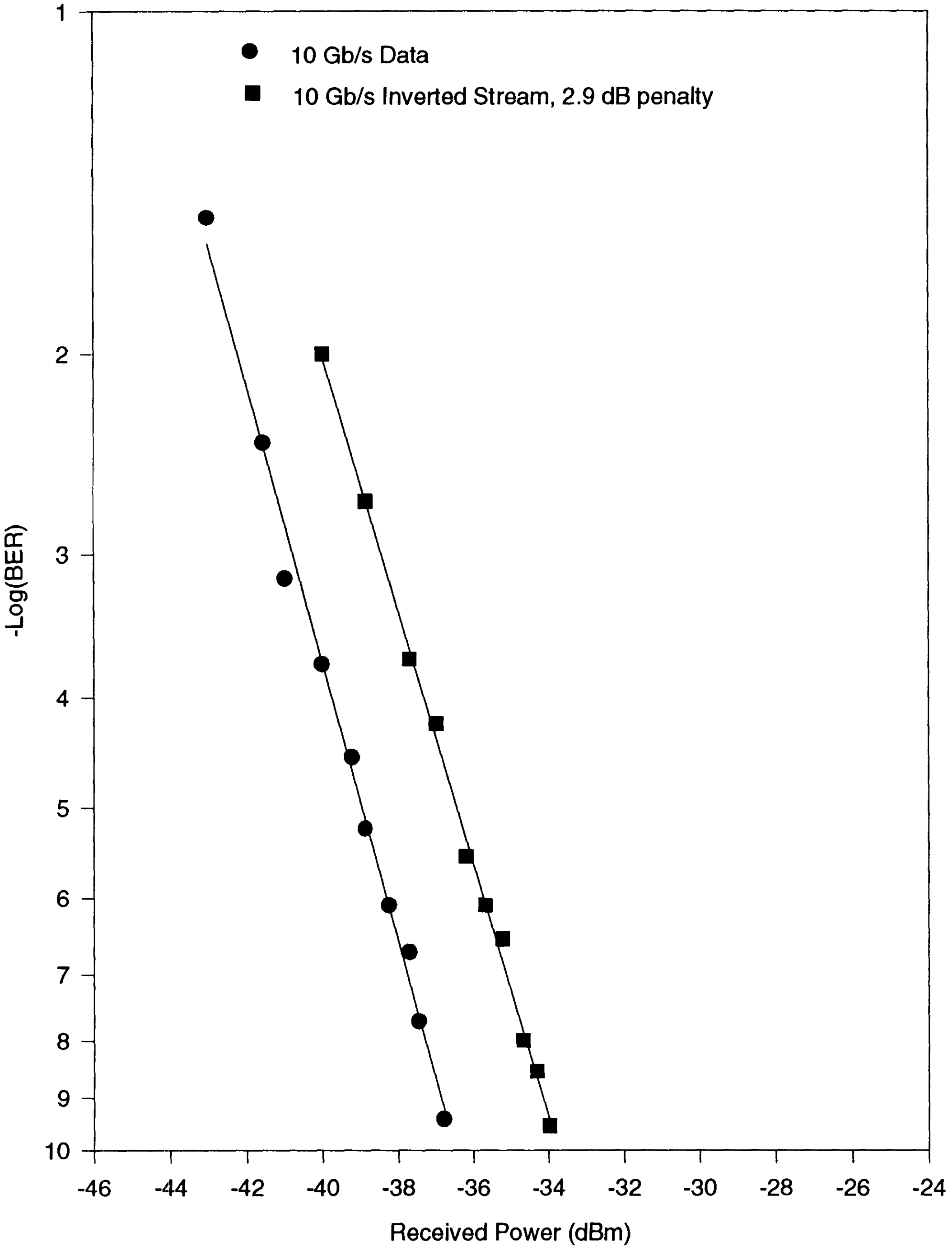

Figure 4.38: *UNI with Counter-Propagating Control Inverter BER*

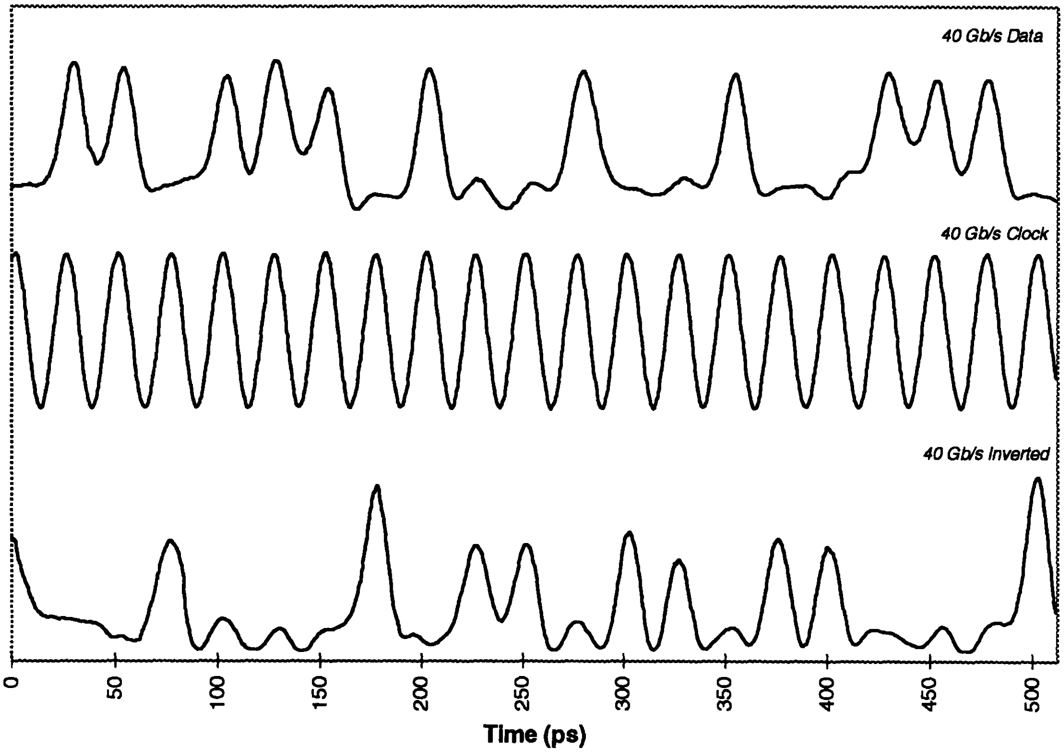

Figure 4.39: ***40 Gb/s Inverting Using a UNI with Counter-Propagating Control***

Recall that by using two control inputs in the UNI geometry, OR and NOR gates can be realized (Figure 2.5). We have performed OR and NOR gating at 10 Gb/s using the UNI / SLA with the counter-propagating control geometry. Note that we can just as easily perform these functions in a co-propagating control geometry since the two geometries are functionally equivalent. The experimental setup is shown in Figure 4.40. The two logical inputs are obtained by splitting the 10 Gb/s electro-optically modulated PRBS along two paths. The variable optical delay in one path is set to an integer multiple of the bit period so as to properly overlap the two streams before entering the control port of the UNI. A 10 Gb/s clock stream enters the signal port. For OR and NOR operation, the UNI is biased OFF and ON respectively. We chose the wavelengths of the clock and logical inputs to be closer to the gain peak of the diode in the expectation that gain nonlinearities would be stronger. As a result, all the input wavelengths are approximately 1545 nm. We are intentionally taking advantage of cross gain saturation for OR and NOR gating in order to be able to turn the clock pulses OFF in the case of NOR gating and to obtain relatively uniform output pulse intensities in the case of OR gating.

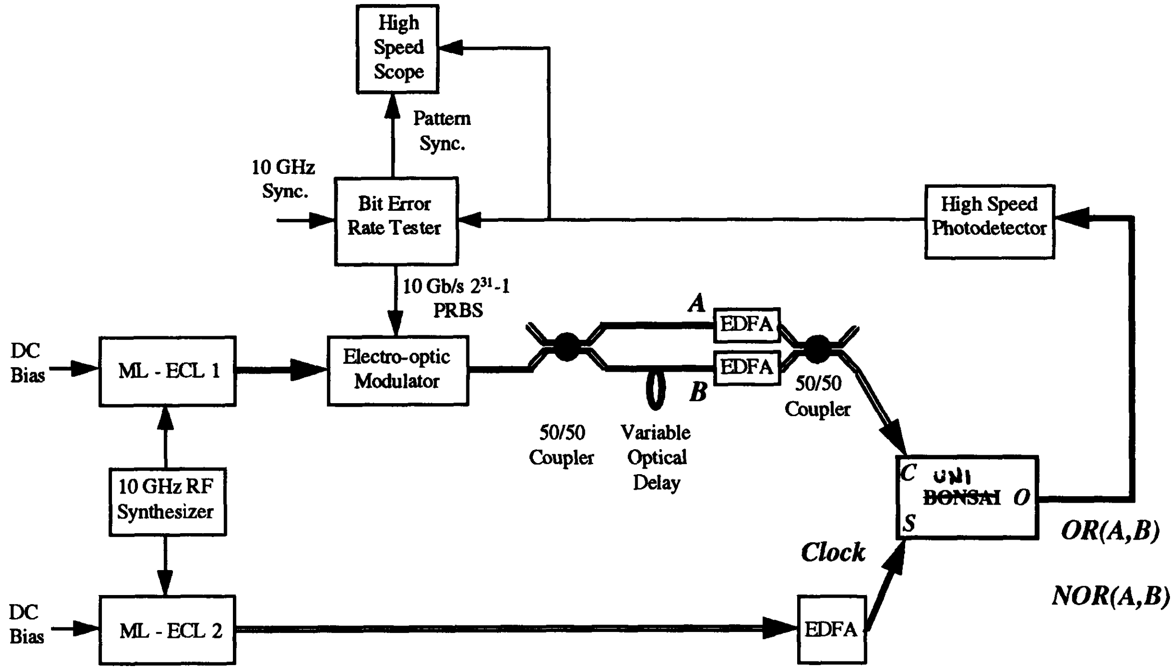

Figure 4.40: ***OR / NOR Gating Experimental Setup***

The clock, A, and B powers were 10 mW, 52 mW, and 48 mW respectively. Figure 4.41 shows a scope trace of OR and NOR operation. The OR and NOR functions could simply be obtained by adjusting primarily the output polarization controller of the UNI. We observe good contrast ratio and relatively uniform pulse heights. It is interesting to note that in the case where A and B are both "1", the output OR'd pulse is slightly higher than the rest of the pulses. This is most likely due to the fact that two temporally coinciding control pulses of similar intensity impart more phase shift to the signal pulse than would one control pulse. In fact, if cross gain saturation was not present, we would expect twice the height in that case. It is conceivable that the amplitude uniformity in the output pulse stream is due to cross gain saturation (XGS) counteracting additional cross phase modulation. More specifically, although a second control pulse imparts more phase shift to the signal pulse, XGS acts to reduce the pulse height. NOR operation is explained more easily since XGS and XPM act in the same direction to turn the signal pulses OFF.

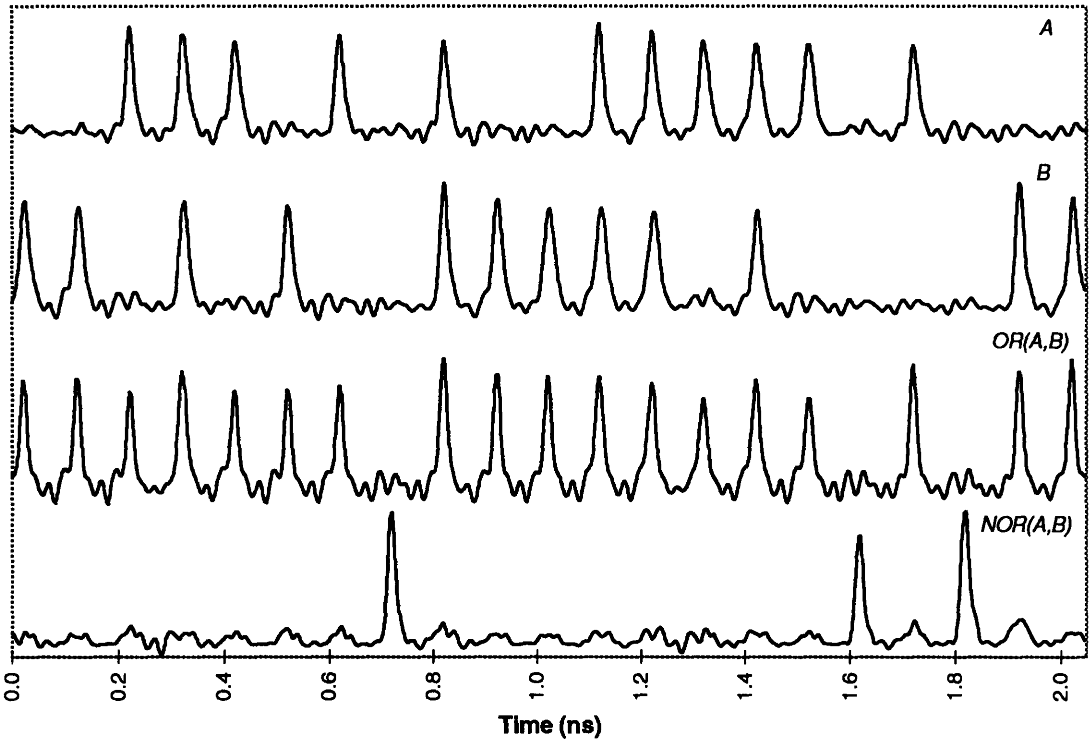

Figure 4.41: ***OR and NOR Gating using a UNI***

Chapter 5: Device Comparisons and Conclusions

5.1 Summary of Results

In this thesis, I have presented a family of switching devices based on the single-arm interferometer geometry. The primary advantage of this geometry is that it circumvents the problem of long-lived refractive index nonlinearities. As a result, it is amenable to semiconductor nonlinearities which allows one to decrease the nonlinear interaction length by 6 to 7 orders of magnitude as compared to fiber. The most important ramification of this length reduction is a commensurate reduction in device propagation delay. In current optical logic, the bit period is typically a small fraction of the device propagation delay (in direct contrast to the electronic logic case). Although these optical switches are easily pipelineable (and are, in fact, almost always operated in this mode), long propagation delays result in added overhead in real systems. For example, an address recognition (AR) module in a 100 Gb/s slotted TDM network may have a propagation delay equivalent to 10,000 to 100,000 bit periods. While the destination address of the packet is being read in this module, the packet itself must be temporarily stored (in a length of fiber for instance) until the AR module decides whether or not to accept the packet. This overhead is extremely cumbersome not only because the predetermined length of fiber must be cut precisely, but also because this delay adds directly to the end to end packet delay. Consequently, the use of semiconductor nonlinearities are attractive due to the possibility of device integration and compactness. It is conceivable that the SAI can be fully integrated into semiconductor by using highly anisotropic (stress induced perhaps) passive waveguides for the PSD. The latter is extremely important from a systems perspective, not only because of the potentially small propagation delay, but also because of the consequent device robustness and manufacturability.

From a functional standpoint, the SAI is a versatile switching device capable of multiple logic functions. We have experimentally demonstrated demultiplexing, AND, OR, NOR, and XOR gating at rates up to 40 Gb/s using different geometries based on the SAI. It is interesting to note that only relatively minor modifications in device geometry were required to achieve this varied functionality. Using a UNI with counter-propagating control, we additionally demonstrated device cascadability, a characteristic critical to the implementation of more complex logic modules suited to header processing, clock recovery, and very simple protocol engines. This varied device functionality coupled with cascadability and ultimately monolithic integration is promising from the perspective of system design because standardized atomic logic units can be interconnected without considerable overhead. Lastly, I should point out that although the SAI-based devices have many advantages, the major disadvantage concerns scaleability of data rate. Namely, since the 2 signal components are effectively polarization and time division multiplexed, the pulse repetition rate in the nonlinear medium is twice (3 or 4 times in the SADINI) that of the incoming data. Consequently, to design a switch operating at a data rate of R requires that the input pulse widths accommodate an intra-switch data rate of 2R (or nR, $2 \le n \le 4$). Therefore, given a pulse source, the SAI-based device may only operate at half the rate of others devices such as the nonlinear optical loop mirror or Mach-Zehnder interferometer.

In section 4.3.1, we demonstrated demultiplexing and inverting using a UNI with a fiber nonlinearity. Although the demultiplexing performance was quite good yielding incurred power penalties less than 3.5 dB, it was necessary to judiciously chose the signal and control wavelengths so that pulse walk-through did not lead to inter-symbol interference. Moreover, due to soliton compression of the control pulse, we found, via autocorrelation measurements, that the output demultiplexed pulse did not significantly resemble the input signal pulse. In the case of inverting operation, we found that a non-optimal logical “0” to “1” contrast ratio led to a 3.8 dB power penalty in the BER measurement. This was attributed to non-uniform phase shifts imparted to the clock pulses even though the input wavelengths were chosen to take advantage of control pulse broadening.

The switching results using a SADINI geometry were presented in section 4.3.2. 20 Gb/s demultiplexing was shown, via the BER measurement, to have approximately the same performance as that of the UNI with a fiber nonlinearity. This indicated that we were successful in interfering out the control pulse as opposed to filtering it at the output. Again, the input wavelengths had to be chosen such as to avoid pulse distortion due to GVD / SPM. We then demonstrated the interesting new logical function - XOR. Although the general operation was correct, the contrast ratio was again not ideal due to non-uniform phase shifts. The observed 6 dB power penalty was easily explained via a simple analysis of the probability of error of a binary PAM signal in WGN. The restrictions on input wavelengths and powers are far more stringent in this case as compared to that of the UNI due to the fact that one must be concerned with the mutual interaction of signal and control. We suggested that with the utilization of shorter pulses, full signal and control walk-through could be achieved leading to more uniform phase shifts. In general, we found, as expected, that the choice of input wavelengths and pulse widths is critical in determining device performance. The latter is somewhat conceptually inelegant from a device perspective.

In section 4.4.1, we demonstrated 40 Gb/s demultiplexing and inverting using a UNI with an SLA for nonlinearity. Demultiplexing operation yielded power penalties commensurate with those obtained using a fiber nonlinearity, suggesting that device performance was not sacrificed by the interaction length reduction. Of more interest, however, was that the device performance was not degraded in spite of long lived refractive index nonlinearities, thus showing the SAI's immunity to these effects. Bit-wise inversion was also demonstrated yielding a 2.9 dB penalty at 10 Gb/s. This should be compared to the 3.8 dB penalty using a fiber nonlinearity. We suggested that cross gain saturation in the SLA helped in non-interferometrically turning the clock pulses OFF. We then demonstrated 40 Gb/s bit-wise inverting using a soliton compression source as the 40 Gb/s clock. Correct operation was observed, although output pulse amplitude modulation was evident due to long lived gain dynamics in the SLA. Setting the signal and control wavelength close or below the band edge should increase the linewidth enhancement factor, thereby reducing the effects of gain saturation. As compared to the UNI with a fiber nonlinearity, the UNI with SLA is more versatile from a device perspective due to its relative input wavelength insensitivity. More specifically, the device performance does not vary significantly as long as the signal and control wavelengths are far above the gain peak of the SLA.

The switching results for the UNI with counter-propagating control were shown in section 4.4.2. The theory in section 3.2.3 predicted that, as long as the SLA length was comparable to pulse widths in the spatial domain, the switching characteristics of the co and counter-propagating results should be similar. Indeed, we empirically verified this for demultiplexing and inverting. The incurred power penalties were no worse that in the co-propagating case. The latter was not only intuitively appealing but also a nice result in that device cascadability was gained with no expense in performance. Moreover, it allowed us to reduce the number of components in the setup by obviating the need for an output filter. We also demonstrated an OR and NOR gate by using cross gain saturation in addition to cross phase modulation in the SLA. We observed very good contrast ratio and uniform output pulse amplitudes. As a final note, the 40 Gb/s AND and NOT gating results obtained from the UNI with co and counter-propagating control also demonstrates wavelength conversion.

5.2 Other Devices of Recent Interest

In this section, I will briefly describe different high speed optical switching devices and their switching performance measures as compared to the SAI based devices developed in this thesis. I will discuss a class of devices based on the nonlinear optical loop mirror (NOLM) using a fiber and semiconductor nonlinearity, recent developments in balanced integrated Mach Zehnder devices, and four wave mixing (FWM) in fiber and semiconductor.

Interferometric device geometries are, by far, the most prevalent and researched class of optical switches. Some of the first demonstrations in optical switching were conducted by Haus et. al.[57], and Lattes et. al.[58], using an integrated Mach-Zehnder (MZ) interferometer. A clock stream entered the device and was split into two components that traveled along distinct paths and were interferometrically recombined at the output. The 2 logical inputs were coupled into the two arms and were used to gate the clock stream. Varying functionality was obtained by appropriate biasing of each arm. As an application, a pseudo-random bit stream generator based on an XOR gate with feedback was demonstrated. The bit rate of the device is intrinsically limited, however, by long lived refractive index and gain modulation in the semiconductor. A recent development circumvented this problem by using judiciously placed nonlinear elements in each arm and a counter-propagating control stream[59]. It should be pointed out that Mach-Zehnder devices have the tremendous advantage of monolithic integrability, which most high speed optical switches have still not achieved. As compared to the SAI geometry, the balanced MZ devices are less elegant due to the fact that the placement of the nonlinear materials is critical in determining the switching window and is also dependent on the intended data rate of the device. The SAI, on the other hand, is self balancing independent of data rate. Moreover, in contrast to the SAI-based devices, the MZ geometry is prone to interferometric misalignment since the 2 signal components traverse separate paths.

An interferometric geometry that has attracted a vast research effort is the nonlinear optical loop mirror (NOLM)[60] in which a signal pulse is split via a fiber coupler into two counter-propagating components that traverse a loop and interfere back at the coupler. A control pulse, coupled in via an additional fiber coupler, co-propagates with one signal component. A nonlinear optical element is present at some point in the loop in which the signal component co-propagating with the control experiences a phase-shift via cross-phase modulation. A major advantage of the NOLM over the MZ geometry is improved stability because both signal components travel along the same path, although in opposite directions. One problem associated with the NOLM, however, is that the polarization bias is pattern dependent due to accumulated cross-phase modulation imparted to the counter-propagating signal pulse component by the control pulse stream. This pattern dependent polarization bias / phase modulation translates into a pattern dependent amplitude modulation on the output pulse. In the case of the SAI, both signal components are co-propagating, and thus it is not subject to this effect.

Many switching demonstrations using the NOLM with a fiber nonlinearity have been performed. Demultiplexing at aggregate rates of 200 Gb/s has been demonstrated[61]. Wavelength converters[62], bit phase comparators[63], optical sampling[64], and XOR gating[65], to mention a few, have also been demonstrated. Due to the long lengths of fiber in these devices, the NOLM is particularly sensitive to acoustic perturbation. Namely, the interferometer bias is transiently modulated by a traveling acoustic wave. The SAI, however, is immune to these effects because both signal components traverse the same path. Moreover, the SAI can be used to perform all the functions described above. This fact is actually not surprising in light of the fact that the NOLM and SAI are topologically equivalent devices.

The use of semiconductor nonlinearities in the NOLM is very popular now. By placing the nonlinear material off center in the loop, the switching window can be customized as a function of the desired data rate. As such, long-lived nonlinearities do not affect the achievable aggregate data rates. In fact, 160 Gb/s demultiplexing using an SLA in a NOLM has been performed[66]. However, the frame rates (control repetition rates) in the demonstrations thus far have not exceeded 10 Gb/s. Consequently, functionality other than demultiplexing has not been demonstrated. Although the SAI clearly is susceptible to long-lived gain nonlinearities, we still have been able to perform bit-wise inversion at 40 Gb/s employing both a high speed signal and control stream.

Although interferometric switches are prevalent, there have been demonstrations of switching using nonlinear parametric processes. Conceptually, an AND or demultiplexing operation is equivalent to a correlation operation between the two inputs since one desires an output only in the presence of both inputs. Second harmonic generation and sum /

difference frequency generation are the lowest order parametric processes that accomplish a correlation operation. In fact, these second order nonlinearities are used commonly in laboratories in short pulse autocorrelators. Recently, sum frequency generation in a crystal was used in a high resolution optical sampling oscilloscope / real time correlator[67]. Third order parametric processes such as four wave mixing (FWM) in fiber and semiconductor have been used in demultiplexing experiments at rates up to 200 Gb/s[68], and very recently, 400 Gb/s[69]. The primary advantage of FWM based DEMUX is device simplicity since the only essential element is the nonlinear material which could be ~ 1mm in length in the case of a semiconductor nonlinearity. Unfortunately, the FWM conversion efficiency is quite small (~ 1%) and thus requires very high pump powers to obtain output powers sufficient to saturate EDFA's. Moreover, FWM admits only one function, as opposed to interferometric devices which have a few degrees of freedom in terms of biasing conditions.

One can also use cross gain saturation in a semiconductor laser amplifier to perform an inverter operation. More specifically, an appropriately timed clock stream and data stream entering a nonlinear gain element interact via cross gain saturation. In the presence of an intense data pulse, the clock pulse experiences a reduction in gain and becomes a "0" at the output. In the absence of a data pulse the clock pulse sees the unperturbed gain and remains a "1" at the output. The achievable bit rate of such a scheme is severely limited, however, by long lived gain relaxation in the nonlinear element. As such, the bit rate cannot exceed the slowest gain relaxation rate. To reduce to upper state lifetime and therefore the gain relaxation time, the introduction of an out of band CW signal (a "holding beam") coupled into the SLA can be employed to increase the rate of stimulated emission from the upper state. Using this technique, 40 Gb/s inverting wavelength conversion has been achieved[70]. As in the FWM case however, simplicity and reliability is an advantage. Similar devices based on nonlinear polarization rotation in an SLA employ gain and refractive index anisotropies to perform demultiplexing[71]. Again, these geometries are intrinsically unbalanced and thus are limited in bit rate.

5.3 Ongoing and Future Work

5.3.1 Simplified Device Implementations

Although all the results up to 40 Gb/s in this thesis were obtained using the implementations described in section 4.4., we have built a simplified "black box" version of the UNI for use in future system experiments. We realized that the number of polarization controllers in the previous implementation represented a considerable complexity problem, especially in comparison to other switching devices of recent interest (notably those based on the nonlinear optical loop mirror geometry). Consequently, we streamlined the design such that only 2 polarization controllers were required in the UNI. Figure 5.1 shows the new implementation of the UNI with counter-propagating control. PC 1 is used to bias the interferometer, while PC 2 is used as a function selector (AND or INVERT). A PM fiber-pigtailed polarization sensitive isolator (PSI) is placed at the signal input to which is spliced the 7.5 m length of BRF such that the slow and fast axes of the BRF are at 45° with respect to one of the axes of the PM fiber. The latter allows us to get rid of 1 polarization controller at the input of the device. Moreover, the PSI translates input polarization fluctuations (which are presumably small) to output amplitude fluctuations. Consequently, the UNI bias is highly stable and independent of variations outside the device, allowing us to treat it as somewhat of a black box, once the polarization controllers have been set. We also found that PC 1 can be used to align the polarization before the BRF in the second PSD, thus allowing us to remove an additional polarization controller. We have experimentally found that the resulting device is highly reliable and can be used in system experiments. Indeed, we have demonstrated stable demultiplexer and inverter operation both at 40 Gb/s using the simplified version and have detected no fundamental differences in the device performance as compared to the more complex previous implementation.

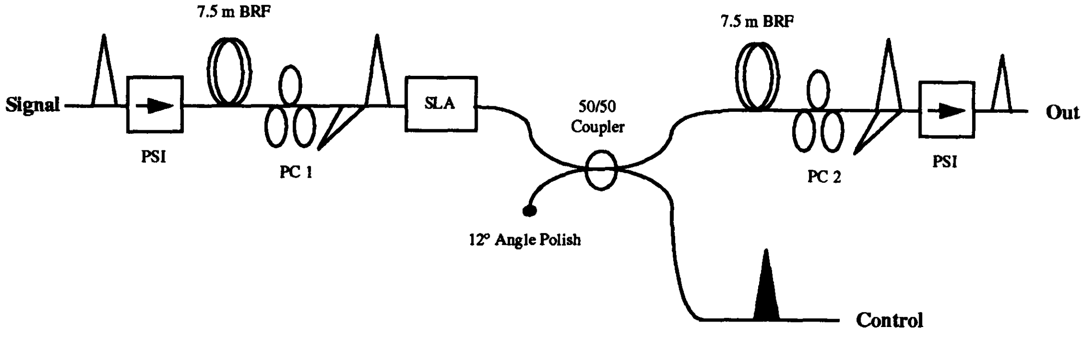

Figure 5.1: ***Simplified Implementation of UNI w/ Counter-Propagating Control***

5.3.2 Future Work

Since other devices, such as the NOLM, have been used to perform demultiplexing at rates up to 200 Gb/s, an important avenue for future work would be in scaling the achievable data rate of the UNI. In addition, more emphasis on using a semiconductor as opposed to a fiber nonlinearity would be prudent given the results and conclusions in section 5.1. Of all the functions demonstrated using a UNI / SLA, high rate demultiplexing is the most likely to work because the SLA gain is perturbed on time scales commensurate with the demultiplexer frame rate, despite the high repetition aggregate data stream.

Now that planar lightwave integrated Mach-Zehnder multiplexers (actually interleavers that rate convert one pseudo-random stream into a higher rate pseudo-random stream) are commercially available, multiplexing of 10 Gb/s stream to aggregate streams at 160 Gb/s is practical. However, the major obstacle then becomes finding a suitable high repetition rate short pulse source. For example, 160 Gb/s demultiplexing using the UNI would require 1 ps pulses. Although linear and soliton compression schemes can be used to compress mode-locked pulses to the required widths, the resulting pulses are either slightly nonlinearly chirped (as is the case in linear compression) or noisy with pedestals (soliton compression). Moreover, stability is a very important consideration because in system experiments one would like to be able to treat individual devices as black boxes. Towards this end, Kawanishi, et. al., have developed a short pulse source utilizing a mode-locked fiber ring laser in conjunction with super-continuum generation, capable of producing sub-picosecond pulses at a repetition rate of 6.25 GHz and tunable over a 200 nm range[72,73]. Active cavity length stabilization is achieved by minimizing relaxation oscillations using a simple feedback circuit[74]. Another difficulty concerns diagnostics. Current commercial electronic sampling oscilloscopes do not have the bandwidths sufficient to track 100 Gb/s streams. Moreover, photodetectors with the required bandwidths are not commercially available (although they do exist in some research laboratories). Consequently, one must adopt an optical sampling technique to display traces of 100 Gb/s bit streams. Takara, et. al., have developed such a system with a temporal resolution of 0.45 ps based on sum frequency generation in KTP[75].

Ironically, perhaps the easiest modification of the experimental setup is to the UNI itself. To extend the data rate to 160 Gb/s, for example, would only require changing the PSD to accommodate a 3.125 ps delay, corresponding to a BRF length of 1.9 m. It should be noted however, that a co-propagating control scenario would be the more likely geometry to use. The reason for the latter concerns the relationship between the pulse widths and the SLA interaction length. For example, 1 ps pulses are spatially smaller than the 1 mm length SLA. As a result, a counter-propagating control would begin to interact with more than one signal pulse leading to a degradation in the switching performance. If the cascadability of the counter-propagating scheme is absolutely essential, the SLA length must be decreased in proportion to the pulse widths.

Extending the data rates of the logic functions is also important, partly because not many results at rates above 40 Gb/s have been obtained thus far in this area. Of particular importance is the use of semiconductor nonlinearities to perform high speed logic.

However, for this to be ultimately fruitful from a device or system perspective, much is still to be learned about the physics of gain nonlinearities and how they affect the device performance. As alluded to in section 3.2, high repetition pump probe studies are required to investigate the effects of carrier density (and thus bias current), wavelength, and average optical power on the recovery times of relevant nonlinearities. It is interesting to note that, in a sense, this brings us full circle to the single-arm interferometer as a tool for probing refractive index nonlinearities[76].

An exciting and challenging prospect is device integration. Indeed, this area is vast and could easily be the subject of many a Ph.D. thesis. It is, however, conceivable that the fiber implementations of the devices in this thesis, could be replaced by integrated versions employing passive and active waveguides for the PSD and nonlinearity respectively. The PSD's could be replaced by highly strained anisotropic InGaAs passive waveguides. Moreover, it may be possible to adjust the linear phase bias of the interferometer with the utilization of an electro-optic material - potentially even the InGaAs waveguides themselves. Even though all of this is very speculative, is it appealing to entertain the thought of an array of such integrated and standardized logic units whose function can be dynamically programmed (i.e. the interferometer bias can be adjusted) by applying a certain voltage to the device. Clearly, there is considerable room for innovation.

APPENDIX

A.1 Simulation Code

```
SCREEN 2

DEFDBL A-Z

DIM phasec(10, 200)
DIM phases(10, 200)
DIM siginm(10, 200)
DIM coninm(10, 200)
DIM sigoutm(10, 200)
DIM conoutm(10, 200)
DIM swrsigm(10)
DIM swrconm(10)

REM DEFINE CONSTANTS

pi = 3.1415926#
c = 3E+08

REM DEFINE FIBER PARAMETERS

n2 = 3.2E-20
a = 5E-11
alpha = 5.7564E-05
L = 8.8
l0 = 1.547E-06
s0 = .067

REM ------------------------------------------------------------------------

N = 0

REM BEGINNING OF OUTER LOOP

5

REM DEFINE SIGNAL AND CONTROL WAVELENGTHS

ls = 1.5602E-06
lc = 1.547E-06

REM DEFINE FIBER DISPERSION CHARACTERSITICS

DEF fnq (lambda) = lambda ^ 2 / (2 * pi * 300000!)
DEF fnb2 (lambda) = -fnq(lambda) * .25 * s0 * lambda * (1 - (l0 * 1E+09 / lambda) ^ 4)
DEF fnb3 (lambda) = (fnq(lambda)) ^ 2 * .25 * s0 * (3 + (l0 * 1E+09 / lambda) ^ 4)

REM ALL DISPERSION PARAMETERS IN PS^N/KM

k1 = (1.445 / c) * 1E+15
k2s = fnb2(ls * 1E+09)
k2c = fnb2(lc * 1E+09)
k20 = 0
k3s = fnb3(ls * 1E+09)
k3c = fnb3(lc * 1E+09)
k30 = fnb3(l0 * 1E+09)

REM DEFINE FREQUENCIES

w0 = 1E-12 * 2 * pi * c / l0: ws = 1E-12 * 2 * pi * c / ls: wc = 1E-12 * 2 * pi * c / lc
```

```
REM COMPUTE VELOCITIES AND WALK-OFF

vsi = k1 + .5 * k30 * (ws - w0) ^ 2 + (k40 / 6) * (ws - w0) ^ 3
vci = k1 + .5 * k30 * (wc - w0) ^ 2 + (k40 / 6) * (wc - w0) ^ 3

vs = 1E+15 / vsi: vc = 1E+15 / vci
v = vs - vc

sigma = L * (vci - vsi)

REM PRINT VELOCITIES TO SCREEN

REM PRINT "signal  velocity= "; vs; "m/s"
REM PRINT "control velocity= "; vc; "m/s"
REM PRINT "velocity difference= "; -v; "m/s"
REM PRINT "walk through= "; -sigma; "ps"

REM ASK FOR INPUT PARAMETERS

REM INPUT "peak power of signal: "; ppowers
REM INPUT "peak power of control: "; ppowerc
REM INPUT "initial signal pulse FWHM: "; tau0s
REM INPUT "initial control pulse FWHM: "; tau0c
REM INPUT "initial pulse separation: "; t0

ppowers = .33333
ppowerc = .33333
tau0s = 25
tau0c = 25
t0 = 20 * (N - 5)

REM RENORMALIZING PARAMETERS

t0 = t0 * 1E-12
tau0s = tau0s * 1E-12 / (2 * SQR(LOG(2)))
k2s = k2s * 1E-27
gs = (2 * pi / ls) * n2 * (ppowers / a)
tau0c = tau0c * 1E-12 / (2 * SQR(LOG(2)))
k2c = k2c * 1E-27
gc = (2 * pi / lc) * n2 * (ppowerc / a)

REM DEFINE INPUT PULSE ENERGIES

eci = SQR(pi) * ppowerc * tau0c
esi = SQR(pi) * ppowers * tau0s

REM DEFINE PULSE EVOLUTION EQUATIONS

DEF fnzs (t) = vs * t
DEF fnzc (t) = vc * (t - t0)
DEF fngammas (t) = vs * tau0s * SQR((1 + (k2s * gs * vs ^ 2 * t ^ 2 / tau0s ^ 2)) ^ 2 + (k2s * vs * t / tau0s ^ 2) ^ 2)
DEF fngammac (t) = vc * tau0c * SQR((1 + (k2c * gc * vc ^ 2 * t ^ 2 / tau0c ^ 2)) ^ 2 + (k2c * vc * t / tau0c ^ 2) ^ 2)
DEF fnicp (t) = (ppowerc / a) * vc * tau0c / fngammac(t)
DEF fnisp (t) = (ppowers / a) * vs * tau0s / fngammas(t)
DEF fnic (z, t) = fnicp(t) * EXP(-((z - fnzc(t)) / fngammac(t)) ^ 2) * EXP(-alpha * z)
DEF fnis (z, t) = fnisp(t) * EXP(-((z - fnzs(t)) / fngammas(t)) ^ 2) * EXP(-alpha * z)

gc0 = (2 * pi / lc) * n2
gs0 = (2 * pi / ls) * n2

dt = .000001

CLS

REM MAIN LOOP

FOR t = 0 TO 1000 * L / vs STEP dt

  CLS
```

```
  LOCATE 1, 1: PRINT t

  FOR zp = -.005 TO .005 STEP .0001
   PSET (320 + 20000 * zp, 199 - 1E-08 * fnis(zp + fnzs(t), t))
   PSET (320 - 20000 * (fnzs(t) - fnzc(t)) + 20000 * zp, 199 - 1E-08 * fnic(zp + fnzc(t), t))
  NEXT zp

  FOR zp = -.01 TO .01 STEP .0001
   phases(N, 100 + 10000 * zp) = phases(N, 100 + 10000 * zp) + gs0 * vs * dt * fnic(zp + fnzs(t), t)
   phasec(N, 100 + 10000 * zp) = phasec(N, 100 + 10000 * zp) + gc0 * vc * dt * fnis(zp + fnzc(t), t)
  NEXT zp

NEXT t

REM FILL OUTPUT PULSE BEFORE POLARIZER MATRIX

  tausf = (1 / vs) * fngammas(1000 * L / vs)
  taucf = (1 / vc) * fngammac(1000 * L / vc)
  icpf = fnicp(1000 * L / vc) * EXP(-alpha * 1000 * L)
  ispf = fnisp(1000 * L / vs) * EXP(-alpha * 1000 * L)
  DEF fnsig (t) = EXP(-(t / tausf) ^ 2)
  DEF fncon (t) = EXP(-(t / taucf) ^ 2)

  FOR j = 0 TO 200
   zp = .0001 * (j - 100)
   ts = (zp / vs) * 1E+12
   tc = (zp / vc) * 1E+12
   sig = fnsig(ts * 1E-12)
   con = fncon(tc * 1E-12)
   siginm(N, j) = sig
   coninm(N, j) = con
  NEXT j

REM FILL IN OUTPUT PULSE SHAPE MATRIX

  phibs = 0
  phibc = 0
  esout = 0
  ecout = 0
  esin = 0
  ecin = 0

  FOR j = 0 TO 200
   zp = .0001 * (j - 100)
   ts = (zp / vs)
   tc = (zp / vc)
   dzp = .0001
   dts = dzp / vs
   dtc = dzp / vc
   esin = esin + dts * fnsig(ts)
   ecin = ecin + dtc * fncon(tc)
   sigout = fnsig(ts) * (COS((phases(N, j) + phibs) / 2)) ^ 2
   conout = fncon(tc) * (COS((phasec(N, j) + phibc) / 2)) ^ 2
   esout = esout + dts * sigout
   ecout = ecout + dtc * conout
   tsp = ts * 1E+12
   tcp = tc * 1E+12
   sigoutm(N, j) = sigout
   conoutm(N, j) = conout
  NEXT j

REM FILL OUTPUT PULSE ENERGY RATIO MATRIX

  esr = esout / esin
  ecr = ecout / ecin
  swrsigm(N) = esr
  swrconm(N) = ecr

IF N = 10 THEN GOTO 100
```

```
N = N + 1
GOTO 5

REM ---------------------------------------------------------------------------

100 REM WRITE DATA TO OUTPUT FILE

  OPEN "SIGIN.DAT" FOR OUTPUT AS #1
  OPEN "CONIN.DAT" FOR OUTPUT AS #2
  OPEN "PHASES.DAT" FOR OUTPUT AS #3
  OPEN "PHASEC.DAT" FOR OUTPUT AS #4
  OPEN "SIGOUT.DAT" FOR OUTPUT AS #5
  OPEN "CONOUT.DAT" FOR OUTPUT AS #6
  OPEN "CHRPSIG.DAT" FOR OUTPUT AS #7
  OPEN "CHRPCON.DAT" FOR OUTPUT AS #8

  FOR j = 0 TO 200

   zp = .0001 * (j - 100)
   ts = (zp / vs) * 1E+12
   tc = (zp / vc) * 1E+12

   dzp = .0001
   dts = dzp / vs
   dtc = dzp / vc

   PRINT #1, ts; ",";
   PRINT #2, tc; ",";
   PRINT #3, ts; ",";
   PRINT #4, tc; ",";
   PRINT #5, ts; ",";
   PRINT #6, tc; ",";
   IF j < 200 THEN PRINT #7, ts; ",";
   IF j < 200 THEN PRINT #8, tc; ",";

  FOR N = 0 TO 10

   IF j < 200 THEN chirps = (phases(N, j + 1) - phases(N, j)) / dts
   IF j < 200 THEN chirpc = (phasec(N, j + 1) - phasec(N, j)) / dtc

   PRINT #1, siginm(N, j); ",";
   PRINT #2, coninm(N, j); ",";
   PRINT #3, phases(N, j); ",";
   PRINT #4, phasec(N, j); ",";
   PRINT #5, sigoutm(N, j); ",";
   PRINT #6, conoutm(N, j); ",";
   IF j < 200 THEN PRINT #7, chirps; ",";
   IF j < 200 THEN PRINT #8, chirpc; ",";

   NEXT N

    PRINT #1,
    PRINT #2,
    PRINT #3,
    PRINT #4,
    PRINT #5,
    PRINT #6,
    IF j < 200 THEN PRINT #7,
    IF j < 200 THEN PRINT #8,

  NEXT j
  OPEN "SWRATIO.DAT" FOR OUTPUT AS #9
   FOR N = 0 TO 10
   t0 = 20 * (N - 5)
   PRINT #9, t0; ","; swrsigm(N); ","; swrconm(N)
   NEXT N
CLOSE
END
```

A.2 Feedback Stabilization Circuit

The first implementation of the SADINI we built was, in fact, composed of bulk optical elements. Slow thermal fluctuations in the table caused interferometer bias drifts. Consequently, we designed a feedback stabilization circuit that could simultaneously stabilize both arms of the SADINI. Although we found that the fiber implementations of the UNI and SADINI were very stable and thus did not require active stabilization, a switching device based on the UNI or SADINI as part of a larger system would most likely require bias stabilization. We have found empirically, that the fiber implementations are immune to acoustic perturbations and that stabilization schemes which track thermal variations on long time scales (1 to 10 seconds) would be sufficient to ensure stable operation.

Figure A.1 is a block diagram of the feedback circuit in which ***bold and italicized*** objects are in the optical domain. The bias of the interferometer can be dynamically adjusted in a few ways. For the fiber implementation, an electronically controlled polarization controller (EC-PC) for each arm is the most appropriate since it does not require any additional mechanical components. Namely, the feedback signal can simply drive the polarization controller responsible for the interferometer bias. The circuit works by "tagging" each optical input with a low frequency dither signal at 200 Hz and 300 Hz respectively via the EC-PC's. The two arms can be simultaneously stabilized because the "tag" for each is distinguishable. When the interferometer is biased appropriately, the second harmonic of the input dither is maximized at the output because we are operating at a null or maxima in the interferometer transfer function. In addition, the amplitude of the fundamental of the dither signal is zero (which can be verified by Fourier transforming the output signal). Thus, we design a circuit that simply minimizes the fundamental of the dither signal. The latter can be accomplished by band pass filtering the output signal around the corresponding dither frequency, mixing the filtered signal with a reference dither signal and using the resulting DC component as the error signal. A phase compensator is required to ensure that the reference signal and the received signal are in phase at the multiplier / mixer. The feedback loop is closed with an integrator (1/s). The resulting signal is then amplified in a variable gain stage and is added to the small dither signal. This signal then drives the EC-PC's in the SADINI. The variable gain stage determines the location of the poles of the system function and should be empirically set such that all the poles are in the left half plane. The latter maximized the lock-in bandwidth without causing feedback instability. For the circuits we built, the lock-in bandwidths are on the order of a few Hz. Note that the two dither signals should not be harmonically related to avoid cross-talk between the two halves of the circuit. Since the dither signal is a low frequency and small amplitude signal, the effect of the feedback circuit is negligible on the output stream. The latter can be verified by looking at the RF spectrum of the SADINI output under normal switching operation. Lastly, in the case of the UNI, only 1 half of the circuit is required since the control arm is unbiased.

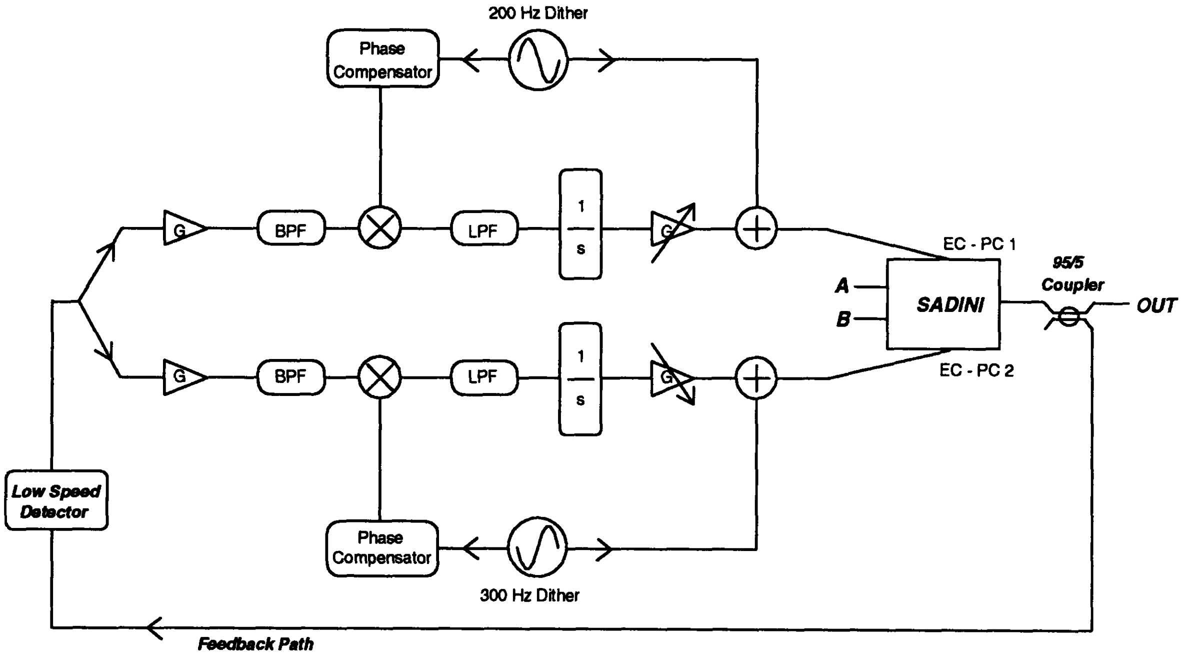

Figure A.1: ***Feedback Stabilization Circuit***

References

---

1. H. Onaka, H. Miyata, G. Ishikawa, K. Otsuka, H. Ooi, Y. Kai, S. Kinoshita, M. Seino, H. Nishimoto, T. Chikama, "1.1 Tb/s WDM Transmission over a 150 km 1.3 um Zero-Dispersion Single-Mode Fiber", *OFC '96 post-deadline paper.*

2. A.H. Gnauck, R.W. Tkach, F. Forghieri, R.M. Derosier, A.R. McCormick, A.R. Chraplyvy, J.L. Zyskind, J.W. Sulhoff, A.J. Lucero, Y. Sun, R.M. Jopson, "One Terabit/s Transmission Experiment", *OFC '96 post-deadline paper.*

3. T. Morioka, H. Takara, S. Kawanishi, O. Kamatani, K. Takigucki, K. Uchiyama, M. Saruwatari, H. Takahashi, M. Yamada, T. Kanamori, H. Ono, "100 Gb/s x 10 Channel OTDM / WDM Transmission Experiment Using a Single Supercontinuum WDM Source", *OFC '96 post-deadline paper.*

4. R.A. Barry, V.W.S. Chan, K.L. Hall, E.S. Kintzer, J.D. Moores, K.A. Rauschenbach, E.A. Swanson, L.E. Adams, C.R. Doerr, S.G. Finn, H.A. Haus, E.P. Ippen, W.S. Wong, *JSAC / JLT Special Issue on Optical Networks*, (1995).

5. R.A. Barry, V.W.S. Chan, K.L. Hall, E.S. Kintzer, J.D. Moores, K.A. Rauschenbach, E.A. Swanson, L.E. Adams, C.R. Doerr, S.G. Finn, H.A. Haus, E.P. Ippen, W.S. Wong, *JSAC / JLT Special Issue on Optical Networks*, (1995).

6. R.A. Barry, *Viewgraph*

7. K.K. Anderson, M.J. LaGasse, C.A. Wang, and J.G. Fujimoto, "Femtosecond dynamics of the nonlinear index near the band edge in AlGaAs waveguides", *Appl. Phys. Lett.*, **56**, p. 1834, (1990).

8. M.J. LaGasse, K.K. Anderson, C.A. Wang, H.A. Haus, and J.G. Fujimoto, "Femtosecond measurements of the nonresonant nonlinear index in AlGaAs", *Appl. Phys. Lett.,* **56**, p. 417, (1990).

9. C. de Chamon, C.K. Sun, H.A. Haus, and J.G. Fujimoto, "Femtosecond time division interferometry technique for measuring the tensor components of $\chi^{(3)}$", *Appl. Phys. Lett.,* **60**, p. 533, (1992).

10. K. Bergman, C.R. Doerr, H.A. Haus, and M. Shirasaki, "Sub-shot-noise measurement with fiber-squeezed optical pulses", *Optics Letters,* p. 643, (October 1992).

11. N.S. Patel, K.A. Rauschenbach, K.L. Hall, "40 Gb/s Demultiplexing Using an Ultrafast Nonlinear Interferometer (UNI)", *Submitted to Photon. Tech. Lett.*

12. N.S. Patel, K.A. Rauschenbach, K.L. Hall, "All-Optical Demultiplexer / Inverter Using a Semiconductor Laser Amplifier in a Single-Arm Interferometer", *CLEO '96 Paper.*

13. N.S. Patel, K.L. Hall, K.A. Rauschenbach, "40 Gb/s Cascadable All-Optical Logic Using an Ultrafast Nonlinear Interferometer (UNI)", *Submitted to Opt. Lett.*

14. N.S. Patel, K.L. Hall, K.A. Rauschenbach, "40 Gb/s Cascadable All-Optical Logic Using an Ultrafast Nonlinear Interferometer (UNI)", *OFC '96 Post-deadline Paper.*

15. M. Shirasaki, H.A. Haus, and D. Liu Wong, "Nonlinear fiber interferometer and logic gate", *Digest of Conference on Lasers and Electro-Optics,* Paper TH01, 1987.

16. N.S. Patel, K.A. Rauschenbach, K.L. Hall, "An All-Fiber Optical Demultiplexer and XOR Gate", *SPIE East '95 Paper.*

---

17. K.L. Hall, G. Lenz, A.M. Darwish, and E.P. Ippen, "Subpicosecond gain and index nonlinearities in InGaAsP diode lasers", *Optics Communications,* **111**, p. 589, (1994).

18. K.K. Anderson, M.J. LaGasse, C.A. Wang, and J.G. Fujimoto, "Femtosecond dynamics of the nonlinear index near the band edge in AlGaAs waveguides", *Appl. Phys. Lett.*, **56**, p. 1834, (1990).

19. M.J. LaGasse, D. Liu-Wong, J.G. Fujimoto, and H.A. Haus, "Ultrafast switching with a single-fiber interferometer", *Opt. Lett.*, **14**, p. 311, (1989).

20. G.P Agrawal, "Nonlinear Fiber Optics", 2nd edition, p. 3

21. G.P Agrawal, "Nonlinear Fiber Optics", 2nd edition, p.8.

22. G.P Agrawal, "Nonlinear Fiber Optics", 2nd edition, p.61

23. G.P Agrawal, "Nonlinear Fiber Optics", 2nd edition, p.63

24. G.P Agrawal, "Nonlinear Fiber Optics", 2nd edition, p.64

25. G.P Agrawal, "Nonlinear Fiber Optics", 2nd edition, p.68

26. G.P Agrawal, "Nonlinear Fiber Optics", 2nd edition, p.68

27. G.P Agrawal, "Nonlinear Fiber Optics", 2nd edition, p.15

28. G.P Agrawal, "Nonlinear Fiber Optics", 2nd edition, p.16

29. G.P Agrawal, "Nonlinear Fiber Optics", 2nd edition, p.405

30. G.P Agrawal, “Nonlinear Fiber Optics”, 2nd edition, p.404

31. G.P Agrawal, “Nonlinear Fiber Optics”, 2nd edition, p.15-17

32. G.P Agrawal, “Nonlinear Fiber Optics”, 2nd edition, p.30

33. E.P Ippen MIT Course 6.634 Notes

34. E.P Ippen MIT Course 6.634 Notes

35. E.P Ippen MIT Course 6.634 Notes

36. E.P Ippen MIT Course 6.634 Notes

37. G.P Agrawal, “Nonlinear Fiber Optics”, 2nd edition, p.42

38. G.P Agrawal, “Nonlinear Fiber Optics”, 2nd edition, p.143

39. V.E. Zakharov and A.B. Shabat, *Sov. Phys. JETP*, **34**, p. 62, (1972).

40. V.E. Zakharov and A.B. Shabat, *Sov. Phys. JETP*, **34**, p. 62, (1972).

41. 41. G.P Agrawal, “Nonlinear Fiber Optics”, 2nd edition, p.245

42. K.L. Hall, G. Lenz, A.M. Darwish, and E.P. Ippen, “Subpicosecond gain and index nonlinearities in InGaAsP diode lasers”, *Optics Communications,* **111**, p. 589, (1994).

43. J. Moores, Internal Memorando on NOLM Walk-through switching analysis.

44. J. Moores, Internal Memorando on NOLM Walk-through switching analysis.

45. M. Jino, "All Optical Signal Regularizing / Regemeration Using a Nonlinear Fiber Sagnac Interferometer Switch with Signal-Clock Walk-Off", *J. Lightwave Technol.,* **12**, p. 1648, (1994).

46. P.A. Bélanger and N. Bélanger, "Rms characteristics of pulses in nonlinear dispersive lossy fibers", *Optics Communications,* **117**, p. 56, (1995).

47. K.L. Hall, G. Lenz, A.M. Darwish, and E.P. Ippen, "Subpicosecond gain and index nonlinearities in InGaAsP diode lasers", *Optics Communications,* **111**, p. 589, (1994).

48. K.L. Hall, "Femtosecond Nonlinearities in InGaAsP Diode Lasers", MIT doctoral thesis, 1993.

49. K.L. Hall, "Femtosecond Nonlinearities in InGaAsP Diode Lasers", MIT doctoral thesis, 1993.

50. K.L. Hall, "Femtosecond Nonlinearities in InGaAsP Diode Lasers", MIT doctoral thesis, 1993.

51. K.L. Hall, "Femtosecond Nonlinearities in InGaAsP Diode Lasers", MIT doctoral thesis, 1993.

52. K.L. Hall, "Femtosecond Nonlinearities in InGaAsP Diode Lasers", MIT doctoral thesis, 1993.

---

53. K.L. Hall, “Femtosecond Nonlinearities in InGaAsP Diode Lasers”, MIT doctoral thesis, 1993.

54. K.K. Anderson, M.J. LaGasse, C.A. Wang, and J.G. Fujimoto, “Femtosecond dynamics of the nonlinear index near the band edge in AlGaAs waveguides”, *Appl. Phys. Lett.*, **56**, p. 1834, (1990).

55. E.A. Swanson, S.R. Chin, K.L. Hall, K.A. Rauschenbach, R.S. Bondurant, and J.W. Millner, “100-GHz Soliton Pulse Generation using Soliton Compression of Two Phase Side Bands from a Single DFB Laser”, *IEEE Phton. Technol. Lett.*, **6**, p. 1194, (1994).

56. E.A. Swanson and S.R. Chin, *IEEE Photon. Technol. Lett.*, **7**, p. 114, (1995).

57. H.A. Haus, N.A. Whitaker, Jr., and M.C. Gabriel, “All-optical logic devices using group III-V semiconductor waveguides”, *SPIE Integrated Optical Circuit Engineering II*, **578**, p. 122, (1985).

58. A. Lattes, H.A. Haus, F.J. Leonberger, and E.P. Ippen, “An Ultrafast All-Optical Gate”, *IEEE J. Quantum Electronics*, **19**, p. 1718, (1983).

59. K.I. Kang, T.G. Chang, I. Glesk, P.R. Prucnal, and R.K. Boncek, “Demonstration of ultrafast, all-optical, low control energy, single wavelength, polarization independent, cascadable, and integrable switch”, *Appl. Phys. Lett.*, **67**, p. 605, (1995).

60. N.J. Doran and D. Wood, “Nonlinear-optical loop mirror”, *Optics Letters*, **13**, p. 56, (1988).

61. S. Kawanishi, H. Takara, K. Uchiyama, T. Kitoh, and M. Saruwatari, "100 Gb/s 50 km, and nonrepeated optical transmission employing all-optical multi/demultiplexing and PLL timing extraction", *Elec. Lett.*, **29**, p. 1075, (1993).

62. K.A. Rauschenbach, K.L. Hall, J.C. Livas, and G. Raybon, "All-Optical Pulse Width and Wavelength Conversion at 10 Gb/s Using a Nonlinear Optical Loop Mirror", *IEEE Photon. Techol. Lett.*, **6**, p. 1130, (1994).

63. K.L. Hall, K.A. Rauschenbach, E.A. Swanson, S.R. Chin, and G. Raybon, "Picosecond-Accuracy All-Optical Bit Phase Sensing Using a Nonlinear Optical Loop Mirror", *IEEE Photon. Technol. Lett.*, **7**, p. 935, (1995).

64. B.P. Nelson, N.J. Doran, "Optical Sampling Oscilloscope using Nonlinear Fibre Loop Mirror", *Elec. Lett.*, **27**, p. 204, (1991).

65. K.L. Hall, K.A. Rauschenbach, "All-optical Bit Pattern Generation and Matching at 10 Gb/s", OFC '96 Paper.

66. K. Suzuki, K. Iwatsuki, S. Nishi, M. Saruwatari, "Error-free demultiplexing of 160 Gb/s pulse signal using optical loop mirror including semiconductor laser amplifier", *Elec. Lett.*, **30**, p. 1501, (1994).

67. H. Takara, S. Kawanishi, T. Morioka, K. Mori, M. Saruwatari, "100 Gb/s optical waveform measurement with 0.6 ps resolution optical sampling using subpicosecond supercontinuum pulses", *Elec. Lett.*, 1994.

68. S. Kawanishi, H. Takara, T. Morioka, O. Kamatani, and M. Saruwatari, "200 Gb/s 100 km TDM transmission using Supercontinuum Pulses with Prescaled PLL Timing Extraction and All-Optical Demultiplexing", *OFC '95 post-deadline paper.*

69. S. Kawanishi, H. Takara, T. Morioka, O. Kamatani, K. Takiguchi, T. Kitoh, and M. Saruwatari, "400 Gb/s TDM Transmission of 0.98 ps Pulses over 40 km Employing Dispersion Slope Compensation", *OFC '96 post-deadline paper.*

70. S.L. Danielsen, C. Joergensen, M. Vaa, K.E. Stubkjaer, P. Doussiere, F. Pommerau, L. Goldstein, R. Ngo, M. Goix, "Bit Error Rate Assessment of a 40 Gb/s All-Optical Polarization Independent Wavelength Converter", *OFC '96 post-deadline paper.*

71. D.M. Patrick, A.D. Ellis, D.A.O. Davies, M.C. Tatham, and G. Sherlock, "Demultiplexing using polarisation rotation in a semiconductor laser amplifier", *Elec. Lett.,* **30**, p. 341, (1994).

72. T. Morioka, S. Kawanishi, H. Takara, and O. Kamatani, "Penalty-free, 100 Gb/s optical transmission of < 2 ps supercontinuum transform-limited pulses over 40 km", *Elec. Lett.,* **31**, p. 124, (1995).

73. K. Tamura, E. Yoshida, T. Sugawa, M. Nakazawa, "Broadband light generation by femtosecond pulse amplification with stimulated Raman scattering in a high-power erbium-doped fiber amplifier", *Optics Lett.,* **14**, p. 1631, (1995).

74. H. Takara, S. Kawanishi, M. Sariwatari, "Stabilisation of a modelocked Er-doped fibre laser by suppressing the relaxation oscillation frequency component", *Elec. Lett.,* **31**, p. 292, (1995).

75. H. Takara, S. Kawanishi, T. Morioka, K. Mori, M. Saruwatari, "100 Gb/s optical waveform measurement with 0.6 ps resolution optical sampling using subpicosecond supercontinuum pulses", *Elec. Lett.,* 1994.

76. K.K. Anderson, M.J. LaGasse, C.A. Wang, and J.G. Fujimoto, "Femtosecond dynamics of the nonlinear index near the band edge in AlGaAs waveguides", *Appl. Phys. Lett.*, **56**, p. 1834, (1990).